

UNIVERSITY OF CALIFORNIA  
RIVERSIDE

Exploring Visible-Light-Responsive Photocatalysts for Water Splitting Based on Novel  
Band-gap Engineering Strategies

A Dissertation submitted in partial satisfaction  
of the requirements for the degree of

Doctor of Philosophy

in

Chemistry

by

Jikai Liu

December 2013

Dissertation Committee:

Dr. Pingyun Feng, Chairperson  
Dr. Christopher A. Reed  
Dr. Robert C. Haddon

Copyright by  
Jikai Liu  
2013

The Dissertation of Jikai Liu is approved:

---

---

---

Committee Chairperson

University of California, Riverside

## Acknowledgements

I would like to take this opportunity to express my sincere gratitude and respect to Prof. Pingyun Feng, for her guidance and mentoring. I appreciate her continuous support and kindly encouragement, without which, this dissertation would not have been possible. She demonstrated the dedication and rigorous attitude toward science, which will inspire and benefit me for the rest of my life.

I also thank our excellent collaborators, Prof. Gregory J. O. Beran in Department of Chemistry at UCR and his post-doctor Dr. Shuhao Wen. Prof. Beran and Dr. Wen provided me the deep insights in understanding my experimental results. They helped me to perform theoretical calculations of the two projects in this dissertation. I also want to appreciate Prof. Xianhui Bu at California State University, Long Beach for his valuable suggestion, discussion and encouragement.

Over the past five years, I have also been fortunate to have the opportunities to work together with the excellent members in Prof. Feng's group: Dr. Fan Zuo, Dr. Yang Hou, Dr. Xiaoxin Zou, Dr. Rui Liu, Dr. Zhenyu Zhang, Dr. Tao Wu, Dr. Qipu Lin, Dr. Xiang Zhao, Dr. Le Wang, Chengyu Mao, Xitong Chen, Yuan Wang, and Fei Bu, who help me in many ways.

I am also very grateful to the rest of my dissertation committee, Prof. Christopher A. Reed and Prof. Robert C. Haddon, for their valuable comments on my dissertation.

There are many others who deserve my sincere thanks. I would like to thank the staff in Department of Chemistry for their kind service and favor.

Finally, I want to sincerely thank my parents and my friends for everything they have done for me. Without their love, encouragement and support, I could not finish my Ph. D. study smoothly.

## ABSTRACT OF THE DISSERTATION

Exploring Visible-Light-Responsive Photocatalysts for Water Splitting Based on Novel  
Band-gap Engineering Strategies

by

Jikai Liu

Doctor of Philosophy, Graduate Program in Chemistry  
University of California, Riverside, December 2013  
Dr. Pingyun Feng, Chairperson

The increasing demand for renewable energy is driving innovations in both science and technology. Hydrogen has been broadly identified as a potential clean energy carrier due to its high energy capacity (enthalpy of combustion is as high as 286 kJ/mol) and environmental friendliness (the only product after burning is water). Meanwhile, solar energy is renewable, abundant and easily available. Solar-driven H<sub>2</sub> production from water has therefore attracted global attention in the past decades since the first report of photoelectrochemical (PEC) water splitting based on an n-type TiO<sub>2</sub> photoanode. Many semiconductor-based materials have been synthesized and studied for their photocatalytic or PEC performance.

Among them, visible-light-active photocatalysts are more promising since the energy of the visible-light region takes up a large proportion of the whole solar spectrum.

Herein, we found two novel groups of compounds, e.g. copper borates and boron carbides. We investigated the origins and performances of their photocatalytic water splitting under visible light irradiation. It is found that the visible light activities of the two groups are resulted from different band-gap engineering mechanisms.

For the two copper borates compounds, e.g. CuB<sub>2</sub>O<sub>4</sub> and Cu<sub>3</sub>B<sub>2</sub>O<sub>6</sub>, we found that the visible light activity is from the intrinsic midgap states in the two compounds. Both midgap states serve as an electron acceptor level, but they function very differently in the two copper borates. For CuB<sub>2</sub>O<sub>4</sub>, the midgap states facilitate the visible light absorption for photocatalytic water splitting, while for Cu<sub>3</sub>B<sub>2</sub>O<sub>6</sub>, the midgap states trap electrons and reduce the photocatalytic activity.

For the two boron carbides, e.g. B<sub>4.3</sub>C and B<sub>13</sub>C<sub>2</sub>, they exhibit efficient photocatalytic H<sub>2</sub> evolution and PEC H<sub>2</sub> evolution as a stable photocathode under visible light irradiation. Interestingly, it is found that the inherent defects and structural distortions in B<sub>4.3</sub>C cause a continuum downshift of its conduction band (CB) edge that facilitates visible-light absorption and water splitting based on density functional theory (DFT) calculations. In B<sub>13</sub>C<sub>2</sub>, however, the more complicated structural defects and distortions result in a large number of midgap states between the CB and the valence band (VB), which reduce its overall photocatalytic and PEC water splitting efficiency by promoting charge recombination.

## Table of Contents

Acknowledgements.....	iv
Abstract.....	vi
Table of Contents.....	viii
List of Figures.....	xii

### **Chapter 1 An Overview of Semiconductor-based Photocatalytic Water Splitting**

1.1 Origin of Semiconductor-based Photocatalytic Water Splitting.....	1
1.2 Working Mechanism in Photocatalytic Water Splitting.....	5
1.3 Half-reactions of Photocatalytic Water Splitting:	
Sacrificial H <sub>2</sub> or O <sub>2</sub> Evolution.....	7
1.4 General Techniques for Characterization.....	8
1.5 Evaluation of Photocatalytic Water Splitting.....	9
1.5.1 Time Course of H <sub>2</sub> and O <sub>2</sub> Evolution.....	10
1.5.2 Turnover Number (TON).....	10
1.5.3 Quantum Yield.....	11
1.6 Experimental Setups.....	12
1.7 References.....	16

**Chapter 2 An Introduction to Semiconductor-based Photocatalysts and Approaches of Band-gap Engineering**

2.1 Wide Band Gap Photocatalysts with UV Light Activity.....	18
2.1.1 Metal Oxides with d <sup>0</sup> Electronic Configuration.....	18
2.1.2 Metal Oxides with d <sup>10</sup> Electronic Configuration.....	22
2.1.3 Metal Nitrides with d <sup>10</sup> Electronic Configuration.....	22
2.2 Visible-light Driven Photocatalysts and Approaches of Band-gap Engineering.....	23
2.2.1 Native Visible-light Driven Photocatalysts.....	24
2.2.2 Approaches of Band-gap Engineering.....	25
2.2.2.1 Metal or/and Non-metal Doping.....	26
2.2.2.2 Developing Solid Solutions.....	30
2.2.2.3 Developing Single-phase Visible-light Active Photocatalysts.....	34
2.2.2.4 Other Newly Explored Approaches.....	41
2.3 References.....	48

**Chapter 3** Visible-light-responsive Copper (II) Borate Photocatalysts with Intrinsic  
Midgap States for Water Splitting

3.1 Introduction.....	60
3.2 Experimental Section.....	61
3.2.1 Method of Synthesis.....	61
3.2.2 Characterizations.....	62
3.2.3 Photocatalytic Experiments.....	63
3.3 Density of States (DOS) Calculations.....	66
3.4 Results and Discussion.....	67
3.4.1 Instrumental Characterizations.....	67
3.4.2 Study of Photocatalytic Water Splitting.....	73
3.4.3 Study of DOS Calculations.....	78
3.5 Conclusion.....	82
3.6 References.....	83

**Chapter 4 Boron Carbides as Efficient, Metal-free, Visible-light-responsive Photocatalysts**

4.1 Introduction.....	85
4.2 Experimental Section.....	87
4.2.1 Method of Synthesis.....	87
4.2.2 Characterizations.....	87
4.2.3 Photocatalytic Experiments.....	88
4.2.4 Photoelectrochemical (PEC) Experiments.....	90
4.3 Density of States (DOS) Calculations.....	91
4.4 Results and Discussion.....	93
4.4.1 Instrumental Characterizations.....	93
4.4.2 Study of Photocatalytic and PEC H <sub>2</sub> Evolution.....	100
4.4.3 Study of DOS Calculations.....	107
4.5 Conclusion.....	111
4.6 References.....	112

## List of figures

- Figure 1.1** Honda-Fujishima effect-water splitting using a TiO<sub>2</sub> photoelectrode. **Page 3**
- Figure 1.2** Processes involved in photocatalytic overall water splitting on a heterogeneous photocatalyst. **Page 5**
- Figure 1.3** The scheme of a photoelectrochemical cell for water splitting. **Page 13**
- Figure 1.4** An example of the experimental setup for photocatalytic water splitting. **Page 14**
- Figure 2.1** Donor level (A) and acceptor level (B) formed by metal ion doping. **Page 26**
- Figure 2.2** New valence band formation by doping of non-metal ions. **Page 29**
- Figure 2.3** Band structure controlled by making a solid solution. **Page 30**
- Figure 2.4** (A) Schematic band structures. Reprinted with permission from Ref. 90. Copyright 2005 American Chemical Society. (B) UV-visible diffuse reflectance spectra of (Ga<sub>1-x</sub>Zn<sub>x</sub>)(N<sub>1-x</sub>O<sub>x</sub>). **Page 31**
- Figure 2.5** Band structure of BiVO<sub>4</sub> calculated by DFT. **Page 35**
- Figure 2.6** Left: Energy scheme for IrO<sub>2</sub>, showing optical transitions and electron transfer processes.; Right: Schematic band structure of Rh<sup>3+</sup>-doped ZnGa<sub>2</sub>O<sub>4</sub>. **Page 43**
- Figure 2.7** Left: Spectral absorbance of the white and black TiO<sub>2</sub> nanocrystals. The inset enlarges the absorption spectrum in the range from approximately 750 to 1200 nm. Right: Schematic illustration of the DOS of disorder-engineered black TiO<sub>2</sub> nanocrystals, as compared to that of unmodified TiO<sub>2</sub> nanocrystals. **Page 44**
- Figure 2.8** Left: Sample prepared so that both ‘new’ and ‘original’ phases are present simultaneously at the surface (the original surface in blue and the new TiO<sub>2</sub> phase in red). Right: Band diagram after growing the new phase of TiO<sub>2</sub>. **Page 45**

- Figure 3.1** Unit cell portions of the crystal structures of CuB<sub>2</sub>O<sub>4</sub> (A) and Cu<sub>3</sub>B<sub>2</sub>O<sub>6</sub> (B). The color code is as follows: oxygen (red); boron (dark yellow); copper in square (cyan), pyramidal (yellow) and octahedral (green) geometry. **Page 68**
- Figure 3.2** XRD patterns of CuB<sub>2</sub>O<sub>4</sub> (top) and Cu<sub>3</sub>B<sub>2</sub>O<sub>6</sub> (bottom). **Page 69**
- Figure 3.3** SEM pictures of prepared (a) CuB<sub>2</sub>O<sub>4</sub> and (b) Cu<sub>3</sub>B<sub>2</sub>O<sub>6</sub>. **Page 70**
- Figure 3.4** General survey XPS spectra of copper borates before and after H<sub>2</sub> evolution. **Page 71**
- Figure 3.5** The ESR spectra of (a) CuB<sub>2</sub>O<sub>4</sub> and (b) Cu<sub>3</sub>B<sub>2</sub>O<sub>6</sub> at room temperature. **Page 72**
- Figure 3.6** Diffuse reflectance spectra for CuB<sub>2</sub>O<sub>4</sub> (■) and Cu<sub>3</sub>B<sub>2</sub>O<sub>6</sub> (△). **Page 73**
- Figure 3.7** (a) O<sub>2</sub> evolution data as a function of time under visible light (>400 nm). (b) Time course of H<sub>2</sub> evolution under visible light irradiation (>400 nm). Symbol: CuB<sub>2</sub>O<sub>4</sub> (■) and Cu<sub>3</sub>B<sub>2</sub>O<sub>6</sub> (△). **Page 74**
- Figure 3.8** XPS spectra of copper borates before and after O<sub>2</sub> evolution reaction (bottom: highly resolved XPS spectra of Ag 3d after O<sub>2</sub> evolution reaction). **Page 75**
- Figure 3.9** XPS spectra of copper borates before and after H<sub>2</sub> evolution reaction. **Page 76**
- Figure 3.10** The comparison of total and projected density of states (PDOS) using LSDA+U for (a) CuB<sub>2</sub>O<sub>4</sub> and (b) Cu<sub>3</sub>B<sub>2</sub>O<sub>6</sub>. **Page 79**
- Figure 3.11** LSDA+U PDOS in antiferromagnetically ordered ground state. U(Cu)=7.5 eV, J(Cu)=0.98 eV are used for both CuB<sub>2</sub>O<sub>4</sub> and Cu<sub>3</sub>B<sub>2</sub>O<sub>6</sub>. **Page 80**
- Figure 3.12** Schematic of the band structures and midgap states of the two copper borates and possible electronic excitations under visible light irradiation. **Page 81**

**Figure 4.1** Supercell model of  $B_{4.3}C$ . Red ellipses show C-B-B chains; Yellow ellipses show the C-B-C chains. Green circles show  $B_{11}C^{polar-site}$  icosahedra. **Page 92**

**Figure 4.2** Supercell model of  $B_{13}C_2$ . Red ellipses show C-B-B chains; Yellow ellipses show the C-B-C chains; Purple ellipses show the B-vacancy-B chains; Green circles show  $B_{11}C^{polar-site}$  icosahedra; Brown circles show the  $B_{12}$  icosahedra. **Page 93**

**Figure 4.3** Idealized elementary cell of boron carbides. B gray, C black. **Page 94**

**Figure 4.4** XRD patterns: (a)  $B_{4.3}C$  and  $B_{13}C_2$ . **Page 95**

**Figure 4.5** FT-Raman spectra.  $B_{13}C_2$  (gray),  $B_{4.3}C$  (black). **Page 96**

**Figure 4.6** Top: UV-visible diffuse reflectance spectra. Bottom: Photoluminescence spectra at room temperature with the excitation wavelength of 325 nm. **Page 97**

**Figure 4.7** SEM images of  $B_{4.3}C$  (top) and  $B_{13}C_2$  (bottom). **Page 98**

**Figure 4.8** EDX spectra of  $B_{4.3}C$  (top) and  $B_{13}C_2$  (bottom). **Page 99**

**Figure 4.9** The TGA curves of  $B_{4.3}C$  and  $B_{13}C_2$  in air. **Page 100**

**Figure 4.10** Time course of  $H_2$  evolution under visible light irradiation. a) 1st cycle, b) 2nd cycle after reevacuation, c) 3rd cycle after re-evacuation, d) 4th cycle after re-evacuation and 100 h reaction time.  $B_{4.3}C$  with Pt (—■—),  $B_{4.3}C$  without Pt (—□—),  $B_{13}C_2$  with Pt (—▼—),  $B_{13}C_2$  without Pt (—▽—). **Page 101**

**Figure 4.11** Synthesized g-C<sub>3</sub>N<sub>4</sub> for  $H_2$  evolution reaction under the same experimental conditions as what were used for boron carbides. (Since the activity of g-C<sub>3</sub>N<sub>4</sub> without Pt is too low, sampling interval was extended to 1 hour instead of 30 min in order to reduce experimental errors.). **Page 102**

**Figure 4.12** XRD patterns of  $B_{4.3}C$  before and after photocatalysis reaction (top) and  $B_{13}C_2$  before and after photocatalysis reaction (bottom). **Page 104**

**Figure 4.13** FT-Raman spectra of  $B_{4.3}C$  before and after photocatalysis reaction (top) and  $B_{13}C_2$  before and after photocatalysis reaction (bottom). **Page 105**

**Figure 4.14** a) Current-potential curves in  $Na_2SO_4$  aqueous solution (0.01m) under visible light. [1]  $B_{4.3}C$  dark, [2]  $B_{4.3}C$  visible light, [3]  $B_{13}C_2$  dark, [4]  $B_{13}C_2$  visible light. b) Transient photocurrent curves under visible light at -0.8 V vs. SCE.  $B_{13}C_2$  (gray),  $B_{4.3}C$  (black). **Page 106**

**Figure 4.15** a) and b) Total DOS of the optimized ideal structure of  $(B_{11}C)CBC$ . c) and d) The DOS of  $B_{4.3}C$  and  $B_{13}C_2$  with defects, but no structural relaxation. e) and f) The DOS of  $B_{4.3}C$  and  $B_{13}C_2$  with defects after structural relaxation. The dotted gray line highlights the downshift of the conduction band edge for  $B_{4.3}C$ . **Page 108**

**Figure 4.16** The site projected density of states (PDOS) of  $B_{4.3}C$ . **Page 110**

**Figure 4.17** The site PDOS of  $B_{13}C_2$ . **Page 110**

# **Chapter 1**

## **An Overview of Semiconductor-based Photocatalytic Water Splitting**

### **1.1 Origin of Semiconductor-based Photocatalytic Water Splitting**

The increasing demand for renewable energy is driving innovations in both science and technology. Hydrogen has been broadly identified as one of the potential clean energy carriers due to its high energy capacity (enthalpy of combustion is as high as 286 kJ/mol) and environmental friendliness (the only product after burning is water). Moreover, hydrogen is also widely used in many chemical industries, such as industrial ammonia synthesis and fuel cell industry.<sup>1</sup> At present, hydrogen is mainly produced by reforming reactions of natural hydrocarbon resources such as fossil fuels or biomass.<sup>2</sup> The commercial hydrogen gas is produced by the steam reforming of natural gas (methane) in industry.



The present technique is defective and even unacceptable if one thinks of energy and environmental issues. First, the process is an intensive endothermic reaction and requires a temperature as high as 700-1000 °C. Secondly, the non-renewable fossil fuels are consumed and the green house gas CO<sub>2</sub> is emitted as a byproduct in the process. These flaws during industrial production confine the broad application of H<sub>2</sub> as a

low-cost and clean energy carrier. Therefore, exploring renewable and environmental-friendly strategies to produce H<sub>2</sub> has been urged.

To save depletable fossil fuels and eliminate unwanted emissions of CO<sub>2</sub>, water is an ideal hydrogen source. But it does require external energy input to split water into H<sub>2</sub> and O<sub>2</sub> (H<sub>2</sub>O(g)----1/2O<sub>2</sub>(g)+H<sub>2</sub>(g) ΔH<sup>0</sup>=241.8 kJ mol<sup>-1</sup>), such as electrical power. The process is widely known as electrolysis of water. If the energy input can be obtained from a renewable source, such as solar energy, H<sub>2</sub> can then become a low-cost and clean energy alternative capable of powering our planet.<sup>3</sup> There are several ways for solar hydrogen production from water. One is electrolysis of water using a solar cell. On top of that, photocatalytic and photoelectrochemical (PEC) water splitting provide two promising strategies to achieve the purpose, too.<sup>4-7</sup>

Photocatalytic water splitting was firstly discovered by Fujishima and Honda through single-crystalline n-type TiO<sub>2</sub> electrodes under ultraviolet (UV) irradiation in 1972.<sup>8</sup>

As shown in Figure 1.1, electrons and holes are generated in TiO<sub>2</sub> under UV irradiation. The photo-induced electrons can reduce water to form H<sub>2</sub> on a Pt counter electrode while holes can oxidize water to form O<sub>2</sub> on the TiO<sub>2</sub> electrode with some external bias. In the process, the semiconductor of TiO<sub>2</sub> harvests UV light and generates electrons for water reduction, which is the key media to convert the energy of light into a

kind of chemical energy ( $H_2$ ) by splitting water molecules. Therefore, semiconductors with this function are usually called photocatalysts in the research field. The pioneering discovery of Fujishima and Honda has triggered numerous studies on semiconductor-based photocatalytic water splitting in the past two decades.

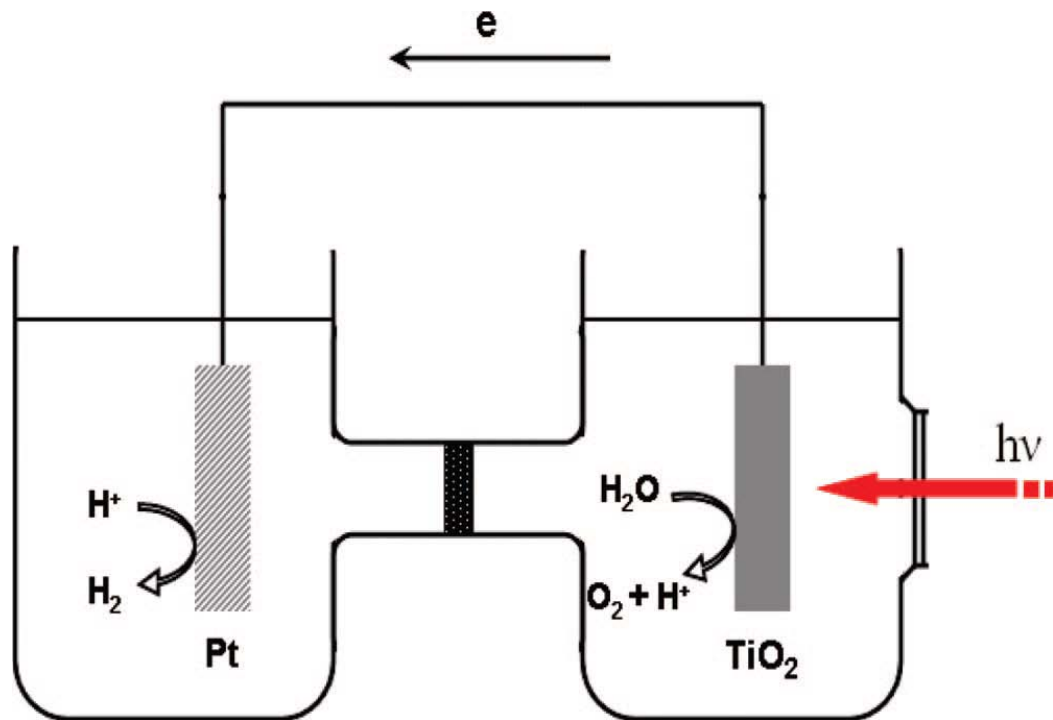


**Figure 1.1** Honda-Fujishima effect-water splitting using a  $TiO_2$  photoelectrode. Reprinted with permission from Ref. 7 and Ref. 8. Copyright American Chemical Society 2010 and Nature Publishing Group 1972.

Not all semiconductors are able to perform photocatalytic water splitting. As we all know, semiconductors have a band gap in which the conduction band (CB) is separated from the valance band (VB) by a band gap. When the energy of incident light is larger than that of the band gap of the semiconductor, electrons and holes are generated in the CB and VB, respectively. Then water molecules are reduced by the electrons to form  $H_2$

and oxidized by the holes to form O<sub>2</sub> for overall water splitting. In principle, there are three important points for the reactions to proceed. From the thermodynamic point of view, the redox potentials of photogenerated electrons and holes have to be suitable for the redox reactions of water molecules. That means the bottom level of the conduction band has to be more negative than the redox potential of H<sup>+</sup>/H<sub>2</sub> (0 V vs. NHE), while the top level of the valence band has to be more positive than the redox potential of O<sub>2</sub>/H<sub>2</sub>O (1.23 V). Therefore, semiconductors must have a band gap larger than 1.23 eV with suitable levels of CB and VB for water splitting. Semiconductors with wide band gaps seem appropriate candidates to satisfy these basic requirements. However, from an efficiency point of view, the energy distribution within the solar spectrum of 1.5 air mass condition (1.5 atmosphere thickness with a solar zenith angle of  $z=48.2^\circ$  corresponds to the solar spectrum at mid-latitudes where are the world's major population centers) is approximately 2% ultraviolet, 47% visible (corresponding wavelength of 380-780 nm) and 51% infra-red.<sup>9</sup> Therefore, wide band gap semiconductors with only UV response have deficient practical applications although many of them have been explored for photocatalytic water splitting, such as TiO<sub>2</sub>,<sup>10</sup> ZrO<sub>2</sub>,<sup>11</sup> K<sub>4</sub>Nb<sub>6</sub>O<sub>17</sub><sup>12</sup> et al. The main efforts currently focus on exploring photocatalysts with visible light response. In addition to the basic requirements and efficiency concern, practically, semiconductors have to be stable in aqueous solution under irradiation of light. Some chalcogenide semiconductors are

considered as suitable photocatalysts to split water under visible light irradiation. Although some of them, such as CdS,<sup>13</sup> do decompose water with very high efficiency under visible light irradiation (the quantum yield of CdS can reach 93% at 420 nm),<sup>14</sup> the photogenerated holes would oxidize and decompose CdS instead of water during the reaction.<sup>5</sup> This is a fatal disadvantage for most chalcogenide photocatalysts. Therefore, exploring suitable and stable semiconductors for efficient photocatalytic water splitting under sunlight irradiation are still a challenge.

## 1.2 Working Mechanism in Photocatalytic Water Splitting

Figure 1.2 presents three main steps in a typical photocatalytic reaction. They all greatly influence the photocatalytic performance of a photocatalyst.

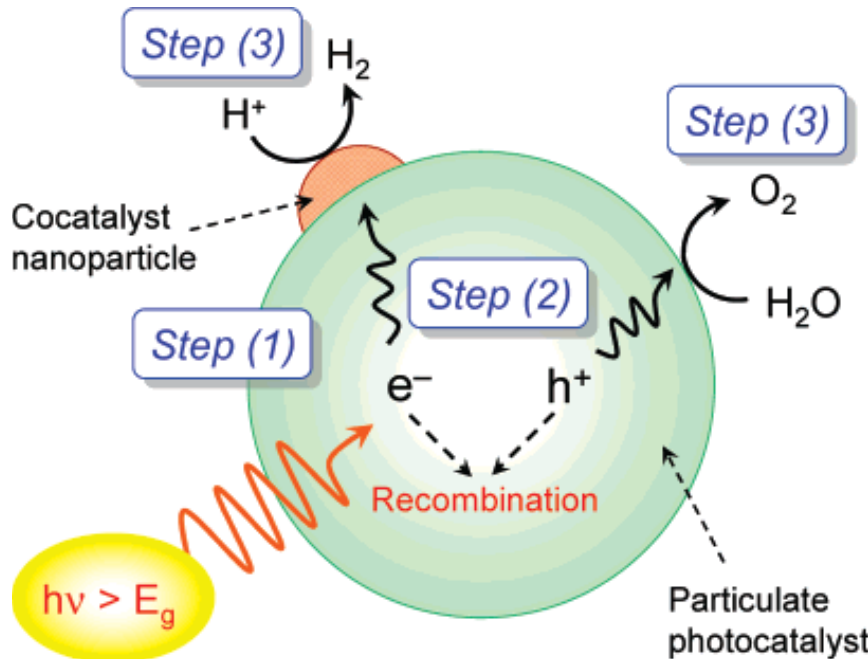


**Figure 1.2** Processes involved in photocatalytic overall water splitting on a heterogeneous photocatalyst. Reprinted with permission from Ref. 15. Copyright American Chemical Society 2007.

(i) Photocatalysts absorb photons to generate electron-hole pairs. As illustrated in Figure, the semiconductor can absorb photons in the incident light and generate electron-hole pairs (so-called excitons) if the energy of incident photons is larger than that of the band gap of the semiconductor. As an electron is excited to the conduction band by the incident photons, a hole will be left behind in the valence band. The photogenerated electron-hole pairs function similarly to the electrolysis of water. The electrons will reduce water molecules to form H<sub>2</sub> and the holes will oxidize them to form O<sub>2</sub> for overall water splitting.

(ii) The charge separation and migration of the photogenerated carriers. Basically, the photogenerated electron-hole pairs have to separate and migrate to the surface reaction sites of photocatalysts and then proceed the photocatalytic reactions. Crystal structure, crystallinity and particle size of the photocatalysts greatly affect this step. For the same photocatalyst (the same crystal structure), higher crystallinity possesses better charge separation and migration because better crystallinity means less structural defects in the crystal. Defects are usually considered as the trapping and recombination centers between photogenerated electrons and holes, resulting in a decrease in the photocatalytic activity. To achieve higher photocatalytic activity, smaller particle size of photocatalysts is preferred because it would provide higher surface area with more reactive sites and shorten the distance for the photogenerated excitons to migrate to the surface reaction

sites and thus decrease the probability of recombinations.

(iii) The surface chemical reactions. The surface active sites and the surface area influence the third step. Even though the as-formed electrons and holes possess thermodynamically sufficient potentials for water splitting, the greatest part of them will recombine with each other before they can participate in the photocatalytic reaction. A common solution is to load co-catalysts on the surface of photocatalysts, such as Pt,<sup>16</sup> Pd,<sup>17</sup> Ru,<sup>18</sup> NiO,<sup>19</sup> RuO<sub>2</sub>,<sup>20</sup> and Cr/Rh oxides.<sup>21</sup> These co-catalysts usually function as active sites in which photocatalytic reactions occur. Besides creating surface active sites, increasing surface area of photocatalysts is always an efficient strategy to obtain higher photocatalytic activity.

The three steps are all crucial for photocatalytic water splitting. Therefore, an efficient photocatalyst must have suitable electronic band structure, bulk properties, and surface characters. The research field of photocatalytic water splitting is still in the stage of laboratory research by far. That means efficient photocatalysts with visible light response have not been developed. Many efforts have been made to explore new photocatalysts and function or modify existent photocatalysts.

### **1.3 Half-reactions of Photocatalytic Water Splitting: Sacrificial H<sub>2</sub> or O<sub>2</sub> Evolution**

As mentioned above, there are strict requirements for semiconductors to perform overall photocatalytic water splitting, i.e. conduction band minimum more negative than

$\text{H}^+/\text{H}_2$  redox potential and valence band maximum more positive than  $\text{O}_2/\text{H}_2\text{O}$  redox potential. An overall photocatalytic water splitting is defined as  $\text{H}_2$  and  $\text{O}_2$  being produced simultaneously in a stoichiometric ratio (2:1) from pure water. The overall water splitting is more promising and the ultimate goal. In practice, however, this kind of semiconductors, especially those with visible light response, is rare. Even though some have suitable band positions, stability can make an issue for practical application. The semiconductors whose band structures can meet only one of the above requirements can proceed with half-reactions of photocatalytic water splitting but a sacrificial agent is needed. So the reaction is named as sacrificial  $\text{H}_2$  or  $\text{O}_2$  evolution. Note that most of photocatalysts explored so far can only conduct sacrificial  $\text{H}_2$  or  $\text{O}_2$  evolution. For sacrificial  $\text{H}_2$  evolution, photogenerated electrons reduce water molecules to produce  $\text{H}_2$  and a reducing agent or hole scavengers have to be added in the aqueous solution to consume the corresponding holes. The common hole scavengers are alcohol, sulfide and sulfite ions. Similarly, for sacrificial  $\text{O}_2$  evolution, oxidizing reagents or electron scavengers, such as  $\text{Ag}^+$ ,<sup>22</sup>  $\text{Fe}^{3+}$ ,<sup>23</sup>  $\text{Ce}^{4+}$ ,<sup>24</sup> are commonly used in aqueous solutions to consume the redundant electrons when water molecules are oxidized by the photogenerated holes to evolve  $\text{O}_2$ . It should be noted that even if a photocatalyst thermodynamically is able to drive both half reactions, respectively, with either reducing or oxidizing sacrificial agents, it does not mean that it must be able to perform overall

water splitting water from pure water because of the kinetic issue.

#### **1.4 General Techniques for Characterization**

As introduced above, proper band structures of the semiconductors, such as band gap, redox potentials of CB and VB, are the basic requirements and extremely crucial for photocatalysis. Detailed characterizations of the band structures are usually necessary. The band gap can be obtained by UV-Visible light absorption measurement. For newly explored photocatalysts, determining the redox potentials of CB and VB is also desirable. Ultra High Vacuum X-ray Photoelectron Spectroscopy (UHV-XPS) is generally used to determine the redox potential of the VB while some electrochemical method (Mott-schottky method) can be employed to determine the redox potential of the CB. Other properties of the photocatalysts, such as crystallinity, particle size, surface area, etc. all influence the photocatalytic performance greatly. Therefore, these properties have to be fully characterized. The crystallinity can be evaluated by X-ray diffraction (XRD) and high resolution transmission electron microscopes (HRTEM). Scanning electron microscopes (SEM) and TEM can show the particle size and morphology of the photocatalysts. The surface area of the photocatalysts is usually determined by the Brunauer–Emmett–Teller (BET) measurement. Besides the above general techniques, other characterization methods may be applied for some specific photocatalysts and research reasons.

## **1.5 Evaluation of Photocatalytic Water Splitting**

Hundreds of photocatalysts have been discovered and thousands of strategies have been reported in literature to function and modify the existing photocatalysts in order to improve the photocatalytic performance. Therefore, no matter for theoretical study or future practical application, a unified standard has to be established to evaluate the performance of these photocatalysts.

### **1.5.1 Time Course of H<sub>2</sub> and O<sub>2</sub> Evolution**

For a typical photocatalytic reaction, amounts of H<sub>2</sub> and O<sub>2</sub> gas should increase with irradiation time. The photocatalytic activity is assessed by the amounts of evolved gas products over irradiation time. Repeated experiments are informative to indicate the long-term stability of the photocatalysts. A stable photocatalyst should exhibit no or negligible activity decrease after a long term photocatalytic reaction.

### **1.5.2 Turnover Number (TON)**

TON is an important reference to indicate the catalytic character for many catalysts. In photocatalysis, TON also has to be studied. Amounts of photogenerated H<sub>2</sub> and O<sub>2</sub> should overwhelm the amount of used photocatalysts. If not, it is hard to determine that this process is a photocatalytic or a chemical reaction. It is possible that H<sub>2</sub> and O<sub>2</sub> can be produced from the chemical reactions between the semiconductors and water, or the self-decomposition of the semiconductors, which are not a real catalytic process.

Turnover number is usually defined by the number of reacted molecules to that of an active site.

$$TON = \frac{\text{number of reacted molecule}}{\text{number of active sites}}$$

For the heterogeneous photocatalysis, however, it is impossible to accurately determine the number of active sites on the surface of a photocatalyst. Therefore, an alternative method is commonly adopted. Instead of the number of active sites, the number of molecules in the photocatalyst is used in above equation. A modified equation is then proposed as follows:<sup>5</sup>

$$TON = \frac{\text{number of reacted electrons}}{\text{number of molecules in a photocatalyt}}$$

The number of reacted electrons is calculated from the number of moles of evolved H<sub>2</sub> or O<sub>2</sub> gas. The TON calculated with the above equation is actually smaller than the real value because the number of molecules in the whole photocatalyst is definitely more than that of active sites on the surface of the photocatalyst.

### 1.5.3 Quantum Yield

As photocatalytic water splitting has attracted global attention, various photocatalysts have been studied with various experimental setups and conditions in different labs. Different experimental setups or conditions, such as the light source, will give different activities ( e.g. evolution rates of H<sub>2</sub> or O<sub>2</sub> derived from the time course measurements ) even using the same photocatalysts. To compare the efficiencies of these

photocatalysts, it is meaningless to just compare their activities.

A fair and widely accepted standard to evaluate the efficiency of various photocatalysts from different research groups globally is the quantum yield (QY). The quantum yield is defined by the equation below:

$$\text{Quantum yield} = \frac{\text{number of reacted electrons}}{\text{number of absorbed photons}}$$

Quantum yield excludes the influence of different light sources. Practically, however, it is difficult to measure the number of absorbed photons. Therefore, an extended term 'external quantum yield' (or apparent quantum yield, assigned as EQY or AQY) is usually used to assess the performance of photocatalysts.<sup>5</sup>

$$\text{AQY \%} = \frac{\text{number of reacted electrons}}{\text{number of incident photons}} \times 100$$

The number of incident photons can be measured by photometer, such as Si photodiode. It should be noted that the AQY is estimated to be lower than the real QY because the number of absorbed photons is usually smaller than that of incident photons by the light scattering of the solid semiconductors.

## 1.6 Experimental Setups

The discovery which launched the research area was firstly fulfilled with a photoelectrochemical (PEC) cell using rutile as a photoanode. The experimental setup is still broadly used to study the photoelectrochemical water splitting. As shown in the Figure 1.3, the PEC cell consists of a photocathode/photoanode as working electrode and

a metal as counter electrode. If a photocathode is applied as working electrode, the water molecules are reduced on the photocathode to generate H<sub>2</sub> and oxidized on the counter electrode to produce O<sub>2</sub>. Similarly, if a photoanode is used as working electrode, O<sub>2</sub> will evolve from it by oxidizing water and H<sub>2</sub> will be generated on the counter electrode by reducing water molecules. A third electrode is usually used as a reference electrode to monitor the external applied bias. The PEC performance of the photocatalysts can be studied by measuring a series of photoelectrical properties, such as photocurrent to potential property (I-V curve) and photocurrent to time property (I-T curve).

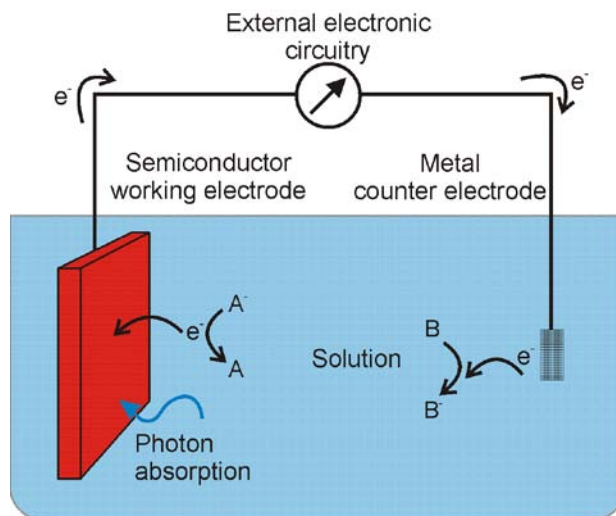


**Figure 1.3** The scheme of a photoelectrochemical cell for water splitting. Copyright Photoelectrochemistry of Semiconductors, Electrochemistry Encyclopedia, November, 2011.

Another popular apparatus for photocatalytic water splitting is shown in Figure 1.4. A gas-closed circulation system is equipped with a vacuum line, a reaction cell, a gas-circulation pump and a gas sampling port that is directly connected to a gas

chromatograph. The whole system should be completely air-free since  $O_2$  in the air will influence the photocatalytic reaction and results. A vacuum line is applied for degassing the system and a high-quality gas-closed system is necessary to keep the system air-free. The optical window of the reactor should be made of quartz which allows both the UV and visible light to go through. The gas-circulation pump is designed here to evenly distribute the gas products in the system which can improve the reliability of the measurement. After the gas products are generated and evenly distributed in the system, a carrier gas line (argon is commonly used) is connected to the sampling port, pushing the gas products into the gas chromatography (GC) to analyze. A thermal conductivity detector (TCD) is installed in the GC to test the  $H_2$  and  $O_2$  gases.

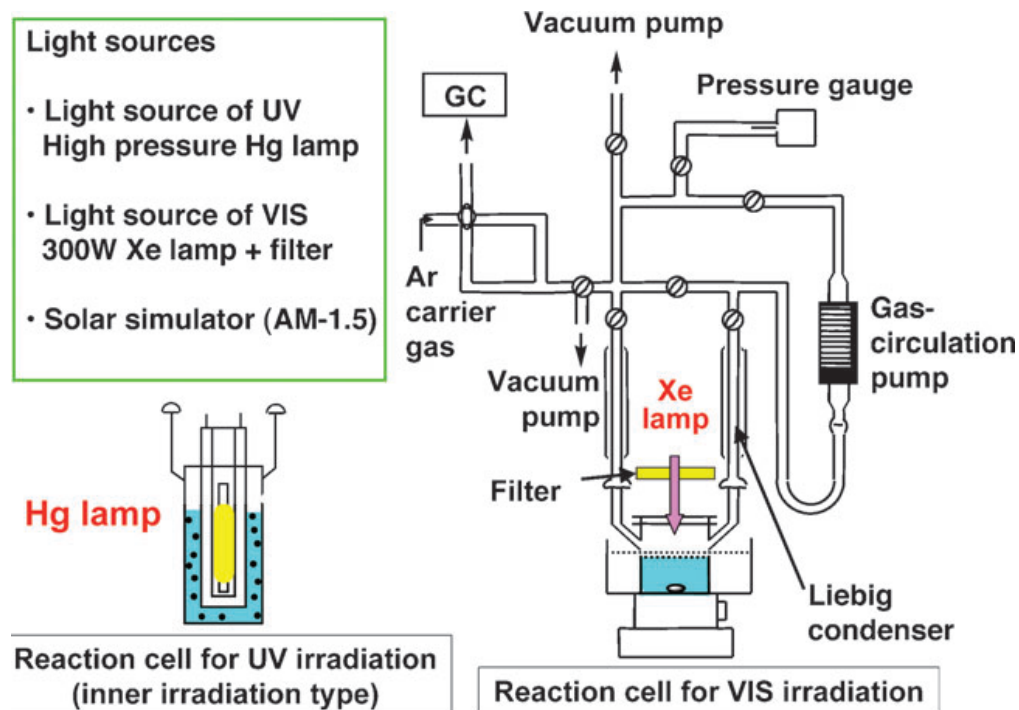


**Figure 1.4** An example of the experimental setup for photocatalytic water splitting. Reprinted with permission from Ref. 5. Copyright Royal Society of Chemistry, 2009.

As shown on the left of Figure 1.4, an inner irradiation reaction cell is recommended to improve the irradiation efficiency. Different light sources are used based on different applications. For a UV application, high-pressure mercury lamps are usually used. If studying the performance under visible light irradiation, Xe lamps are often employed. Proper optical filters may be applied between the optical window of the reactor and the light source if a specific range of light wavelength needs to be studied. A solar simulator with an air-mass 1.5 filter (AM 1.5), which can provide a power of 100 mW cm<sup>-2</sup>, is a standard light source to evaluate the efficiency of solar hydrogen production of a photocatalyst.

## 1.7 References

- (1) Max Appl "Ammonia" in Ullmann's Encyclopedia of Industrial Chemistry, **2006** Wiley-VCH, Weinheim.
- (2) Cortright, R. D.; Davda, R. R.; Dumesic, J. A. *Nature* **2002**, *418*, 964-967.
- (3) Lewis, N. S.; Nocera, D. G. *Proc. Natl. Acad. Sci. U. S. A.* **2006**, *103*, 15729-15735.
- (4) Osterloh, F. E. *Chem. Mater.* **2008**, *20*, 35-54.
- (5) Kudo, A.; Miseki, Y. *Chem. Soc. Rev.* **2009**, *38*, 253-278.
- (6) Walter, M. G.; Warren, E. L.; McKone, J. R.; Boetcher, S. W.; Mi, Q.; Santori, E. A.; Lewis, N. S. *Chem. Rev.* **2010**, *110*, 6446-6473.
- (7) Chen, X.; Shen, S.; Guo, L.; Mao, S. S. *Chem. Rev.* **2010**, *110*, 6503-6570.
- (8) Fujishima, A.; Honda, K. *Nature* **1972**, *238*, 37-38.
- (9) Solar Spectrum, Australian Glass & Glazing Association Technical Fact Sheet.
- (10) Fujishima, A.; Zhang, X.; Tryk, D. A. *Int. J. Hydrogen Energy* **2007**, *32*, 2664-2672.
- (11) Sayama, K.; Arakawa, H. *J. Phys. Chem.* **1993**, *97*, 531-533.
- (12) a) Domen, K.; Kudo, A.; Shibata, M.; Tanaka, A.; Maruya, K.; Onishi, T. *J. Chem. Soc., Chem. Commun.* **1986**, *23*, 1706-1707. b) Domen, K.; Kudo, A.; Shinozaki, A.; Tanaka, A.; Maruya, K.; Onishi, T. *J. Chem. Soc., Chem. Commun.* **1986**, *4*, 356-357.
- (13) a) Matsumura, M.; Saho, Y.; Tsubomura, H. *J. Phys. Chem.* **1983**, *87*, 3807-3808. b) Reber, J. F.; Meier, K. *J. Phys. Chem.* **1986**, *90*, 824-834.
- (14) Yan, H.; Yang, J.; Ma, G.; Wu, G.; Zong, X.; Lei, Z.; Shi, J.; Li, C. *J. Catal.* **2009**, *266*, 165-168.

- (15) Maeda, K.; Domen, K. *J. Phys. Chem. C* **2007**, *111*, 7851-7861.
- (16) Sato, S.; White, J. M. *Chem. Phys. Lett.* **1980**, *72*, 83-86.
- (17) Yamaguti, K.; Sato, S. *J. Chem. Soc. Farad. Trans.* **1985**, *81*, 1237-1246.
- (18) Hitoki, G.; Takata, T.; Kondo, J. N.; Hara, M.; Kobayashi, H.; Domen, K. *Chem. Commun.* **2002**, 1698-1699.
- (19) Kato, H.; Asakura, K.; Kudo, A. *J. Am. Chem. Soc.* **2003**, *125*, 3082-3089.
- (20) Inoue, Y.; Niizuma, T.; Asai, Y.; Sato, K. *J. Chem. Soc. Chem. Comm.* **1992**, 579-580.
- (21) Maeda, K.; Teramura, K.; Lu, D. L.; Takata, T.; Saito, N.; Inoue, Y.; Domen, K. *Nature* **2006**, *440*, 295-295.
- (22) Kim, H. G.; Becker, O. S.; Jang, J. S.; Ji, S. M.; Borse, P. H.; Lee, J. S. *J. Solid State Chem.* **2006**, *179*, 1214-1218.
- (23) Kudo, A.; Kato, H. *Chem. Lett.* **1997**, 421-422.
- (24) Zou, Z. G.; Arakawa, H. *J. Photochem. Photobio. A* **2003**, *158*, 145-162.

# **Chapter 2**

## **An Introduction to Semiconductor-based Photocatalysts and Approaches of Band-gap Engineering**

### **2.1 Wide Band Gap Photocatalysts with UV Light Activity**

As mentioned in Chapter 1, not all semiconductors can perform photocatalytic reactions since there are many strict requirements for water splitting. Wide band gap semiconductors meet all these requirements theoretically. In fact, these semiconductors were the first to be discovered. Although these photocatalysts with wide band gaps only have UV activity and limited practical applications, these studies do trigger the formation of this research field and contribute a lot to the establishment of many theories in photocatalysis. The wide band gap photocatalysts mainly consist of the semiconductors with  $d^0$  and  $d^{10}$  electronic configurations.

#### **2.1.1 Metal Oxides with $d^0$ Electronic Configuration**

This is the biggest family of wide band gap photocatalysts. They can be further categorized into Group 4 metal oxides, Group 5 metal oxides and other metal oxides with  $d^0$  electronic configuration.

i) Group 4 metal oxides.  $TiO_2$  is the most famous photocatalyst since the discovery of the Honda-Fujishima effect in 1972.<sup>1</sup> The overall water splitting was achieved under UV irradiation by using a photoelectrochemical cell with an n-type  $TiO_2$  electrode and

some external bias. Photocatalytic water splitting even cannot proceed on unmodified  $\text{TiO}_2$  loaded with platinum (Pt) co-catalysts due to the 'back reaction' although Pt is usually an excellent co-catalyst for the reduction of  $\text{H}^+$ . The back reaction arises because Pt can also function as a catalyst for the rapid formation of  $\text{H}_2\text{O}$  from the generated  $\text{H}_2$  and  $\text{O}_2$ . In order to suppress the back reaction,  $\text{NaOH}$  was coated on  $\text{TiO}_2$  and the modified photocatalysts successfully decomposed water vapor into  $\text{H}_2$  and  $\text{O}_2$ .<sup>2</sup>  $\text{Pt-TiO}_2$  can also perform photocatalytic water splitting by adding a large amount of carbonates (e.g.  $\text{Na}_2\text{CO}_3$ ) to the reaction system.<sup>3</sup> Complex photoreactions with carbonates and photocatalytic redox reactions on the  $\text{TiO}_2$  under UV light both contribute to the achievement of overall water splitting. Inspired by the success of  $\text{TiO}_2$ , many other  $\text{Ti}^{4+}$ -containing oxide photocatalysts were explored, such as  $\text{SrTiO}_3$ ,<sup>4</sup>  $\text{Sr}_3\text{Ti}_2\text{O}_7$ ,<sup>5</sup>  $\text{Sr}_4\text{Ti}_3\text{O}_{10}$ ,<sup>6</sup>  $\text{La}_2\text{Ti}_2\text{O}_7$ ,<sup>7</sup> Ba-doped  $\text{La}_2\text{Ti}_2\text{O}_7$ ,<sup>8</sup>  $\text{KLaZr}_{0.3}\text{Ti}_{0.7}\text{O}_4$ <sup>9</sup> and  $\text{La}_4\text{CaTi}_5\text{O}_{17}$ .<sup>7</sup> The typical character is that they all have layered perovskite structures and wide band gaps. The layered structure is convenient for electron migration. Therefore, these photocatalysts can usually provide high quantum yields for the photocatalytic water splitting under UV light. Although these photocatalysts have limited practical application due to their wide band gaps, some interesting studies have been carried out based on the representative  $\text{SrTiO}_3$ .  $\text{NiO/Ni}$  (denoted as  $\text{NiO}_x$ ) loaded  $\text{SrTiO}_3$ <sup>4</sup> shows good performance for water splitting because  $\text{NiO}_x$  co-catalysts can suppress back reaction

between H<sub>2</sub> and O<sub>2</sub>, which is distinct from Pt co-catalyst. Therefore, the NiO<sub>x</sub> co-catalyst has often been used with many overall water splitting photocatalysts later on. For example, NiO<sub>x</sub> loaded A<sub>2</sub>La<sub>2</sub>Ti<sub>3</sub>O<sub>10</sub> (A= K or Rb) exhibits excellent activity for overall water splitting under UV irradiation.<sup>10</sup> Holes are generated in the layered perovskite and oxidize water to O<sub>2</sub> and photogenerated electrons reduce H<sup>+</sup> to H<sub>2</sub> through the NiO<sub>x</sub> co-catalyst particles loaded on the external surface of the photocatalysts. The excellent performance is due to the efficient charge separation because the H<sub>2</sub> and O<sub>2</sub> evolution occurs at different reaction sites.

Besides TiO<sub>2</sub> and Ti<sup>4+</sup>-containing photocatalysts, ZrO<sub>2</sub> is another important photocatalyst for water splitting in group 4. ZrO<sub>2</sub> is actually able to promote overall photocatalytic water splitting even without loading any co-catalysts.<sup>11</sup> ZrO<sub>2</sub> has a very large band gap (*ca.* 5 eV) and the potentials of the CB and VB edges locate at -1 and +4 V vs. NHE at pH=0, respectively. The unique band structures count for the unique photocatalytic properties of ZrO<sub>2</sub>.

ii) Group 5 metal oxides. Many Nb<sup>5+</sup> and Ta<sup>5+</sup> containing oxides have been reported for photocatalytic water splitting. For Nb<sup>5+</sup> oxides, K<sub>4</sub>Nb<sub>6</sub>O<sub>17</sub>,<sup>12</sup> Rb<sub>4</sub>Nb<sub>6</sub>O<sub>17</sub>,<sup>13</sup> Ca<sub>2</sub>Nb<sub>2</sub>O<sub>7</sub>,<sup>7</sup> Sr<sub>2</sub>Nb<sub>2</sub>O<sub>7</sub>,<sup>7</sup> Ba<sub>5</sub>Nb<sub>4</sub>O<sub>15</sub>,<sup>14</sup> NaCa<sub>2</sub>Nb<sub>3</sub>O<sub>10</sub>,<sup>15</sup> ZnNb<sub>2</sub>O<sub>6</sub>,<sup>16</sup> Cs<sub>2</sub>Nb<sub>4</sub>O<sub>11</sub><sup>17</sup> and La<sub>3</sub>NbO<sub>7</sub><sup>18</sup> can drive overall water splitting under UV irradiation. Even more Ta<sup>5+</sup> containing oxides are active photocatalysts under UV light, such as Ta<sub>2</sub>O<sub>5</sub>,<sup>11(b)</sup>

$K_2PrTa_5O_{15}$ ,<sup>19</sup>  $K_3Ta_3B_2O_{12}$ ,<sup>20</sup>  $LiTaO_3$ ,<sup>21</sup>  $NaTaO_3$ ,<sup>22</sup>  $KTaO_3$ ,<sup>22</sup>  $AgTaO_3$ ,<sup>23</sup> Zr-doped  $KTaO_3$ ,<sup>24</sup> La-doped  $NaTaO_3$ ,<sup>25</sup> Sr-doped  $NaTaO_3$ ,<sup>26</sup>  $Na_2Ta_2O_6$ ,<sup>27</sup>  $K_2Ta_2O_6$ ,<sup>28</sup>  $CaTa_2O_6$ ,<sup>29</sup>  $SrTa_2O_6$ ,<sup>29</sup>  $BaTa_2O_6$ ,<sup>29</sup>  $NiTa_2O_6$ ,<sup>30</sup>  $Rb_4Ta_6O_{17}$ ,<sup>13</sup>  $Ca_2Ta_2O_7$ ,<sup>27</sup>  $Sr_2Ta_2O_7$ ,<sup>31</sup>  $K_2SrTa_2O_7$ ,<sup>32</sup>  $RbNdTa_2O_7$ ,<sup>33</sup>  $H_2La_{2/3}Ta_2O_7$ ,<sup>34</sup>  $K_2Sr_{1.5}Ta_3O_{10}$ ,<sup>35</sup>  $LiCa_2Ta_3O_{10}$ ,<sup>36</sup>  $KBa_2Ta_3O_{10}$ ,<sup>7</sup>  $Sr_5Ta_4O_{15}$ ,<sup>31</sup>  $Ba_5Ta_4O_{15}$ ,<sup>37</sup>  $H_{1.8}Sr_{0.81}Bi_{0.19}Ta_2O_7$ ,<sup>38</sup> Mg-Ta oxide,<sup>39</sup>  $LaTaO_4$ ,<sup>40</sup> and  $La_3TaO_7$ .<sup>18</sup> Similar to  $ZrO_2$ ,  $Ta^{5+}$  containing photocatalysts usually have very large band gaps and therefore can exhibit photocatalytic water splitting without any co-catalysts. Among the  $Ta^{5+}$  containing photocatalysts,  $ATaO_3$  ( $A=Li$ ,  $Na$ , or  $K$ ) was heavily studied.<sup>22</sup>  $NaTaO_3$  has much better performance than  $LiTaO_3$  and  $KTaO_3$ . The high activity of  $NaTaO_3$  can be attributed to the suitable conduction band level consisting of  $Ta$  5d and energy delocalization caused by the slight distortion of  $TaO_6$  connections. It is also found that La(2%)-doped  $NaTaO_3$  has much higher activity than non-doped  $NaTaO_3$ .<sup>41</sup> There are two major advantages by La-doping. First, the La-doped  $NaTaO_3$  particles are not only small but also have high crystallinity, which both favor the charge separation of the photocatalysts. Secondly, La-doping can create the ordered nanosteps on the particle surface.  $H_2$  evolution sites at nanostep edges are effectively separated from the  $O_2$  evolution sites at the groove of the nanostep structure. The back reaction between  $H_2$  and  $O_2$  are therefore effectively suppressed. By studying the photocatalyst of La-doped  $NaTaO_3$ , morphological characteristics can be a crucial factor to influence the photocatalytic performance.

iii) Other metal oxides with  $d^0$  electronic configuration. Other metal oxides, such as  $\text{PbWO}_4$ ,<sup>42</sup>  $\text{RbWNbO}_6$ ,<sup>43</sup>  $\text{RbWTaO}_6$ ,<sup>43</sup> Sr-doped  $\text{CeO}_2$ ,<sup>44</sup> and  $\text{BaCeO}_3$ ,<sup>45</sup> can also function as photocatalysts for overall water splitting under UV light irradiation.

### 2.1.2 Metal Oxides with $d^{10}$ Electronic Configuration

Although photocatalysts with  $d^0$  electronic configuration dominate the family of wide band gap photocatalysts, the discovery of photocatalysts with  $d^{10}$  electronic configuration changed the conventional concepts and had a major impact on the development of new photocatalysts. The fundamental difference between the  $d^0$  and  $d^{10}$  photocatalysts is their band gap structures. The top levels of the VB and the bottom levels of the CB with  $d^0$  electronic structures are usually composed of O 2p orbitals and transition metal  $d^0$  orbitals, respectively. In contrast, for photocatalysts with  $d^{10}$  electronic configuration, such as  $\text{SrIn}_2\text{O}_4$ ,<sup>46</sup> the top level of the VB consists of O 2p orbitals but the bottom level of the CB consists of hybridized orbitals among the In 5s, In 5p and O 2p orbitals. The hybridized orbitals are broad with large dispersion, which can enhance the mobility of the photoexcited electrons. The representative photocatalysts with  $d^{10}$  electronic configuration are  $\text{NaInO}_2$ ,<sup>47</sup>  $\text{CaIn}_2\text{O}_4$ ,<sup>46</sup>  $\text{SrIn}_2\text{O}_4$ ,<sup>46</sup>  $\text{LaInO}_3$ ,<sup>46</sup>  $\text{Y}_{x}\text{In}_{2-x}\text{O}_3$ ,<sup>48</sup>  $\text{NaSbO}_3$ ,<sup>49</sup>  $\text{CaSb}_2\text{O}_6$ ,<sup>50</sup>  $\text{Ca}_2\text{Sb}_2\text{O}_7$ ,<sup>50</sup>  $\text{Sr}_2\text{Sb}_2\text{O}_7$ ,<sup>50</sup>  $\text{Sr}_2\text{SnO}_4$ ,<sup>49</sup>  $\text{ZnGa}_2\text{O}_4$ ,<sup>51</sup>  $\text{Zn}_2\text{GeO}_4$ ,<sup>50</sup>  $\text{LiInGeO}_4$ ,<sup>52</sup> and  $\text{Ga}_2\text{O}_3$ .<sup>53</sup>

### **2.1.3 Metal Nitrides with d<sup>10</sup> Electronic Configuration**

Derived from metal oxides with d<sup>10</sup> electronic configuration, metal nitrides with d<sup>10</sup> electronic configuration can also function as efficient photocatalysts for water splitting. The representative compounds are Ge<sub>3</sub>N<sub>4</sub>,<sup>54</sup> GaN<sup>55</sup> and Mg-doped GaN.<sup>56</sup> Among these nitrides, β-Ge<sub>3</sub>N<sub>4</sub> exhibits the highest photocatalytic activity for overall water splitting after loading RuO<sub>2</sub> co-catalyst. The quantum efficiency of β-Ge<sub>3</sub>N<sub>4</sub> at around 300 nm can reach as high as *ca.* 9%. Distinct from metal oxide photocatalysts, the VB of metal nitrides consists of N 2p orbitals. Similar to the photocatalysts with d<sup>10</sup> electronic configuration, the CB of these metal nitrides is also composed of hybridized orbitals, Ge 4s4p orbitals in Ge<sub>3</sub>N<sub>4</sub>. The broad hybridized orbitals with large dispersion can enhance the mobility of photogenerated electrons and therefore reduce the possibility of charge recombination, permitting efficient overall water splitting. Although these metal nitrides are all wide band gap semiconductors and only have UV light response, the discoveries guide the later development of visible light responsive photocatalysts.

## **2.2 Visible-light Driven Photocatalysts and Approaches of Band-gap Engineering**

For practical application, photocatalysts with visible light response are the ultimate goal because the energy of UV light only takes up 2% in the whole sunlight spectrum. Besides several native visible-light driven photocatalysts, narrowing the band gap of wide band gap photocatalysts is the main strategy to obtain visible-light responsive

photocatalysts. This is so-called 'band-gap engineering'. The next sections will first briefly summarize the native visible-light photocatalysts and then focus on the different strategies of band-gap engineering.

### 2.2.1 Native Visible-light Driven Photocatalysts

Metal sulfides are believed to be attractive photocatalysts for H<sub>2</sub> evolution with visible light response. The VB of metal sulfides usually consists of S 3p orbitals, the potential level of which is less positive than O 2p orbitals that make up the VB in metal oxides. This is why metal sulfides usually have smaller band gap than corresponding metal oxides and visible light response. Although most of metal sulfides are unstable due to photocorrosion during photocatalysis, suitable hole scavengers, such as S<sup>2-</sup> and SO<sub>3</sub><sup>2-</sup>, can be used to partially suppress the photocorrosion reaction. Extremely high quantum yield can be achieved for some modified metal sulfides. CdS is the representative one and studied in most details. A composite of Pt-PdS modified CdS can achieve a quantum yield of 93% for H<sub>2</sub> evolution at 420 nm using Na<sub>2</sub>S and Na<sub>2</sub>SO<sub>3</sub> as sacrificial agents.<sup>57</sup> Other metal sulfides, such as CuInS<sub>2</sub>,<sup>58</sup> CuIn<sub>5</sub>S<sub>8</sub>,<sup>58</sup> AgGaS<sub>2</sub><sup>59</sup> and AgIn<sub>5</sub>S<sub>8</sub><sup>60</sup> have also been reported for photocatalytic H<sub>2</sub> evolution in the presence of sacrificial reagents. NaInS<sub>2</sub> with layer structure,<sup>61</sup> ZnIn<sub>2</sub>S<sub>4</sub> with spinel structure<sup>62</sup> and indium sulfide compounds with open-framework structure<sup>63</sup> have also been reported. Although metal sulfides usually have high efficiency under visible light response, sacrificial agents have

to be added to suppress the photocorrosion, which confines its practical application. Meanwhile, even with sacrificial agents, they are still lack of long term stability compared to metal oxides photocatalysts.

$\text{WO}_3$ <sup>64</sup> and  $\alpha\text{-Fe}_2\text{O}_3$ <sup>65</sup> with a band gap of ~2.8 eV and ~2.1 eV, respectively, are also important photocatalysts with native visible light response. They are usually used as a photoelectrode (photoanode) in the photoelectrochemical (PEC) cell. The PEC water splitting can be achieved with an external bias under visible light irradiation.

A metal-free photocatalyst, graphitic carbon nitride ( $\text{g-C}_3\text{N}_4$ ), has been reported for efficient photocatalytic  $\text{H}_2$  evolution under visible light irradiation after loading Pt co-catalyst.<sup>66</sup> It can also be fabricated as a photoanode for PEC water splitting with an external bias under visible light irradiation.<sup>67</sup>

The native visible-light driven photocatalysts with long term stability are actually only a few. In order to obtain more photocatalysts with visible light response and long term stability, band-gap engineering is necessary to modify existing wide band gap photocatalysts (based on oxides and nitrides) or fabricate new narrow band gap photocatalysts.

### 2.2.2 Approaches of Band-gap Engineering

Note that although many heterometallic oxides with single phase have been developed for visible-light responsive photocatalytic water splitting, the fabrication of

these photocatalysts is based on the metal-mediated band-gap engineering. Therefore, it can still be included into one of the strategies of band-gap engineering while not the native visible-light driven photocatalysts. Basically, several common approaches of band-gap engineering are: i) metal or/and non-metal doping to narrow the band gap; ii) developing solid solutions to control the band structure; iii) developing single-phase visible-light active photocatalysts through metal-mediated band-gap engineering; iv) other newly explored approaches.

### 2.2.2.1 Metal or/and Non-metal Doping

Doping external ions is one of the most effective strategies to create impurity levels in the forbidden band and therefore narrow the band gap. Metal or non-metal ions are usually doped or co-doped into wide band gap photocatalysts. Upon doping, either a donor level above the original VB or an acceptor level below the original CB can be created to make the photocatalysts visible-light active as shown in Figure 2.1.

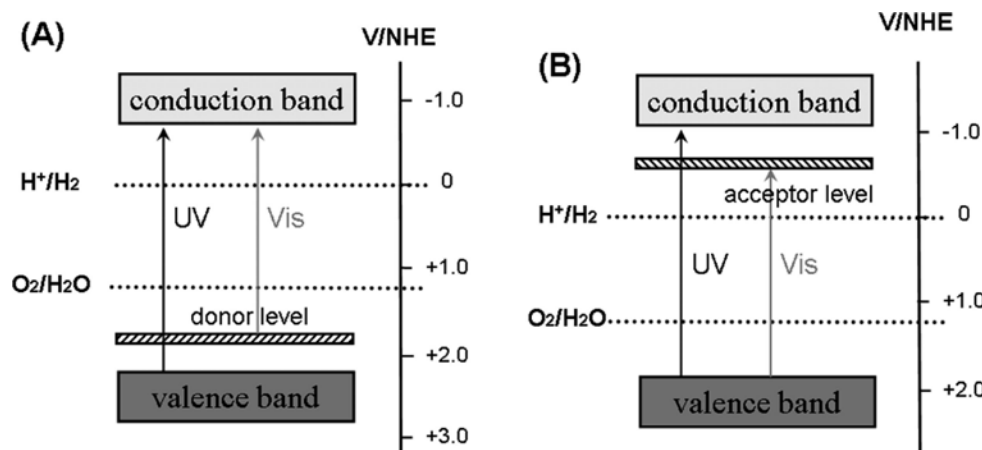


**Figure 2.1** Donor level (A) and acceptor level (B) formed by metal ion doping. Reprinted with permission from Ref. 68. Copyright American Chemical Society 2010.

Since  $\text{TiO}_2$  and  $\text{Ti}^{4+}$  containing semiconductors were first discovered and heavily studied as UV responsive photocatalysts, doping strategy was first applied to these materials to form visible-light responsive photocatalysts.  $\text{Cr}^{5+}$  ions were successfully doped into  $\text{TiO}_2$  as early as 1982.<sup>69</sup> Later on, various 3d metal ions, such as V, Ni, Mo, Fe, Sn, Mn, and so on,<sup>70</sup> were doped into  $\text{TiO}_2$  to improve its visible-light absorption and photocatalytic performance. The effects of metal ion dopants were then widely studied in details. Doping some transition metals, such as V, Cr, Mn, Fe and Ni, into  $\text{TiO}_2$  would result in not only better absorption of visible light but also effective photocatalytic reaction under both UV and visible light irradiation.<sup>71</sup>  $\text{Pt}^{4+}$  and  $\text{Ag}^+$  doped  $\text{TiO}_2$  exhibited similar photocatalytic properties.<sup>72</sup> Conclusively, it is believed that the doping ions in these photocatalysts not only contributed to the visible-light absorption but also served as a recombination inhibitor by trapping photogenerated electrons or holes, which in return promoted the charge separation required for the photocatalytic water splitting. However, in more other cases, metal-ion dopants would inevitably create defects in the photocatalysts and be considered as the recombination sites for photoinduced charges, which results in low photocatalytic performance compared to single-phase photocatalysts.  $\text{Ni}^{2+}$ ,  $\text{Rh}^{3+}$  and  $\text{Cr}^{3+}$  doped  $\text{TiO}_2$  exhibited virtually no photocatalytic activity because the dopants create defects in the crystalline photocatalysts and act as the recombination sites for the photoinduced charges. However,  $\text{TiO}_2$  codoped by  $\text{Ni}^{2+}$ ,  $\text{Rh}^{3+}$ , or  $\text{Cr}^{3+}$  together

with  $Ta^{5+}$ ,  $Nb^{5+}$ , or  $Sb^{5+}$  would result in efficient photocatalytic  $O_2$  evolution from water.<sup>73</sup> It can be explained that codoping highly charged metal ions can balance the charge in the photocatalysts, reduce crystalline defects and in return suppress the recombination between the photoinduced electrons and holes. Other  $Ti^{4+}$  containing photocatalysts, such as  $SrTiO_3$ ,<sup>74</sup>  $CaTiO_3$ ,<sup>75</sup>  $La_2Ti_2O_7$ ,<sup>76</sup>  $K_2La_2Ti_3O_{10}$ <sup>77</sup> and  $In_2TiO_5$ ,<sup>78</sup> have also been doped with various metal ions to achieve photocatalytic water splitting under visible light irradiation.

Besides metal oxides in group 4, photocatalysts in group 5 are also intensively studied by doping strategy. A famous photocatalyst is  $InTaO_4$  doped by different metal ions (Mn, Fe, Co, Ni and Cu).<sup>79</sup> Among these doped  $InTaO_4$ ,  $In_{0.9}Ni_{0.1}TaO_4$  exhibited the highest photocatalytic activity, which induced overall water splitting with stoichiometric amounts of oxygen and hydrogen under visible light irradiation. The quantum yield can reach ~0.66% at 402 nm.<sup>79(a)</sup> Other metal oxides in group 5, such as  $K_4Nb_6O_{10}$ ,<sup>80</sup>  $BiTaO_4$ <sup>81</sup> and  $NaAO_3$  ( $A=Nb$ ,  $Ta$ ),<sup>82</sup> have been doped with various metal ions and their photocatalytic performance under visible light is improved.

Non-metal ion doping is another approach to modify the wide band gap photocatalysts. Unlike the metal ion doping, non-metal doping usually shift the VB edge upward and therefore narrow the band gap as indicated in Figure 2.2.

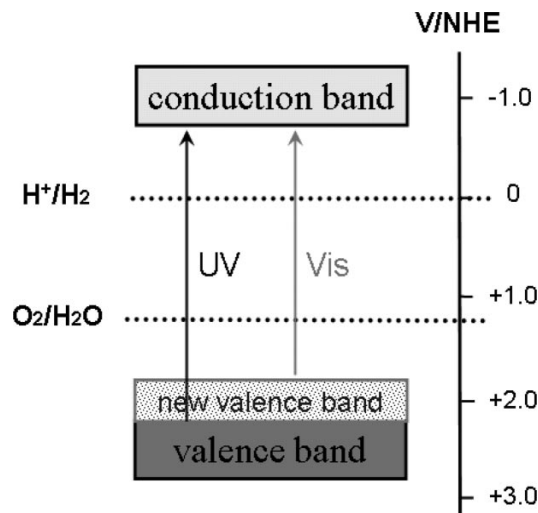


**Figure 2.2** New valence band formation by doping of non-metal ions. Reprinted with permission from Ref. 68. Copyright American Chemical Society 2010.

This strategy was also first fulfilled by doping  $\text{TiO}_2$  photocatalyst. Various non-metal ions (such as C, N, S etc.) were doped into  $\text{TiO}_2$  and the resultant products were studied for their optical and photocatalytic properties.<sup>83</sup> By theoretical study on N-doped  $\text{TiO}_2$ , the hybridization of N 2p and O 2p orbitals will move the VB edge upward and lead to the narrowing of the band gap. X-ray photoelectron spectroscopy (XPS) study on C, N, and S-doped  $\text{TiO}_2$  also indicates that additional electronic states exist above the VB edge of pure  $\text{TiO}_2$ . Besides Ti-based oxides,<sup>84</sup> the strategy of non-metal ion doping has been widely used to modify other wide band gap photocatalysts, such as Ta-based oxides,<sup>85</sup> Zr-based oxides,<sup>86</sup> Nb-based oxides,<sup>87</sup> etc.

To extend the doping strategy, co-doping metal/non-metal ion couples have also been studied. Different charge-compensated donor-acceptor pairs such as (N + V), (Nb + N), (Cr + C) and (Mo + C) have been used to co-dope  $\text{TiO}_2$ .<sup>88</sup> Among them, (Mo + C)

doped  $\text{TiO}_2$  exhibits best performance of photocatalytic water splitting because it reduces the band gap to the ideal visible light region.

Note that doping is the earliest approach of band-gap engineering and it is also the most intensively studied. It is very effective to narrow the band gap of many UV-active photocatalysts. However, as mentioned above, dopants are more likely to create defects and act as the recombination sites in the photocatalysts, which reduces the photocatalytic performance. Therefore, other approaches have to be developed.

### 2.2.2.2 Developing Solid Solutions

Forming solid solution between wide and narrow band gap semiconductors is an effective approach to control the band structure of the photocatalysts. This method can not only narrow the band gap but also adjust the band positions by varying the ratio of the compositions of the semiconductors in the solid solution. Figure 2.3 shows the controllable band structures by forming a solid solution.

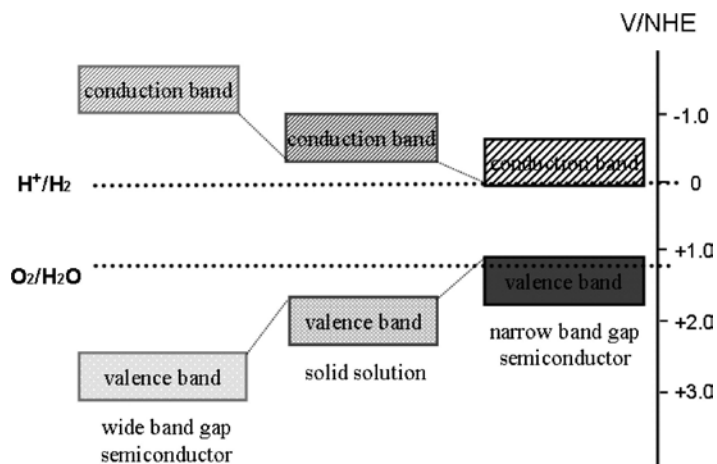


**Figure 2.3** Band structure controlled by making a solid solution. Reprinted with permission from Ref. 68. Copyright the American Chemical Society 2010.

The most important solid solution ' $(\text{Ga}_{1-x}\text{Zn}_x)(\text{N}_{1-x}\text{O}_x)$ ' for photocatalytic water splitting under visible light was developed by Domen K. and co-workers in 2005.<sup>89</sup> Since it is a solid solution formed by an oxide and a nitride, it is called oxynitride solid solution. Both GaN and ZnO have wide band gaps. So, the solid solution of the two compounds should have great band gap energy ( $> 3.0$  eV). However, the p-d repulsion between the N 2p and Zn 3d orbitals shifted the VB maximum upward without affecting the CB minimum. This would narrow the band gap of GaN-ZnO solid solution as schematically depicted in Figure 4. By adjusting the ratio of the compositions of the two semiconductors (the value of 'X'), the band gap of the solid solution can be tuned as shown in Figure 2.4.

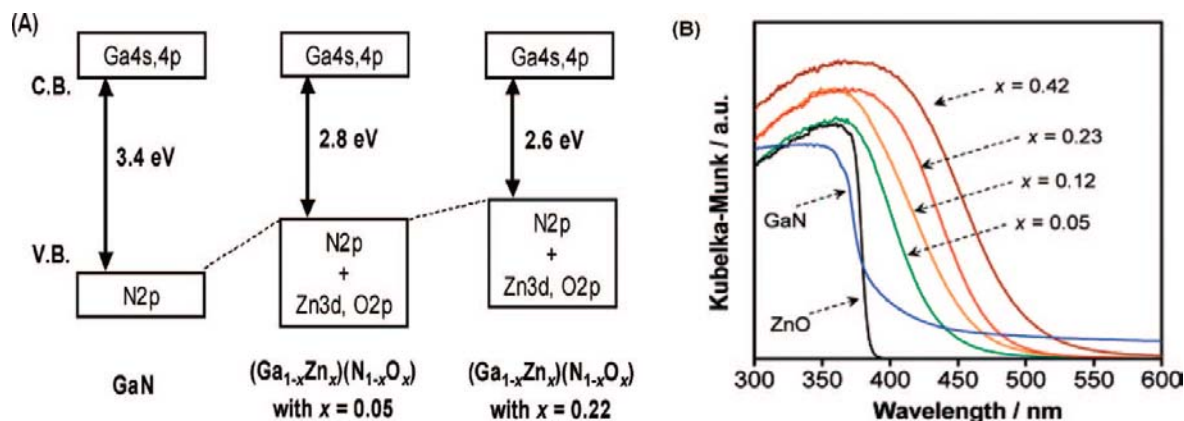


**Figure 2.4** (A) Schematic band structures. Reprinted with permission from Ref. 90. Copyright 2005 American Chemical Society. (B) UV-visible diffuse reflectance spectra of  $(\text{Ga}_{1-x}\text{Zn}_x)(\text{N}_{1-x}\text{O}_x)$ . Reprinted with permission from Ref. 91. Copyright 2007 American Chemical Society.

Importantly, the band structure of  $(\text{Ga}_{1-x}\text{Zn}_x)(\text{N}_{1-x}\text{O}_x)$  was suitable for overall water splitting under visible light irradiation. The quantum efficiency at 420-440 nm was about

2.5% after loading  $\text{Rh}_{2-y}\text{Cr}_y\text{O}_3$  as a co-catalyst. With the loading of  $\text{Rh}_{2-y}\text{Cr}_y\text{O}_3$  co-catalyst, the charge recombination was inhibited, and the  $\text{O}_2$  evolution reaction was enhanced. In addition, post-calcination treatment can further improve the photocatalytic performance of  $\text{Rh}_{2-y}\text{Cr}_y\text{O}_3/(\text{Ga}_{1-x}\text{Zn}_x)(\text{N}_{1-x}\text{O}_x)$  under visible light irradiation.<sup>89(b)</sup> It is due to the fact that post-calcination treatment can reduce the density of the zinc- and/or oxygen-related defects that functioned as recombination centers for photogenerated electrons and holes in the material. The highest quantum efficiency obtained by post-calcination treatment can reach as high as *ca.* 5.9% at 420-440 nm. The solid solution of  $(\text{Ga}_{1-x}\text{Zn}_x)(\text{N}_{1-x}\text{O}_x)$  is a representative oxynitride solid solution. Other oxynitride solid solutions have also been developed. The solid solution of  $(\text{Zn}_{1+x}\text{Ge})(\text{N}_2\text{O}_x)$  can also perform photocatalytic overall water splitting under visible light irradiation.<sup>92</sup> Additionally, InN was used to form oxynitride solid solution with  $(\text{Ga}_{1-x}\text{Zn}_x)(\text{N}_{1-x}\text{O}_x)$ .<sup>93</sup> However, the resultant Ga-Zn-In mixed oxynitride solid solution can only photocatalyze half water splitting reaction in the presence of appropriate sacrificial agents.

Besides the oxynitride solid solutions, sulfide or oxysulfide solid solutions have also been developed. Similarly to metal sulfide photocatalysts, these compounds usually have really high photocatalytic activity for  $\text{H}_2$  evolution under visible light. However, due to small redox potential of  $\text{S}/\text{S}^{2-}$ , these solid solutions are usually not able to photocatalyze  $\text{O}_2$  evolution and instable during photocatalysis. The solid solution of

$\text{Cd}_{1-x}\text{Zn}_x\text{S}$  ( $x=0.2$ ) exhibited the highest quantum yield of 10.23% at 420 nm for  $\text{H}_2$  evolution even without loading any co-catalysts.<sup>94</sup>  $\text{ZnS}$  and  $\text{MInS}_2$  ( $\text{M}=\text{Cu}$  or  $\text{Ag}$ ) can form a series of sulfide solid solutions.<sup>95</sup> The apparent quantum yields of Pt-loaded  $(\text{AgIn})_{0.22}\text{Zn}_{1.56}\text{S}_2$  ( $E_g=2.33$  eV) and Pt-loaded  $(\text{CuIn})_{0.09}\text{Zn}_{1.82}\text{S}_2$  ( $E_g=2.35$  eV) amounted to 20% and 12.5% at 420 nm, respectively. Another series of sulfide solid solutions is  $\text{A}_2\text{ZnBS}_4$  ( $\text{A}=\text{Cu}$  or  $\text{Ag}$ ;  $\text{B}=\text{Sn}$  or  $\text{Ge}$ ). Of these,  $\text{Ag}_2\text{ZnSnS}_4$  is the most active, exhibiting a quantum yield of ~3% at 500 nm.<sup>96</sup> A zincoxysulfide solid solution of  $(\text{ZnS}_{1-x-0.5y}\text{O}_x(\text{OH})_y)$  was developed.<sup>97</sup> It also exhibited high photocatalytic activity for  $\text{H}_2$  evolution even without a noble metal co-catalyst. The apparent quantum yield was *ca.* 3% under visible light irradiation.

The photocorrosion and instability of sulfide-based photocatalysts confine its practical application although most of them show high activity for  $\text{H}_2$  evolution. If the stability of photocatalysts has to be considered, oxide-based photocatalysts are the best choice. Therefore, oxide solid solution have also been developed although their photocatalytic activities are usually lower than sulfide-based photocatalysts. The oxide solid solutions of  $\text{Bi}_x\text{In}_{1-x}\text{TaO}_4$  ( $x = 0.2$ , 0.5, and 0.8) have suitable band gaps of 2.86, 2.71, and 2.74 eV, respectively.<sup>98</sup> Under visible light irradiation, they all can produce  $\text{H}_2$  or  $\text{O}_2$  from water with appropriate sacrificial agents. By combining  $\text{CaMoO}_4$  or  $(\text{Na}_{0.5}\text{Bi}_{0.5})\text{MoO}_4$  with the famous visible-light-active photocatalyst  $\text{BiVO}_4$ ,<sup>99</sup> the

resultant solid solutions showed high activity for photocatalytic O<sub>2</sub> evolution, which is even better than monoclinic BiVO<sub>4</sub>. The solid solution of Y<sub>2</sub>WO<sub>6</sub> and Bi<sub>2</sub>WO<sub>6</sub> or BiYWO<sub>6</sub>, is able to perform overall photocatalytic water splitting under visible light up to  $\lambda < 470$  nm.<sup>100</sup> The Bi 6s and Y 4d contributed to a new VB and CB, respectively. Later, a similar solid solution, Bi<sub>0.5</sub>Dy<sub>0.5</sub>VO<sub>4</sub> prepared from BiVO<sub>4</sub> and DyVO<sub>4</sub> can also stoichiometrically split water into H<sub>2</sub> and O<sub>2</sub> under visible light up to 450 nm.<sup>101</sup>

### **2.2.2.3 Developing Single-phase Visible-light Active Photocatalysts**

Doping and developing solid solution strategies both may introduce defects into the photocatalysts, which is usually considered as recombination centers of charge carriers and reduces the photocatalytic activity. Single-phase photocatalysts are highly preferred in order to improve the photocatalytic performance. Various single-phase photocatalysts with visible light activity have been developed through the metal-mediated band-gap engineering. They are usually heterometallic oxides. The hybridization of the molecular orbitals of some metal ions contributes to the narrowed band gap. Based on the difference of the molecular orbitals of the participating metal ions, this group of photocatalysts can be further divided into d-block, p-block and f-block metal oxides.

i) d-block single-phase photocatalysts. As discussed in doping approach, doping d-block transition metals into the wide band gap photocatalysts can form a separate donor level in the forbidden band. Therefore, it is expected that single-phase heterometallic

oxides containing d-block transition metals may have the similar function.

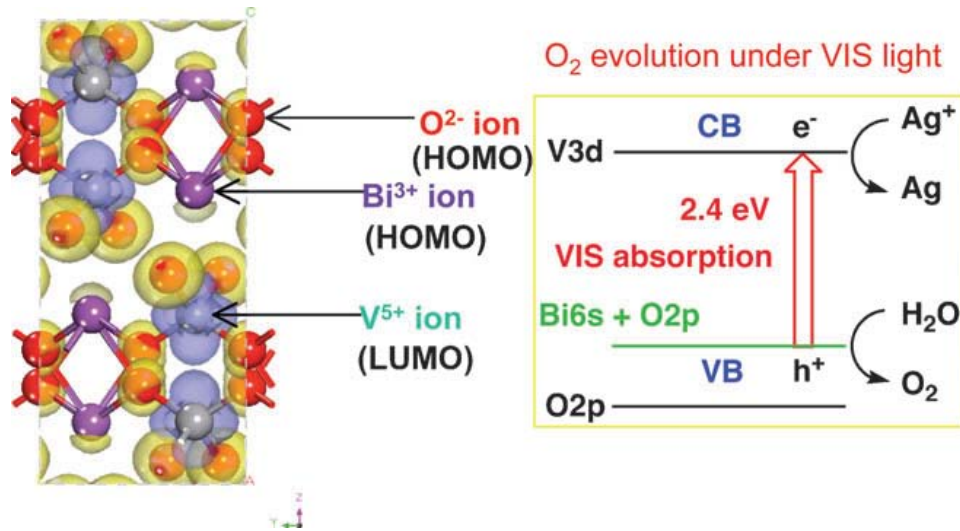


**Figure 2.5** Band structure of  $\text{BiVO}_4$  calculated by DFT. Reprinted with permission from Ref. 103. Copyright 2009 Royal Society of Chemistry.

One well-known group of d-block single-phase heterometallic photocatalysts is the V-containing oxides. The less negative V 3d orbitals contribute to the formation of the CB, lower the CB edge and therefore narrow the band gap.  $\text{BiVO}_4$  is a representative V-containing oxide photocatalyst.<sup>102</sup> As shown in Figure 2.5,<sup>103</sup> the CB of  $\text{BiVO}_4$  consists of V 3d while the VB is formed by the hybridization of O 2p and Bi 6s. Since the CB edge of  $\text{BiVO}_4$  is more positive than the redox potential of  $\text{H}^+/\text{H}_2$ ,  $\text{BiVO}_4$  can only produce  $\text{O}_2$  from water photocatalytically with  $\text{AgNO}_3$  as sacrificial agent under visible light. Some other V-containing oxide photocatalysts may have more negative CB edges than the redox potential of  $\text{H}^+/\text{H}_2$ , such as  $\text{InVO}_4$ ,<sup>104</sup> which enables them to photocatalyze  $\text{H}_2$  from water under visible light. So, depending on the chemical components and crystal structures of different vanadates, the V 3d level is either less negative or more negative

than the H<sub>2</sub> evolution potential. Other V-containing oxide photocatalysts, such as M<sub>3</sub>V<sub>2</sub>O<sub>8</sub> (M=Mg, Ni, Zn),<sup>105</sup> CaBiVMO<sub>8</sub> (M =W, Mo),<sup>106</sup> Bi<sub>2</sub>GaVO<sub>7</sub>,<sup>107</sup> Bi<sub>2</sub>YVO<sub>8</sub>,<sup>108</sup> and BiM<sub>2</sub>VO<sub>6</sub> (M=Cu, Zn),<sup>109</sup> M<sub>2.5</sub>VMoO<sub>8</sub> (M=Mg, Zn),<sup>110</sup> also displayed efficient photocatalytic performance under visible light irradiation.

Either Cr<sup>6+</sup> or Cr<sup>3+</sup> is also used to form single-phase photocatalysts with visible light response based on different mechanisms. Since Cr<sup>6+</sup> has empty 3d orbital, the CB edge of BaCrO<sub>4</sub> is composed of Cr<sup>6+</sup> 3d orbitals. Therefore, the visible light transition is ascribed to the electronic excitation from the VB composed of the O 2p orbitals to the CB composed of the Cr<sup>6+</sup> 3d orbitals.<sup>111</sup> In contrast, Cr<sup>3+</sup> 3d orbitals in BaCr<sub>2</sub>O<sub>4</sub> are partially filled and split into Cr 3d-t<sub>2g</sub> and Cr 3d-e<sub>g</sub> orbitals. The photoexcitation from Cr 3d-t<sub>2g</sub> to Cr 3d-e<sub>g</sub> contributes to the H<sub>2</sub> evolution while the photoexcitation from O 2p orbitals to Cr 3d-t<sub>2g</sub> causes the O<sub>2</sub> evolution reaction.<sup>112</sup> A similar pair of Cr-containing photocatalysts, Ag<sub>2</sub>CrO<sub>4</sub> and AgCrO<sub>2</sub>,<sup>113</sup> also exhibits sufficient photocatalytic activity under visible light irradiation. The Zn/Cr layered double hydroxides (LDH) can perform efficient photocatalytic O<sub>2</sub> generation under visible light irradiation.<sup>114</sup> Its apparent quantum yields can reach as high as 60.9% and 12.2% at 410 nm and 570 nm, respectively.

A series of Ni-containing photocatalysts, such as NiM<sub>2</sub>O<sub>6</sub> (M=Nb, Ta),<sup>115</sup> have been developed for water splitting under visible light irradiation. Similar to the functions

of Cr, it is believed that the Ni d-d transition between the Ni 3d-t<sub>2g</sub> and 3d-e<sub>g</sub> levels played an important role in the visible light response and photocatalytic activity of NiM<sub>2</sub>O<sub>6</sub>.

A series of perovskite type photocatalysts, MCo<sub>1/3</sub>Nb<sub>2/3</sub>O<sub>3</sub> (M=Ca, Sr, and Ba)<sup>116</sup> were found to possess visible light photocatalytic activity due to the hybridization of Co<sup>2+</sup> 3d orbitals and O 2p orbitals. The Fe 3d orbitals of Fe<sup>3+</sup> can also participate in the formation of band structures. After loaded with NiO, Ca<sub>2</sub>Fe<sub>2</sub>O<sub>5</sub> can splitting pure water to generate H<sub>2</sub> under visible light irradiation.<sup>117</sup> Several Ag-based photocatalysts were found to have excellent photocatalytic O<sub>2</sub> evolution activity under visible light. The hybridization of Ag 4d and O 2p orbitals can upward the VB edge and enable visible light adsorption. These photocatalysts are AgTaO<sub>3</sub>,<sup>118</sup> AgNbO<sub>3</sub>,<sup>118</sup> AgInW<sub>2</sub>O<sub>8</sub>,<sup>119</sup>  $\alpha$ -AgGaO<sub>2</sub>,<sup>120</sup> Ag<sub>2</sub>ZnGeO<sub>4</sub>,<sup>121</sup> and AgLi<sub>1/3</sub>M<sub>2/3</sub>O<sub>2</sub> (M=Ti and Sn).<sup>122</sup>

ii) p-block single-phase photocatalysts. Different from d-block photocatalysts, the s orbitals from the outer layer-orbital configurations of p-block metal ions get involved in mediating the band structures. In-containing metal oxides are a big group in this family. MIn<sub>2</sub>O<sub>4</sub> (M=Ca, Sr, Ba) semiconductors are visible light active for water splitting.<sup>123</sup> For these In-containing photocatalysts, the VB was composed of O 2p orbitals, while the CB was mainly composed of the In 5s orbitals. However, it is different for InMO<sub>4</sub> (M=Ta, Nb) photocatalysts.<sup>124</sup> InMO<sub>4</sub> contains two kinds of octahedra, InO<sub>6</sub> and MO<sub>6</sub>. The VB is

believed to be a combination of both the O 2p levels of  $\text{InO}_6$  and  $\text{NbO}_6$  octahedrons, which locates about 1.1 eV more positive than that of the O 2p levels. The  $\text{NiNb}_2\text{O}_6$  has a similar case as  $\text{InMO}_4$ ,<sup>115</sup> the VB of which is attributable to both the O 2p levels of  $\text{NiO}_6$  and  $\text{NbO}_6$  octahedra.

Another big group of p-block metal oxides is Bi-containing semiconductors. Through solid state reaction of  $\text{Bi}_2\text{O}_3$  and  $\text{TiO}_2$ , a visible-light-active polycrystalline  $\text{Bi}_{12}\text{TiO}_{20}$  can be obtained.<sup>125</sup> Its band gap is narrowed to be 2.78 eV by introducing the p-block transition metal Bi. The VB of  $\text{Bi}_{12}\text{TiO}_{20}$  originates from the hybridization of the Bi 6s and O 2p orbitals, which shifts the VB edge upward and narrows band gap. Similarly, for other visible-light-responsive Bi(III)-containing photocatalysts, such as  $\text{CaBi}_2\text{O}_4$ ,<sup>126</sup>  $\text{Bi}_2\text{WO}_6$ ,<sup>127</sup>  $\text{Bi}_2\text{MoO}_6$ ,<sup>128</sup>  $\text{BiSbO}_4$ ,<sup>129</sup> and  $\text{Bi}_2\text{MNB}_7$  (M=Al, Ga, In),<sup>130</sup> the VB also involves the hybridized orbitals between the Bi 6s and the O 2p orbitals, which plays an important role in their visible-light absorption and photocatalytic activities. A Bi (V) photocatalyst,  $\text{NaBiO}_3$ , was also found to be photoactive under visible light for water splitting.<sup>131</sup> The band structure of the VB in  $\text{NaBiO}_3$ , mainly composed of O 2p orbitals, is quite different from that of Bi(III)-containing oxides because the latter is composed of hybridized orbitals between the Bi 6s and the O 2p orbitals at the top of the VB. The reason is that the contribution of the empty  $\text{Bi}^{5+}$  6s orbitals in  $\text{NaBiO}_3$  to the VB is much smaller than the filled  $\text{Bi}^{3+}$  6s orbitals in the  $\text{Bi}^{3+}$ -containing oxides.

The p-block metal ion of lead is effective to mediate the band structure. Two binary lead niobates,  $\text{Pb}_3\text{Nb}_2\text{O}_8$  and  $\text{Pb}_3\text{Nb}_4\text{O}_{13}$ ,<sup>132</sup> were developed as visible-light-active photocatalysts. The hybridization of the Pb 6s and O 2p orbitals in these lead niobates shifted the position of the VB edge upward and narrowed the band gap, leading to the visible light responses. The substitution effects of Pb ions were investigated in details based on various UV-light-active photocatalysts:  $\text{CaBi}_4\text{Ti}_4\text{O}_{15}$ ,  $\text{CaBi}_2\text{Nb}_2\text{O}_9$ ,  $\text{Sr}_3\text{Ti}_2\text{O}_7$  and  $\text{K}_{0.5}\text{La}_{0.5}\text{Ca}_{1.5}\text{Nb}_3\text{O}_{10}$ .<sup>133</sup> Their Pb-containing analogues ( $\text{PbBi}_4\text{Ti}_4\text{O}_{15}$ ,  $\text{PbBi}_2\text{Nb}_2\text{O}_9$ ,  $\text{K}_{0.5}\text{La}_{0.5}\text{Ca}_{0.75}\text{Pb}_{0.75}\text{Nb}_3\text{O}_{10}$ ,  $\text{PbTiO}_3$  and  $\text{K}_{0.5}\text{La}_{0.25}\text{Bi}_{0.25}\text{Ca}_{0.75}\text{Pb}_{0.75}\text{Nb}_3\text{O}_{10}$ ) all exhibited sufficient photocatalytic activities for water decomposition under visible light irradiation. Similarly to the lead niobates, this is also attributed to the hybridization of the occupied Pb 6s and O 2p orbitals, shifting the position of the VB edge up and giving a smaller band gap compared to their original lead-free matrix.

The p-block metal ion of  $\text{Sn}^{2+}$  can also function as a band structure mediator to narrow the band gap.  $\text{SnNb}_2\text{O}_6$ <sup>134</sup> and  $\text{SnNbO}_2$ <sup>135</sup> showed the photocatalytic activity under visible light irradiation for  $\text{H}_2$  or  $\text{O}_2$  evolution from an aqueous solution containing methanol or  $\text{AgNO}_3$ , respectively. The position of the VB edge formed from the hybrid orbitals of Sn 5s and O 2p was higher than that consisting of only O 2p orbitals, making  $\text{SnNb}_2\text{O}_6$  active to visible light. The  $\beta$ - $\text{SnWO}_4$  can also function as a visible light active photocatalyst for  $\text{H}_2$  evolution from an aqueous methanol solution.<sup>136</sup> The filled Sn 5s

orbitals contribute to the VB structure of  $\beta$ -SnWO<sub>4</sub>, narrowing its band gap and leading to its visible-light responses.

iii) f-block single-phase photocatalysts. The rare earth 4f orbitals can also tune the electronic structure of metal oxides to achieve visible-light-driven photocatalysts. By studying the band structures and photophysical properties of Bi<sub>2</sub>RNbO<sub>7</sub> (R=Y, rare earth),<sup>137</sup> the R 4f orbitals of the R<sup>3+</sup> ions played an important role in the band structures of these photocatalysts. The visible light absorption was attributable to the R 4f and Nb 4d band transition between the R<sup>3+</sup> and Nb<sup>5+</sup> ions. It was assumed that the partly filled R 4f band in the rare earths could form a new energy level in the band structure, and the 4f-d transition resulted in the narrowed band gaps of these photocatalysts. The band structures of R<sub>2</sub>Ti<sub>2</sub>O<sub>7</sub> (R = rare earth: La, Pr, Nd) are also greatly influenced by the 4f band of rare earths.<sup>138</sup> It was found that the R 4f level in R<sub>2</sub>Ti<sub>2</sub>O<sub>7</sub> was shifted to a lower energy as the number of 4f electrons increased, which decreased the band gap energy of both Pr<sub>2</sub>Ti<sub>2</sub>O<sub>7</sub> and Nd<sub>2</sub>Ti<sub>2</sub>O<sub>7</sub>. Other rare earth containing photocatalysts, R<sub>2</sub>M<sub>2</sub>O<sub>7</sub> (R=La, Pr, Nd, Sm, Gd, Dy, Ho, Er, and Yb; M=Ti, Zr), exhibit a similar situation.<sup>139</sup> A series of Ce-containing metal oxide photocatalysts, K<sub>4</sub>Ce<sub>2</sub>M<sub>10</sub>O<sub>30</sub> (M = Ta, Nb),<sup>140</sup> are capable of evolving H<sub>2</sub> or O<sub>2</sub> from aqueous solutions under visible light irradiation ( $\lambda > 420$  nm) with appropriate sacrificial agents, respectively. The DFT study indicates that the CB of K<sub>4</sub>Ce<sub>2</sub>M<sub>10</sub>O<sub>30</sub> (M = Ta, Nb) mainly consists of the Ta 5d (or Nb 4d) orbitals, while the

VB is composed of hybridized O 2p + Ta 5d (or Nb 4d) and occupied Ce 4f orbitals. The Ce 4f orbitals essentially contribute to the narrowed band gaps of these photocatalysts. The pyrochlore-type compound  $\text{Sm}_2\text{InMO}_7$  ( $\text{M} = \text{Ta}, \text{Nb}$ ), with a  $4\text{f}-\text{d}^{10}-\text{d}^0$  configuration, is another new stable visible-light-active photocatalyst for  $\text{H}_2$  evolution.<sup>141</sup> The configuration of  $4\text{f}-\text{d}^{10}-\text{d}^0$  influences not only the crystal but also the electronic structures of these photocatalysts.

#### 2.2.2.4 Other Newly Explored Approaches

Although the above three main approaches of band-gap engineering are quite effective to mediate the band structures and successful to achieve many photocatalysts with visible light response, the approaches of doping and solid solution may introduce crystalline defects and the approach of developing single-phase visible-light-active photocatalysts is confined by the limited choices of mediating metal ions. Therefore, it is still necessary to explore other novel approaches of band-gap engineering to obtain visible-light-responsive photocatalysts with high stability and efficiency.

As introduced above, d-block metal ions are widely used to dope wide band gap photocatalysts or form visible-light-responsive single-phase photocatalysts via mediating the band gaps. Electron transitions between the d orbitals of the d-block metals, which are usually visible-light active, are scarcely studied for photocatalytic water splitting.  $\text{IrO}_2$  nanocrystals are found to exhibit sufficient photocatalytic activity for  $\text{O}_2$  evolution under

both visible light and UV light irradiation.<sup>142</sup> As shown in Figure 2.6 (left), the photocatalytic process is driven by visible excitations from the Ir-d( $t_{2g}$ ) to the Ir-d( $e_g$ ) band (1.5-2.75 eV) and by UV excitations from the O 2p band to the Ir-d( $e_g$ ) (>3.0 eV) band. With aqueous persulfate and silver nitrate solution as sacrificial agents, the non-sensitized  $\text{IrO}_2$  particles can evolve  $\text{O}_2$  with a initial rate up to 0.96  $\mu\text{mol}/\text{min}$  and a quantum efficiency of at least 0.19% at 530 nm.

Based on the similar mechanism of d-d transition absorptions of noble metals,  $\text{Rh}^{3+}$ -doped  $\text{ZnGa}_2\text{O}_4$  also exhibits sufficient  $\text{H}_2$  or  $\text{O}_2$  evolution with appropriate sacrificial agents under visible light.<sup>143</sup> The  $\text{Rh}^{3+}$  ion ( $\text{Rh } d^6$ ) in a regular octahedral coordination can form fully occupied  $t_{2g}^6$  and empty  $e_g^0$  as a result of ligand-field splitting. As shown in Figure 2.6 (right), due to the suitable potentials of the midgap states created by  $t_{2g}^6$  and  $e_g^0$ , the photocatalyst can produce either  $\text{H}_2$  or  $\text{O}_2$  in the presence of sacrificial agents under visible light irradiation. Although the photocatalytic activities of the above two reports are not very high, they provide a new approach of band-gap engineering, e.g. d-d transition absorptions of transition metals. The midgap states formed by the d orbitals of the transition metals can not only entitle the visible light response to the photocatalysts but also perform photocatalytic water splitting due to their suitable potentials. However, the above reports both utilize the d-d transition absorptions of noble metal ions and the exploration of other d-d transition absorptions based on cheap transition metal ions is

quite necessary.

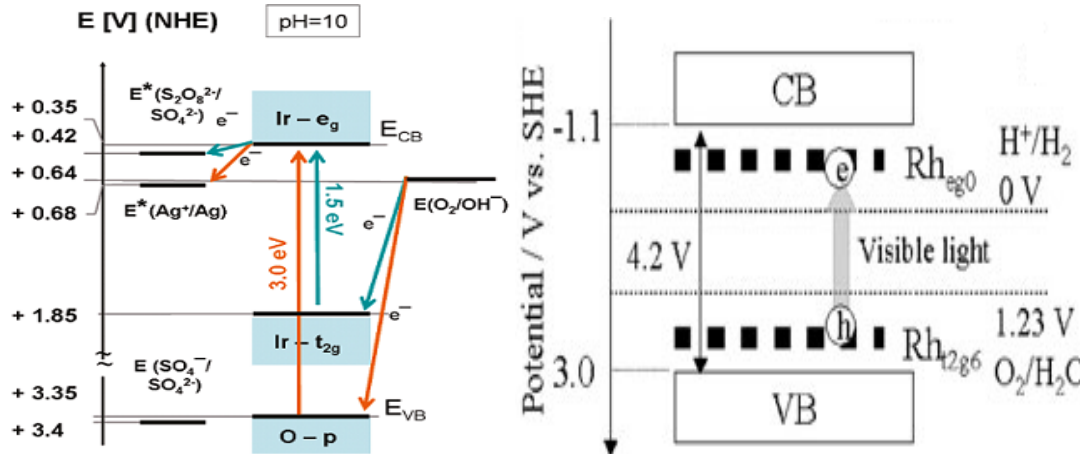


**Figure 2.6** Left: Energy scheme for  $\text{IrO}_2$ , showing optical transitions and electron transfer processes.; Right: Schematic band structure of  $\text{Rh}^{3+}$ -doped  $\text{ZnGa}_2\text{O}_4$ . Reprinted with permission from Ref. 142 and Ref. 143. Copyright 2011 American Chemical Society and 2011 Royal Society of Chemistry.

Another interesting and newly explored approach of band-gap engineering is to introduce significant surface disorder to narrow the band gap. The two stories are both based on  $\text{TiO}_2$  photocatalysts. A so-called 'black  $\text{TiO}_2$ ' was synthesized by treating normal white  $\text{TiO}_2$  nanocrystals in hydrogen gas at  $200^\circ\text{C}$  for 5 days.<sup>144</sup> After the hydrogenation process, a disorder-engineered nano-phase  $\text{TiO}_2$  would consist of two phases: a crystalline  $\text{TiO}_2$  core and a highly disordered surface layer where dopants are introduced. The introduction of disorder and dopants on the surface of nano-phase  $\text{TiO}_2$  would enhance visible and infrared absorption, with the additional benefit of carrier trapping. Large amounts of lattice disorder in semiconductors could yield midgap states whose energy distributions differ from that of a single defect in a crystal. For example, instead of forming discrete donor states near the CB edge, these midgap states can form a

continuum extending to and overlapping with the CB edge; thus they are often also known as band tail states.

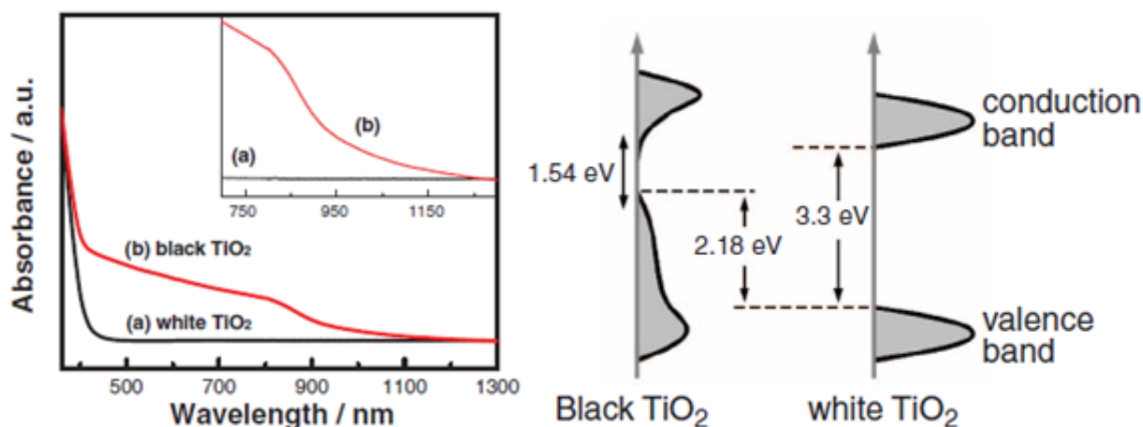


**Figure 2.7** Left: Spectral absorbance of the white and black  $\text{TiO}_2$  nanocrystals. The inset enlarges the absorption spectrum in the range from approximately 750 to 1200 nm. Right: Schematic illustration of the DOS of disorder-engineered black  $\text{TiO}_2$  nanocrystals, as compared to that of unmodified  $\text{TiO}_2$  nanocrystals. Reprinted with permission from Ref. 144. Copyright 2011 Science Magazine.

As shown in Figure 2.7, the density of states (DOS) calculations indicate that the VB edge of 'black  $\text{TiO}_2$ ' has a significant continuum up-shift compared to white  $\text{TiO}_2$  by as much as 2.18 eV. These extended energy states combining with the energy levels produced by dopants, can contribute to the dominant centers for the optical excitation and relaxation. Another potential advantage of these surface disorders is that they may provide trapping sites for photogenerated carriers and prevent them from rapid recombination, thus promoting electron transfer and photocatalytic reactions. The diffusive reflectance spectroscopy (DRS) revealed that the onset of optical absorption of the hydrogenated  $\text{TiO}_2$  was lowered to about 1.0 eV ( $\sim 1200$  nm). An abrupt change in

both the reflectance and absorbance spectra at  $\sim 1.54$  eV (806.8 nm) indicated that the optical gap of the black  $\text{TiO}_2$  was significantly narrowed by the surface hydrogenation of  $\text{TiO}_2$ .

Instead of creating surface disorder by hydrogenating  $\text{TiO}_2$ , the other study reported that growing a new phase on the surface of rutile  $\text{TiO}_2$  (011) could also result in significant continuum up-shift of its VB edge.<sup>145</sup> Commercial rutile  $\text{TiO}_2$ (011) single crystals were treated by standard surface science procedures, consisting of several cycles of low-energy  $\text{Ar}^+$  ion sputtering and vacuum annealing to  $650$   $^{\circ}\text{C}$ . To prepare the new surface structure, clean samples were annealed within the vacuum chamber in a  $1 \times 10^{-6}$  torr  $\text{O}_2$  atmosphere. The new phase were verified by scanning tunnelling spectroscopy (STS) measurements.

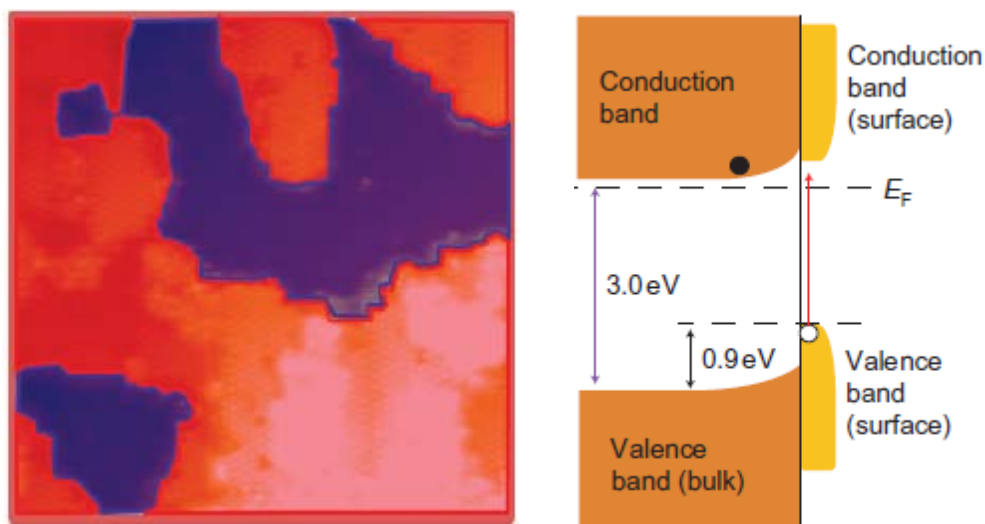


**Figure 2.8** Left: Sample prepared so that both ‘new’ and ‘original’ phases are present simultaneously at the surface (the original surface in blue and the new  $\text{TiO}_2$  phase in red). Right: Band diagram after growing the new phase of  $\text{TiO}_2$ . Reprinted with permission from Ref. 145. Copyright 2011 Nature Publishing Group.

As shown in Figure 2.8, the original phase is in blue and the new phase is in red. The ultraviolet photoemission spectroscopy (UPS) indicates that the VB edge of the pristine surface locates at 3.0 eV, which is consistent with the  $E_f$  being located close to the bottom of the CB. After forming the new surface phase, a new state within the bulk band gap of  $\text{TiO}_2$  is observed, with a maximum at 2.1 eV below  $E_f$ . Moreover, STS spectra revealed that the new phase exhibited filled electronic states that located in the band gap region of rutile  $\text{TiO}_2$ . Therefore, it can be concluded that the formation of the new surface phase up-shifted the VB edge by 0.9 eV as depicted in Figure 8. The continuum up-shift of the VB edge narrows the band gap to ~2.1 eV and matches it closely with the energy of visible light.

The above two reports show a new approach of band-gap engineering, which is introducing surface disorder. The introduction of large surface disorder can result in a continuum up-shift of the VB edge, and thus narrow the band gap, which is superior to conventional band-gap engineering strategies like doping. In conventional methods of band-gap engineering, a discrete energy level between the VB and CB is usually formed, which often serves as recombination sites of the photogenerated charges and reduces the photocatalytic performance.

The new approach of band-gap engineering has only been applied to  $\text{TiO}_2$  so far. There may be many unclear mechanisms behind the approach due to the lack of other

successful materials. Therefore, exploring other novel materials based on the disorder-engineered approach of the band-gap engineering can not only contribute to the enrichment of the new approach but also help to understand the possible mechanisms more profoundly.

### 2.3 References

- (1) Fujishima, A.; Honda, K. *Nature* **1972**, *238*, 37-38.
- (2) Yamaguti, K.; S. Sato, S. *J. Chem. Soc., Faraday Trans. I* **1985**, *81*, 1237-1246.
- (3) Sayama, K.; Arakawa, H. *J. Chem. Soc., Faraday Trans.*, **1997**, *93*, 1647-1654.
- (4) (a) Domen, K.; Naito, S.; Onishi, T.; Tamaru, T.; Soma, M. *J. Phys. Chem.* **1982**, *86*, 3657-3661. (b) Domen, K.; Kudo, A.; Onishi, T.; Kosugi, N.; Kuroda, H. *J. Phys. Chem.* **1986**, *90*, 292-295. (c) Domen, K.; Kudo, A.; Onishi, T. *J. Catal.* **1986**, *102*, 92-98. (d) Kudo, A.; Tanaka, A.; Domen, K.; Onishi, T. *J. Catal.* **1988**, *111*, 296-301.
- (5) Jeong, H.; Kim, T.; Kim, D.; Kim, K. *Int. J. Hydrogen Energy* **2006**, *31*, 1142-1146.
- (6) Ko, Y. G.; Lee, W. Y. *Catal. Lett.* **2002**, *83*, 157-160.
- (7) Kim, H. G.; Hwang, D. W.; Kim, J.; Kim Y. G.; Lee, J. S. *Chem. Commun.* **1999**, 1077-1078.
- (8) Kim, J.; Hwang, D. W.; Kim, H. G.; Bae, S. W.; Lee, J. S.; Li, W.; Oh, S. H. *Top. Catal.* **2005**, *35*, 295-303.
- (9) Reddy, V. R.; Hwang, D. W.; Lee, J. S. *Catal. Lett.* **2003**, *90*, 39-43.
- (10) (a) Takata, T.; Furumi, Y.; Shinohara, K.; Tanaka, A.; Hara, M.; Kondo, J. N.; Domen, K. *Chem. Mater.* **1997**, *9*, 1063-1064. (b) Ikeda, S.; Hara, M.; Kondo, J. N.; Domen, K.; Takahashi, H.; Okubo, T.; Kakihana, M. *Chem. Mater.* **1998**, *10*, 72-77.
- (11) (a) Sayama, K.; Arakawa, H. *J. Phys. Chem.* **1993**, *97*, 531-533. (b) Sayama, K.; Arakawa, H. *J. Photochem. Photobiol. A* **1994**, *77*, 243-247. (c) Sayama, K.; Arakawa, H. *J. Photochem. Photobiol. A* **1996**, *94*, 67-74. (d) Zou, J. J.; Liu, C. J.; Zhang, Y. P. *Langmuir* **2006**, *22*, 2334-2339.
- (12) Domen, K.; Kudo, A.; Shinozaki, A.; Tanaka, A.; Maruya, K.; Onishi, T. *J. Chem. Soc. Chem. Commun.* **1986**, 356-357.

- (13) Sayama, K.; Arakawa, H.; Domen, K. *Catal. Today* **1996**, 28, 175-182.
- (14) Miseki, Y.; Kato, H.; Kudo, A. *Chem. Lett.* **2006**, 35, 1052-1053.
- (15) Ebina, Y.; Sakai, N.; Sasaki, T. *J. Phys. Chem. B* **2005**, 109, 17212-17216.
- (16) Kudo, A.; Nakagawa, S.; Kato, H. *Chem. Lett.* **1999**, 28, 1197-1198.
- (17) Miseki, Y.; Kato, H.; Kudo, A. *Chem. Lett.* **2005**, 34, 54-55.
- (18) Abe, R.; Higashi, M.; Zou, Z. G.; Sayama, K.; Arakawa, H. *J. Phys. Chem. B* **2004**, 108, 811-814.
- (19) Kudo, A.; Okutomi, H.; Kato, H. *Chem. Lett.* **2000**, 29, 1212-1213.
- (20) Kudo, A.; Kato, H. *Chem. Lett.* **1997**, 26, 867-868.
- (21) Kurihara, T.; Okutomi, H.; Miseki, Y.; Kato, H.; Kudo, A. *Chem. Lett.* **2006**, 35, 274-275.
- (22) Kato, H.; Kudo, A. *J. Phys. Chem. B* **2001**, 105, 4285-4292.
- (23) Kato, H.; Kobayashi, H.; Kudo, A. *J. Phys. Chem. B* **2002**, 106, 12441-12447.
- (24) Mitsui, C.; Nishiguchi, H.; Fukamachi, K.; Ishihara, T.; Takita, Y. *Chem. Lett.* **1999**, 28, 1327-1328.
- (25) Kudo, A.; Kato, H. *Chem. Phys. Lett.* **2000**, 331, 373-377.
- (26) Iwase, A.; Kato, H.; Okutomi, H.; Kudo, A. *Chem. Lett.* **2004**, 33, 1260-1261.
- (27) Ikeda, S.; Fubuki, M.; Takahara, Y. K.; Matsumura, M. *Appl. Catal. A* **2006**, 300, 186-190.
- (28) Ishihara, T.; Baik, N. S.; Ono, N.; Nishiguchi, H.; Takita, Y. *J. Photochem. Photobiol. A* **2004**, 167, 149-157.
- (29) Kato, H.; Kudo, A. *Chem. Lett.* **1999**, 28, 1207-1208.

- (30) Kato, H.; Kudo, A. *Chem. Phys. Lett.* **1998**, 295, 487-492.
- (31) Yoshioka, K.; Petrykin, V.; Kakihana, M.; Kato, H.; Kudo, A. *J. Catal.* **2005**, 232, 102-107.
- (32) Shimizu, K.; Tsuji, Y.; Hatamachi, T.; Toda, K.; Kodama, T.; Sato, M.; Kitayama, Y. *Phys. Chem. Chem. Phys.* **2004**, 6, 1064-1069.
- (33) Machida, M.; Yabunaka, J.; Kijima, T. *Chem. Mater.* **2000**, 12, 812-817.
- (34) Shimizu, K.; Itoh, S.; Hatamachi, T.; Kodama, T.; Sato, M.; Toda, K. *Chem. Mater.* **2005**, 17, 5161-5166.
- (35) Yao, W.; Ye, J. *Chem. Phys. Lett.* **2007**, 435, 96-99.
- (36) Mitsuyama, T.; Tsutsui, A.; Hara, T.; Ikeue, K.; Machida, M. *Bull. Chem. Soc. Jpn.* **2008**, 81, 401-406.
- (37) Otsuka, H.; Kim, K.; Kouzu, A.; Takimoto, I.; Fujimori, H.; Sakata, Y.; Imamura, H.; Matsumoto, T.; Toda, K. *Chem. Lett.* **2005**, 34, 822-823.
- (38) Li, Y.; Chen, G.; Zhou, C.; Li, Z. *Catal. Lett.* **2008**, 123, 80-83.
- (39) Kondo, J. N.; Uchida, M.; Nakajima, K.; Daling, L. Hara, M.; Domen, K. *Chem. Mater.* **2004**, 16, 4304-4310.
- (40) Machida, M.; Murakami, S.; Kijima, T. *J. Phys. Chem. B* **2001**, 105, 3289-3294.
- (41) Kato, H.; Asakura, K.; Kudo, A. *J. Am. Chem. Soc.* **2003**, 125, 3082-3089.
- (42) (a) Saito, N.; Kadowaki, H.; Kobayashi, H.; Ikarashi, K.; Nishiyama, H.; Inoue, Y. *Chem. Lett.* **2004**, 33, 1452-1453. (b) Kadowaki, H.; Saito, N.; Nishiyama, H.; Kobayashi, H.; Shimodaira, Y.; Inoue, Y. *J. Phys. Chem. C* **2007**, 111, 439-445.
- (43) Ikeda, S.; Itani, T.; Nango, K.; Matsumura, M. *Catal. Lett.* **2004**, 98, 229-233.
- (44) Kadowaki, H.; Saito, N.; Nishiyama, H.; Inoue, Y. *Chem. Lett.* **2007**, 36, 440-441.

- (45) Yuan, Y.; Zheng, J.; Zhang, X.; Li, Z.; Yu, T.; Ye, J.; Zou, Z. *Solid State Ionics* **2008**, *178*, 1711-1713.
- (46) Sato, J.; Kobayashi, H.; Inoue, Y. *J. Phys. Chem. B* **2003**, *107*, 7970-7975.
- (47) (a) Sato, J.; Kobayashi, H.; Saito, N.; Nishiyama, H.; Inoue, Y. *J. Photochem. Photobiol. A* **2003**, *158*, 139-144. (b) Sato, J.; Saito, N.; Nishiyama, H.; Inoue, Y. *J. Phys. Chem. B* **2003**, *107*, 7965-7969.
- (48) Arai, N.; Saito, N.; Nishiyama, H.; Shimodaira, Y.; Kobayashi, H.; Inoue, Y.; Sato, K. *J. Phys. Chem. C* **2008**, *112*, 5000-5005.
- (49) Sato, J.; Saito, N.; Nishiyama, H.; Inoue, Y. *Chem. Lett.* **2001**, 868-869.
- (50) Sato, J.; Kobayashi, H.; Ikarashi, K.; Saito, N.; Nishiyama, H.; Inoue, Y. *J. Phys. Chem. B* **2004**, *108*, 4369-4375.
- (51) Ikarashi, K.; Sato, J.; Kobayashi, H.; Saito, N.; Nishiyama, H.; Inoue, Y. *J. Phys. Chem. B* **2002**, *106*, 9048-9053.
- (52) Ikarashi, K.; Sato, J.; Kobayashi, H.; Saito, N.; Nishiyama, H.; Shimodaira, Y.; Inoue, Y. *J. Phys. Chem. B* **2005**, *109*, 22995-23000.
- (53) Yanagida, T.; Sakata, Y.; Imamura, H. *Chem. Lett.* **2004**, *33*, 726-727.
- (54) (a) Sato, J.; Saito, N.; Yamada, Y.; Maeda, K.; Takata, T.; Kondo, J. N.; Hara, M.; Kobayashi, H.; Domen, K.; Inoue, Y. *J. Am. Chem. Soc.* **2005**, *127*, 4150-4151. (b) Lee, Y.; Watanabe, T.; Takata, T.; Hara, M.; Yoshimura, M.; Domen, K. *J. Phys. Chem. B* **2006**, *110*, 17563-17569. (c) Maeda, K.; Saito, N.; Lu, D.; Inoue, Y.; Domen, K. *J. Phys. Chem. C* **2007**, *111*, 4749-4755. (d) Maeda, K.; Saito, N.; Inoue, Y.; Domen, K. *Chem. Mater.* **2007**, *19*, 4092-4097.
- (55) Maeda, K.; Teramura, K.; Saito, N.; Inoue, Y.; Domen, K. *Bull. Chem. Soc. Jpn.* **2007**, *80*, 1004-1010.
- (56) (a) Arai, N.; Saito, N.; Nishiyama, H.; Inoue, Y.; Domen, K.; Sato, K. *Chem. Lett.* **2006**, *35*, 796-797. (b) Arai, N.; Saito, N.; Nishiyama, H.; Domen, K.; Kobayashi, H.; Sato, K.; Inoue, Y. *Catal. Today* **2007**, *129*, 407-411.

- (57) Yan, H.; Yang, J.; Ma, G.; Wu, G.; Zong, X.; Lei, Z.; Shi, J.; Li, C. *J. Catal.* **2009**, *266*, 165-168.
- (58) Kobayakawa, K.; Teranishi, A.; Tsurumaki, T.; Sato, Y.; Fujishima, A. *Electrochim. Acta* **1992**, *37*, 465-467.
- (59) Kudo, A. *Int. J. Hydrogen Energy* **2006**, *31*, 197-202.
- (60) Chen, D.; Ye, J. *J. Phys. Chem. Solids* **2007**, *68*, 2317-2320.
- (61) Kudo, A.; Nagane, A.; Tsuji, I.; Kato, H. *Chem. Lett.* **2002**, *31*, 882-883.
- (62) Lei, Z.; You, W.; Liu, M.; Zhou, G.; Takata, T.; Hara, M.; Domen, K.; Li, C. *Chem. Commun.* **2003**, 2142-2143.
- (63) Zheng, N.; Bu, X.; Vu, H.; Feng, P. *Angew. Chem. Int. Ed.* **2005**, *44*, 5299-5303.
- (64) (a) Darwent, J. R.; Mills, A. *J. Chem. Soc., Faraday Trans. 2* **1982**, *78*, 359-367.  
(b) Erbs, W.; Desilvestro, J.; Borgarello, E.; Gratzel, M. *J. Phys. Chem.* **1984**, *88*, 4001-4006. (c) Miseki, Y.; Kusama, H.; Sugihara, H.; Sayama, K. *J. Phys. Chem. Lett.* **2010**, *1*, 1196-1200.
- (65) Tilley, S. D.; Cornuz, M.; Sivula, K.; Gratzel, M. *Angew. Chem. Int. Ed.* **2010**, *49*, 6405-6408.
- (66) Wang, X.; Maeda, K.; Thomas, A.; Takanabe, K.; Xin, G.; Carlsson, J. M.; Domen, K.; Antonietti, M. *Nature Mater.* **2009**, *8*, 76-80.
- (67) Zhang, Y.; Mori, T.; Ye, J.; Antonietti, M. *J. Am. Chem. Soc.* **2010**, *132*, 6294–6295.
- (68) Chen, X.; Shen, S.; Guo, L.; Mao, S. S. *Chem. Rev.* **2010**, *110*, 6503–6570.
- (69) Borgarello, E.; Kiwi, J.; Grātzel, M.; Pelizzetti, E.; Visca, M. *J. Am. Chem. Soc.* **1982**, *104*, 2996-3002.
- (70) (a) Luo, Z.; Gao, Q. *J. Photochem. Photobiol. A* **1992**, *63*, 367-375. (b) Tian, B.; Li, C.; Gu, F.; Jiang, H.; Hu, Y.; Zhang, J. *Chem. Eng. J.* **2009**, *151*, 220-227. (c) Devi, L. G.; Kumar, S. G.; Murthy, B. N.; Kottam, N. *Catal. Commun.* **2009**, *10*,

- 794-795. (d) Takaoka, G. H.; Nose, T.; Kawashita, M. *Vacuum* **2008**, *83*, 679-683. (e) Fan, X.; Chen, X.; Zhu, S.; Li, Z.; Yu, T.; Ye, J.; Zou, Z. *J. Mol. Catal. A: Chem.* **2008**, *284*, 155-160. (f) Kim, D. H.; Choi, D. K.; Kim, S. J.; Lee, K. S. *Catal. Commun.* **2008**, *9*, 654-655.
- (71) (a) Anpo, M.; Kishiguchi, S.; Ichihashi, Y.; Takeuchi, M.; Yamashita, H.; Ikeue, K.; Morin, B.; Davidson, A.; Che, M. *Res. Chem. Intermed.* **2001**, *27*, 459-467. (b) Anpo, M. *Pure Appl. Chem.* **2000**, *72*, 1787-1792. (c) Anpo, M. *Pure Appl. Chem.* **2000**, *72*, 1265-1270. (d) Anpo, M.; Takeuchi, M. *Int. J. Photoenergy* **2001**, *3*, 89-94. (e) Anpo, M.; Takeuchi, M. *J. Catal.* **2003**, *216*, 505-516. (f) Takeuchi, M.; Yamashita, H.; Matsuoka, M.; Anpo, M.; Hirao, T.; Itoh, N.; Iwamoto, N. *Catal. Lett.* **2000**, *67*, 135-137.
- (72) (a) Kim, S.; Hwang, S. J.; Choi, W. *J. Phys. Chem. B* **2005**, *109*, 24260-24267. (b) Rengaraj, S.; Li, X. *Z. J. Mol. Catal. A: Chem.* **2006**, *243*, 60-67.
- (73) (a) Niishiro, R.; Konta, R.; Kato, H.; Chun, W. J.; Asakura, K.; Kudo, A. *J. Phys. Chem. C* **2007**, *111*, 17420-17426. (b) Niishiro, R.; Kato, H.; Kudo, A. *Phys. Chem. Chem. Phys.* **2005**, *7*, 2241-2245. (c) Ikeda, T.; Nomoto, T.; Eda, K.; Mizutani, Y.; Kato, H.; Kudo, A.; Onishi, H. *J. Phys. Chem. C* **2008**, *112*, 1167-1173. (d) Matsumoto, Y.; Unal, U.; Tanaka, N.; Kudo, A.; Kato, H. *J. Solid State Chem.* **2004**, *177*, 4205-4212.
- (74) (a) Wang, D.; Ye, J.; Kako, T.; Kimura, T. *J. Phys. Chem. B* **2006**, *110*, 15824-15830. (b) Konta, R.; Ishii, T.; Kato, H.; Kudo, A. *J. Phys. Chem. B* **2004**, *108*, 8992-8995. (c) Sayama, K.; Mukasa, K.; Abe, R.; Abe, Y.; Arakawa, H. *Chem. Commun.* **2001**, *23*, 2416-2417.
- (75) (a) Nishimoto, S.; Matsuda, M.; Miyake, M. *Chem. Lett.* **2006**, *35*, 308-309. (b) Zhang, H.; Chen, G.; Li, Y.; Teng, Y. *Int. J. Hydrogen Energy* **2010**, *35*, 2713-2716.
- (76) (a) Hwang, D. W.; Kim, H. G.; Jang, J. S.; Bae, S. W.; Ji, S. M.; Lee, J. S. *Catal. Today* **2004**, *93-95*, 845-850. (b) Hwang, D. W.; Kim, H. G.; Lee, J. S.; Li, W.; Oh, S. H. *J. Phys. Chem. B* **2005**, *109*, 2093-2102.
- (77) (a) Wang, B.; Li, C.; Hirabayashi, D.; Suzuki, K. *Int. J. Hydrogen Energy* **2010**, *35*, 3306-3312. (b) Yang, Y.; Chen, Q.; Yin, Z.; Li, J. *J. Alloys Compd.* **2008**, *225*, 8419-8422.

- (78) Shah, P.; Bhange, D. S.; Deshpande, A. S.; Kulkarni, M. S.; Gupta, N. M. *Mater. Chem. Phys.* **2009**, *117*, 399-407.
- (79) (a) Zou, Z.; Ye, J.; Sayama, K.; Arakawa, H. *Nature* **2001**, *414*, 625-627. (b) Zou, Z.; Ye, J.; Sayama, K.; Arakawa, H. *J. Photochem. Photobiol. A* **2002**, *148*, 65-69. (c) Zou, Z.; Ye, J.; Arakawa, H. *Catal. Lett.* **2001**, *75*, 209-214. (d) Zou, Z.; Ye, J.; Arakawa, H. *J. Phys. Chem. B* **2002**, *106*, 13098-13101.
- (80) Lin, H. Y.; Lee, T. H.; Sie, C. Y. *Int. J. Hydrogen Energy* **2008**, *33*, 4055-4063.
- (81) Zhang, H.; Chen, G.; Li, X.; Wang, Q. *Int. J. Hydrogen Energy* **2009**, *34*, 3631-3638.
- (82) Iwase, A.; Saito, K.; Kudo, A. *Bull. Chem. Soc. Jpn.* **2009**, *82*, 514-518.
- (83) (a) Asahi, R.; Morikawa, T.; Ohwaki, T.; Aoki, K.; Taga, Y. *Science* **2001**, *293*, 269-271. (b) Chen, X.; Burda, C. *J. Am. Chem. Soc.* **2008**, *130*, 5018-5019.
- (84) (a) Lindgren, T.; Mwabora, J. M.; Avendano, E.; Jonsson, J.; Hoel, A.; Granqvist, C. G.; Lindquist, S. E. *J. Phys. Chem. B* **2003**, *107*, 5709-5716. (b) Chen, X.; Burda, C. *J. Phys. Chem. B* **2004**, *108*, 15446-15449. (c) Gole, J. L.; Stout, J. D.; Burda, C.; Lou, Y.; Chen, X. *J. Phys. Chem. B* **2004**, *108*, 1230-1240. (d) Zaleska, A.; Grabowska, E.; Sobczak, J. W.; Gazda, M.; Hupka, J. *Appl. Catal. B* **2009**, *89*, 469-475. (e) Ohno, T.; Tsubota, T.; Nakamura, Y.; Sayama, K. *Appl. Catal. A* **2005**, *288*, 74-79. (f) Paven-Thivet, C. L.; Ishikawa, A.; Ziani, A.; Gendre, L. L.; Yoshida, M.; Kubota, J.; Tessier, F.; Domen, K. *J. Phys. Chem. C* **2009**, *113*, 6156-6162.
- (85) (a) Ito, S.; Thampi, K. R.; Comte, P.; Liska, P.; Gratzel, M. *Chem. Commun.* **2005**, *2*, 268-269. (b) Lu, D.; Hitoki, G.; Katou, E.; Kondo, J. N.; Hara, M.; Domen, K. *Chem. Mater.* **2004**, *16*, 1063-1064. (c) Hara, M.; Hitoki, G.; Takata, T.; Kondo, J. N.; Kobayashi, H.; Domen, K. *Catal. Today* **2003**, *78*, 555-560. (d) Yashima, M.; Lee, Y.; Domen, K. *Chem. Mater.* **2007**, *19*, 588-593. (e) Liu, M.; You, W.; Lei, Z.; Zhou, G.; Yang, J.; Wu, G.; Ma, G.; Luan, G.; Takata, T.; Hara, M.; Domen, K.; Li, C. *Chem. Commun.* **2004**, *19*, 2192-2193. (f) Higashi, M.; Abe, R.; Teramura, K.; Takata, T.; Ohtani, B.; Domen, K. *Chem. Phys. Lett.* **2008**, *452*, 120-123.
- (86) (a) Mishima, T.; Matsuda, M.; Miyake, M. *Appl. Catal. A* **2007**, *324*, 77-85. (b)

- Qiu, X.; Zhao, Y.; Burda, C. *Adv. Mater.* **2007**, *19*, 3995-3999. (c) Kanade, K. G.; Baeg, J. O.; Kale, B. B.; Lee, S. M.; Moon, S. J.; Kong, K. *Int. J. Hydrogen Energy* **2007**, *32*, 4678-4684.
- (87) (a) Ji, S. M.; Borse, P. H.; Kim, H. G.; Hwang, D. W.; Jang, J. S.; Bae, S. W.; Lee, J. S. *Phys. Chem. Chem. Phys.* **2005**, *7*, 1315-1321. (b) Li, X.; Kikugawa, N.; Ye, J. *Adv. Mater.* **2008**, *20*, 3816-3819. (c) Shi, H.; Li, X.; Iwai, H.; Zou, Z.; Ye, J. *J. Phys. Chem. Solids* **2009**, *70*, 931-935. (d) Matsumoto, Y.; Koinuma, M.; Iwanaga, Y.; Sato, T.; Iida, S. *J. Am. Chem. Soc.* **2009**, *131*, 6644-6649.
- (88) Gai, Y.; Li, J.; Li, S. S.; Xia, J. B.; Wei, S. H. *Phys. Rev. Lett.* **2009**, *102*, 036402.
- (89) (a) Maeda, K.; Takata, T.; Hara, M.; Saito, N.; Inoue, Y.; Kobayashi, H.; Domen, K. *J. Am. Chem. Soc.* **2005**, *127*, 8286-8287. (b) Maeda, K.; Teramura, K.; Lu, D.; Takata, T.; Saito, N.; Inoue, Y.; Domen, K. *Nature* **2006**, *440*, 295.
- (90) Maeda, K.; Teramura, K.; Takata, T.; Hara, M.; Saito, N.; Toda, K.; Inoue, Y.; Kobayashi, H.; Domen, K. *J. Phys. Chem. B* **2005**, *109*, 20504-20510.
- (91) Maeda, K.; Domen, K. *J. Phys. Chem. C* **2007**, *111*, 7851-7861.
- (92) (a) Lee, Y.; Terashima, H.; Shimodaira, Y.; Teramura, K.; Hara, M.; Kobayashi, H.; Domen, K.; Yashima, M. *J. Phys. Chem. C* **2007**, *111*, 1042-1048. (b) Lee, Y.; Teramura, K.; Hara, M.; Domen, K. *Chem. Mater.* **2007**, *19*, 2120-2127. (c) Wang, X.; Maeda, K.; Lee, Y.; Domen, K. *Chem. Phys. Lett.* **2008**, *457*, 134-136. (d) Tessier, F.; Maillard, P.; Lee, Y.; Bleugat, C.; Domen, K. *J. Phys. Chem. C* **2009**, *113*, 8526-8531.
- (93) Kamata, K.; Maeda, K.; Lu, D.; Kako, Y.; Domen, K. *Chem. Phys. Lett.* **2009**, *470*, 90-94.
- (94) Zhang, K.; Jing, D.; Xing, C.; Guo, L. J. *Int. J. Hydrogen Energy* **2007**, *32*, 4685-4691.
- (95) (a) Tsuji, I.; Kato, H.; Kudo, A. *Angew. Chem., Int. Ed.* **2005**, *44*, 3565-3568. (b) Tsuji, I.; Kato, H.; Kobayashi, H.; Kudo, A. *Chem. Mater.* **2006**, *18*, 1969-1975.
- (96) Tsuji, I.; Shimodaira, Y.; Kato, H.; Kobayashi, H.; Kudo, A. *Chem. Mater.* **2010**, *22*, 1042-1049.

- (97) Li, Y.; Ma, G.; Peng, S.; Lu, G.; Li, S. *Appl. Catal. A* **2009**, *363*, 180-187.
- (98) (a) Zou, Z.; Ye, J.; Sayama, K.; Arakawa, H. *Chem. Phys. Lett.* **2001**, *343*, 303-308. (b) Zou, Z.; Ye, J.; Arakawa, H. *Solid State Commun.* **2001**, *119*, 471-475.
- (99) (a) Yao, W.; Ye, J. *J. Phys. Chem. B* **2006**, *110*, 11188-11195. (b) Yao, W.; Ye, J. *Chem. Phys. Lett.* **2008**, *450*, 370-374.
- (100) Liu, H.; Yuan, J.; Shangguan, W.; Teraoka, Y. *J. Phys. Chem. C* **2008**, *112*, 8521-8523.
- (101) Wang, Q.; Liu, H.; Jiang, L.; Yuan, J.; Shangguan, W. *Catal. Lett.* **2009**, *131*, 160-163.
- (102) (a) Kudo, A.; Ueda, K.; Kato, H.; Mikami, I. *Catal. Lett.* **1998**, *53*, 229-230. (b) Kudo, A.; Omori, K.; Kato, H. *J. Am. Chem. Soc.* **1999**, *121*, 11459-11467. (c) Yu, J.; Zhang, Y.; Kudo, A. *J. Solid State Chem.* **2009**, *182*, 223-228. (d) Ke, D.; Peng, T.; Ma, L.; Cai, P.; Dai, K. *Inorg. Chem.* **2009**, *48*, 4685-4691. (e) Ke, D.; Peng, T.; Ma, L.; Cai, P.; Jiang, P. *Appl. Catal. A* **2008**, *350*, 111-117. (f) Li, M. T.; Zhao, L.; Guo, L. *J. Int. J. Hydrogen Energy* **2010**, *35*, 7127-7133.
- (103) Kudo, A.; Miseki, Y. *Chem. Soc. Rev.* **2009**, *38*, 253–278.
- (104) Ye, J.; Zou, Z.; Oshikiri, M.; Matsushita, A.; Shimoda, M.; Imai, M.; Shishido, T. *Chem. Phys. Lett.* **2002**, *356*, 221-226.
- (105) Wang, D.; Tang, J.; Zou, Z.; Ye, J. *Chem. Mater.* **2005**, *17*, 5177-5182.
- (106) Yao, W.; Ye, J. *Catal. Today* **2006**, *116*, 18-21.
- (107) Luan, J.; Cai, H.; Zheng, S.; Hao, X.; Luan, G.; Wu, X.; Zou, Z. *Mater. Chem. Phys.* **2007**, *104*, 119-124.
- (108) Luan, J.; Zheng, Z.; Cai, H.; Wu, X.; Luan, G.; Zou, Z. *Mater. Res. Bull.* **2008**, *43*, 3332-3344.
- (109) (a) Liu, H.; Nakamura, R.; Nakato, Y. *ChemPhysChem* **2005**, *6*, 2499-2502. (b) Liu, H.; Nakamura, R.; Nakato, Y. *Electrochim. Solid-State Lett.* **2006**, *9*,

G187-G190.

- (110) Wang, D.; Zou, Z.; Ye, J. *Catal. Today* **2004**, *93-95*, 891-894.
- (111) Yin, J.; Zou, Z.; Ye, J. *Chem. Phys. Lett.* **2003**, *378*, 24-28.
- (112) Wang, D.; Zou, Z.; Ye, J. *Chem. Phys. Lett.* **2003**, *373*, 191-196.
- (113) Ouyang, S.; Li, Z.; Ouyang, Z.; Yu, T.; Ye, J.; Zou, Z. *J. Phys. Chem. C* **2008**, *112*, 3134-3141.
- (114) Silva, C. G.; Bouizi, Y.; Fornes, V.; Garcia, H. *J. Am. Chem. Soc.* **2009**, *131*, 13833-13839.
- (115) Ye, J.; Zou, Z.; Matsushita, A. *Int. J. Hydrogen Energy* **2003**, *28*, 651-655.
- (116) (a) Yin, J.; Zou, Z.; Ye, J. *J. Phys. Chem. B* **2003**, *107*, 4936-4941. (b) Yin, J.; Zou, Z.; Ye, J. *J. Mater. Sci.* **2006**, *41*, 1131-1135.
- (117) Wang, Y. X.; Wang, Y. Q.; Gao, Y. T. *React. Kinet. Mech. Catal.* **2010**, *99*, 485-491.
- (118) Kato, H.; Kobayashi, H.; Kudo, A. *J. Phys. Chem. B* **2002**, *106*, 12441-12447.
- (119) Tang, J.; Zou, Z.; Ye, J. *J. Phys. Chem. B* **2003**, *107*, 14265-14269.
- (120) Maruyama, Y.; Irie, H.; Hashimoto, K. *J. Phys. Chem. B* **2006**, *110*, 23274-23278.
- (121) Hosogi, Y.; Kato, H.; Kudo, A. *J. Mater. Chem.* **2008**, *18*, 647-653.
- (122) Li, X.; Ouyang, S.; Kikugawa, N.; Ye, J. *Appl. Catal. A* **2008**, *334*, 51-58.
- (123) (a) Tang, J.; Zou, Z.; Katagiri, M.; Kako, T.; Ye, J. *Catal. Today* **2004**, *93-95*, 885-889. (b) Tang, J.; Zou, Z.; Ye, J. *Chem. Mater.* **2004**, *16*, 1644-1649.
- (124) (a) Zou, Z.; Ye, J.; Arakawa, H. *Mater. Res. Bull.* **2001**, *36*, 1185-1193. (b) Zhang, L.; Djerdj, I.; Cao, M.; Antonietti, M.; Niederberger, M. *Adv. Mater.* **2007**, *19*, 2083-2086. (c) Chiou, Y. C.; Kumar, U.; Wu, J. C. S. *Appl. Catal. A* **2009**, *357*, 73-78.

- (125) Zhou, J.; Zou, Z.; Ray, A. K.; Zhao, X. S. *Ind. Eng. Chem. Res.* **2007**, *46*, 745-749.
- (126) (a) Tang, J.; Zou, Z.; Ye, J. *Angew. Chem.* **2004**, *116*, 4563-4566. (b) Solarska, R.; Heel, A.; Ropka, J.; Braun, A.; Holzer, L.; Ye, J.; Graule, T. *Appl. Catal. A* **2010**, *382*, 190-196.
- (127) Fu, H.; Zhang, L.; Yao, W.; Zhu, Y. *Appl. Catal. B* **2006**, *66*, 100-110.
- (128) Shimodaira, Y.; Kato, H.; Kobayashi, H.; Kudo, A. *J. Phys. Chem. B* **2006**, *110*, 17790-17797.
- (129) Lin, X. P.; Huang, F. Q.; Wang, W. D.; Zhang, K. L. *Appl. Catal. A* **2006**, *307*, 257-262.
- (130) (a) Zou, Z.; Ye, J.; Arakawa, H. *Mater. Sci. Eng.* **2001**, *B79*, 83-84. (b) Zou, Z.; Ye, J.; Arakawa, H. *Int. J. Hydrogen Energy* **2003**, *28*, 663-669.
- (131) Kako, T.; Zou, Z.; Katagiri, M.; Ye, J. *Chem. Mater.* **2007**, *19*, 198-202.
- (132) (a) Li, X.; Kako, T.; Ye, J. *Appl. Catal. A* **2007**, *326*, 1-7. (b) Li, X.; Ye, J. *J. Phys. Chem. C* **2007**, *111*, 13109-13116.
- (133) (a) Kim, H. G.; Becker, O. S.; Jang, J. S.; Ji, S. M.; Borse, P. H.; Lee, J. S. *J. Solid State Chem.* **2006**, *179*, 1214-1218. (b) Kim, H. G.; Hwang, D. W.; Lee, J. S. *J. Am. Chem. Soc.* **2004**, *126*, 8912-8913.
- (134) Hosogi, Y.; Kato, H.; Kudo, A. *Chem. Lett.* **2006**, *35*, 578-579.
- (135) Hosogi, Y.; Shimodaira, Y.; Kato, H.; Kobayashi, H.; Kudo, A. *Chem. Mater.* **2008**, *20*, 1299-1307.
- (136) Cho, I. S.; Kwak, C. H.; Kim, D. W.; Lee, S.; Hong, K. S. *J. Phys. Chem. C* **2009**, *113*, 10647-10653.
- (137) Zou, Z.; Ye, J.; Arakawa, H. *J. Phys. Chem. B* **2002**, *106*, 517-520.
- (138) Hwang, D. W.; Lee, J. S.; Li, W.; Oh, S. H. *J. Phys. Chem. B* **2003**, *107*,

4963-4970.

- (139) (a) Uno, M.; Kosuga, A.; Okui, M.; Horisaka, K.; Yamanaka, S. *J. Alloys Compd.* **2005**, *400*, 270-275. (b) Uno, M.; Kosuga, A.; Okui, M.; Horisaka, K.; Muta, H.; Kuroasaki, K.; Yamanaka, S. *J. Alloys Compd.* **2006**, *420*, 291-297.
- (140) Tian, M.; Shangguan, W.; Yuan, J.; Jiang, L.; Chen, M.; Shi, J.; Ouyang, Z.; Wang, S. *Appl. Catal. A* **2006**, *309*, 76-84.
- (141) (a) Tang, X.; Ye, H.; Liu, H.; Ma, C.; Zhao, Z. *J. Solid State Chem.* **2010**, *183*, 192-197. (b) Tang, X. D.; Ye, H. Q.; Liu, H.; Ma, C. X.; Zhao, Z. *Chem. Phys. Lett.* **2009**, *484*, 48-53.
- (142) Frame, F. A.; Townsend, T. K.; Chamousis, R. L.; Sabio, E. M.; Dittrich, T.; Browning, N. D.; Osterloh, F. E. *J. Am. Chem. Soc.* **2011**, *133*, 7264-7267.
- (143) Kumagai, N.; Ni, L.; Irie, H. *Chem. Commun.* **2011**, *47*, 1884-1886.
- (144) Chen, X.; Liu, L.; Yu, P. Y.; Mao, S. S. *Science*, **2011**, *331*, 746-750.
- (145) Tao, J.; Luttrell, T.; Batzill, M. *Nature Chem.* **2011**, *3*, 296-300.

## **Chapter 3**

# **Visible-light-responsive Copper (II) Borate Photocatalysts with Intrinsic Midgap States for Water Splitting**

### **3.1 Introduction**

Semiconductor-based photocatalysts can convert solar energy into hydrogen by splitting water or decompose harmful environmental pollutants under ultraviolet or visible light irradiation.<sup>1</sup> Visible-light-responsive metal oxides photocatalysts are particularly promising for practical applications due to their photostabilities.<sup>2</sup> However most metal oxides have band gaps in the UV range. One of the most effective strategies for achieving visible light response in photocatalytic water splitting is by doping the materials with transition metal ions or non-metal elements.<sup>1(a)-1(e)</sup> Doping creates either an electron-donor level above the original valence band (VB) or an electron-acceptor level below the original conduction band (CB), making the photocatalyst active under visible light.<sup>3</sup> Unfortunately, dopants may also create localized defect sites that hinder charge migration through the semiconductor and inhibit photocatalysis. For this reason, undoped visible-light photocatalysts are preferred. In principle, undoped semiconductors which intrinsically exhibit an electron-donor or acceptor levels between the VB and CB should be ideal candidates for visible-light photocatalysis. One such material, an undoped photocatalyst  $\text{CaCu}_3\text{Ti}_4\text{O}_{12}$  that degrades pollutant 4-chlorophenol (4-CP), was reported

recently.<sup>4</sup> Density functional theory (DFT) suggests that a localized empty state between the VB and CB acted as an electron-acceptor level. However, few such photocatalytic materials for water splitting are known.

Here, we report two undoped borate photocatalysts, namely CuB<sub>2</sub>O<sub>4</sub> and Cu<sub>3</sub>B<sub>2</sub>O<sub>6</sub>, that can produce either H<sub>2</sub> or O<sub>2</sub> under visible light irradiation in the presence of sacrificial agents. DFT predicts that these copper borates exhibit intrinsic midgap states that derive from the Cu 3d orbitals and whose properties depend strongly on the crystal structures and Cu<sup>2+</sup> coordination environments. Such intrinsic midgaps states are rare, and these materials provide two new examples of this behavior. More importantly, both midgap states serve as an electron acceptor level, but they function very differently in the two copper borates. For CuB<sub>2</sub>O<sub>4</sub>, the midgap states facilitate the visible light absorption for photocatalytic water splitting, while for Cu<sub>3</sub>B<sub>2</sub>O<sub>6</sub>, the midgap states trap electrons and reduce the photocatalytic activity.

### 3.2 Experimental Section

#### 3.2.1 Method of Synthesis

All chemicals, including boric acid (Acros, 99+%), boron oxide (City Chemical, 99.9%), copper (II) nitrate trihydrate (Acros, for analysis), copper (II) oxide (Sigma-Aldrich, 99.99%), iron (III) oxide (Alfa Aesar, 99.5%), sodium nitrate (Alfa Aesar, 99%) were used as received without any further purification.

A typical synthetic procedure of CuB<sub>2</sub>O<sub>4</sub> can refer to a previous report.<sup>5</sup> First, H<sub>3</sub>BO<sub>3</sub>, Cu(NO<sub>3</sub>)<sub>2</sub>·3H<sub>2</sub>O, and NaNO<sub>3</sub> at a molar ratio of 1:10:0.02 were dissolved in distilled water. The solution was slowly evaporated to dryness on a hot plate with constant stirring. The dry mixture was heated at 500 °C for 5 h. The resultant mixture was ground thoroughly and heated at 800 °C for 12 h. The product was washed with a large amount of warm distilled water to remove excess B<sub>2</sub>O<sub>3</sub> and then dry at 70 °C overnight. The final product was ground before characterization and property measurements.

A typical synthetic procedure of Cu<sub>3</sub>B<sub>2</sub>O<sub>6</sub> can refer to a previous report<sup>6</sup> with minor changes. A nearly stoichiometric mixture of CuO and B<sub>2</sub>O<sub>3</sub> (3% excess B<sub>2</sub>O<sub>3</sub>) was heated in air at 900 °C for 36 h, with two intermediate grindings. The product was washed with a large amount of warm distilled water and then dried at 70 °C overnight. The final product was ground before characterization and property measurements.

### 3.2.2 Characterizations

Powder X-ray diffraction data were collected using a Bruker D8-Advance powder diffractometer operating at 40kV, 40mA for Cu K $\alpha$  radiation ( $\lambda=1.54\text{\AA}$ ). The pure Al<sub>2</sub>O<sub>3</sub> was used as the internal standard to allow for accurate measurement of the peak positions (i.e. 2 $\theta$  values) which might be shifted due to various experimental or instrumental factors such as the height of the sample surface. The UV-visible absorption spectra were recorded on a Shimadzu UV-3101PC UV-Vis-NIR spectrophotometer

operating in the diffuse mode with application of Kubelka-Munk equation. SEM pictures were recorded on a Philips XL30 scanning electron microscope. A thin layer of Au/Pd was sprayed onto the sample before measurement. The ESR spectra were obtained on a JES-FA 200 ESR spectrometer at room temperature. The X-ray photoelectron spectroscopy (XPS) characterization was carried out by using a Kratos AXIS ULTRADLD XPS system equipped with an Al K monochromated X-ray source and a 165-mm electron energy hemispherical analyzer to examine the surface properties and composition of the sample. All the binding energies were calibrated by using the contaminant carbon (C 1s) 284.6 eV as a reference. The specific surface area was calculated using the BET (Brunauer-Emmett-Teller) method from the nitrogen adsorption data in the relative range ( $P/P_0$ ) of 0.04-0.20

### 3.2.3 Photocatalytic Experiments

Photocatalytic H<sub>2</sub> and O<sub>2</sub> production experiments were conducted in a sealed circulation system. For H<sub>2</sub> evolution, 1 wt% Pt was loaded as cocatalysts by UV irradiation of PtCl<sub>4</sub> aqueous solution. In a typical run, 0.100 g of sample was suspended in 120 mL 25% methanol aqueous solution (containing 0.0017 g PtCl<sub>4</sub>) under magnetic stirring. Then a 300 W Xe lamp was applied to this mixture for 30 minutes, in that case, Pt nanoparticles would be loaded to the surface of CuB<sub>2</sub>O<sub>4</sub> as cocatalysts. After degassing the system for about half an hour, this 300 W Xe lamp with a 400 nm cut-on filter

(Newport Corp.) was applied to execute the photocatalytic reaction. For O<sub>2</sub> evolution, 1 wt% RuO<sub>2</sub> was loaded by impregnation from a carbonyl complex, Ru<sub>3</sub>(CO)<sub>12</sub> (Aldrich, 99.0%), in acetone solution according to the method reported previously.<sup>7</sup> In a typical run, 0.100 g RuO<sub>2</sub>-photocatalysts was suspended in 120 mL 0.05 M AgNO<sub>3</sub> aqueous solution containing 0.2 g La<sub>2</sub>O<sub>3</sub> as a base buffer to maintain the pH at ~8.08. After degassing the system for about half an hour, the 300 W Xe lamp with a 400 nm cut-on filter was applied to execute the photocatalytic reaction. The products of H<sub>2</sub> and O<sub>2</sub> were analyzed by gas chromatography (Shimadzu GC-8A) equipped with a thermal conductivity detector (TCD). All the photocatalysis experiments were repeated for three times at least.

To confirm the H<sub>2</sub> is coming from the photocatalytic reaction, the amount of H<sub>2</sub> we actually collected must exceed the amount of photocatalysts we used in the experiment (Turnover number > 1). To facilitate the measurements, H<sub>2</sub> was collected by illuminating the reaction under UV irradiation.<sup>8</sup> For CuB<sub>2</sub>O<sub>4</sub>, we collected 702.4 μmol of H<sub>2</sub> under UV irradiation (0.13 W/cm<sup>2</sup>) for 116 hours, which exceeds the amount of CuB<sub>2</sub>O<sub>4</sub> (0.1 g, 670.4 μmol) used in the experiment. During 116 hours irradiation under UV light, H<sub>2</sub> was steadily produced, which actually further verifies the photostability of the compound. Since Cu<sub>3</sub>B<sub>2</sub>O<sub>6</sub> appears much slower H<sub>2</sub> evolution rate than CuB<sub>2</sub>O<sub>4</sub>, in order to shorten the measurement period, we increased the light intensity to 1.66 W/cm<sup>2</sup> when performing its turnover number measurement. After 52 hours irradiation, we collected 3781.4 μmol

of H<sub>2</sub>, which exceeds the amount of Cu<sub>3</sub>B<sub>2</sub>O<sub>6</sub> (0.1 g, 324.39 µmol) used in the experiment. H<sub>2</sub> was steadily produced during the measurement which also further indicates the photostability of the compound.

The apparent quantum yield (AQY) was calculated based on the following equations: AQY of H<sub>2</sub> evolution = 100% × [(number of evolved H<sub>2</sub> molecules) × 2] / (number of incident photons); AQY of O<sub>2</sub> evolution = 100% × [(number of evolved O<sub>2</sub> molecules) × 4] / (number of incident photons). A 420 nm bandpass filter (Newport Corp.) was applied. The number of the incident photons was determined using a radiant power energy meter (Newport Corp., Model 70260 with a Thermopile Detector).

To further confirm the photocatalytic reactions, control experiments were conducted as follows. First, set up a H<sub>2</sub> evolution trial according to the above experimental conditions for H<sub>2</sub> evolution measurement and wrap the reactor with aluminum foils thoroughly. Sample the system every two hours, re-vacuum the system and sample it again in a two hours interval. Second, set up an O<sub>2</sub> evolution trial according to the above experimental conditions for O<sub>2</sub> evolution measurement and wrap the reactor with aluminum foils thoroughly. Sample the system in the same interval as it is used for O<sub>2</sub> evolution experiment above. In control experiments, only trace amount of H<sub>2</sub> or O<sub>2</sub> were observed, indicating the H<sub>2</sub> and O<sub>2</sub> obtained under visible light irradiation were not from the mechano-catalytic water splitting.

### 3.3 Density of States (DOS) Calculations

The DOS calculations were performed using the plane-wave-based DFT code, VASP,<sup>9</sup> via the projector-augmented wave method to describe core electrons.<sup>10</sup> The unit cells were sampled with an 8 x 8 x 16 k-point for CuB<sub>2</sub>O<sub>4</sub> and an 18 x 2 x 2 k-point for Cu<sub>3</sub>B<sub>2</sub>O<sub>6</sub>. Wave functions were expanded by the plane waves up to a cutoff energy of 400 eV. We performed the calculations using the LSDA functional of Ceperley and Alder, parameterized by Perdew and Zunger, and the LSDA+U method implemented by Dudarev and co-workers.<sup>11</sup> We chose the parameters of U(Cu)=7.5 eV, J(Cu)=0.98 eV for CuB<sub>2</sub>O<sub>4</sub> and U(Cu)=6.0 eV, J(Cu)=0.98 eV for Cu<sub>3</sub>B<sub>2</sub>O<sub>6</sub> respectively. The first set has been used on similar copper compounds previously and the predicted population maximum of the midgap state in CuB<sub>2</sub>O<sub>4</sub> agrees well with the experimental d-d transition peak maximum. The Cu<sub>3</sub>B<sub>2</sub>O<sub>6</sub> parameters were chosen to shift the midgap state population maximum to the energy corresponding to the experimental d-d transition peak maximum in that material as well.

Optimized crystal geometry compared with experimental results  
(in parentheses)

	CuB <sub>2</sub> O <sub>4</sub>	Cu <sub>3</sub> B <sub>2</sub> O <sub>6</sub>
a (Å)	11.499(11.480)	3.30397(3.35300)
b (Å)	11.499 (11.480)	19.7983(19.6650)
c (Å)	5.6049(5.6200)	19.7672(19.6270)
α (degree)	90.000 (90.000)	88.9970(88.7700)
β (degree)	90.000 (90.000)	69.6042(69.7100)
γ (degree)	90.000 (90.000)	69.3382(69.2400)
V	741.158 (741.178)	1125.44(1127.41)
density	4.01031(4.01020)	4.54812(4.54019)

### 3.4 Results and Discussion

#### 3.4.1 Instrumental Characterizations

Figure 3.1 depicts the crystal structures of two copper borates. The powder XRD of CuB<sub>2</sub>O<sub>4</sub> agrees well with its standard XRD pattern as shown in Figure 3.2. The deep blue tetragonal CuB<sub>2</sub>O<sub>4</sub> crystals consist of Cu<sup>2+</sup> ions bonding with oxygen ions to form a perfect square or a distorted octahedron.<sup>12</sup>

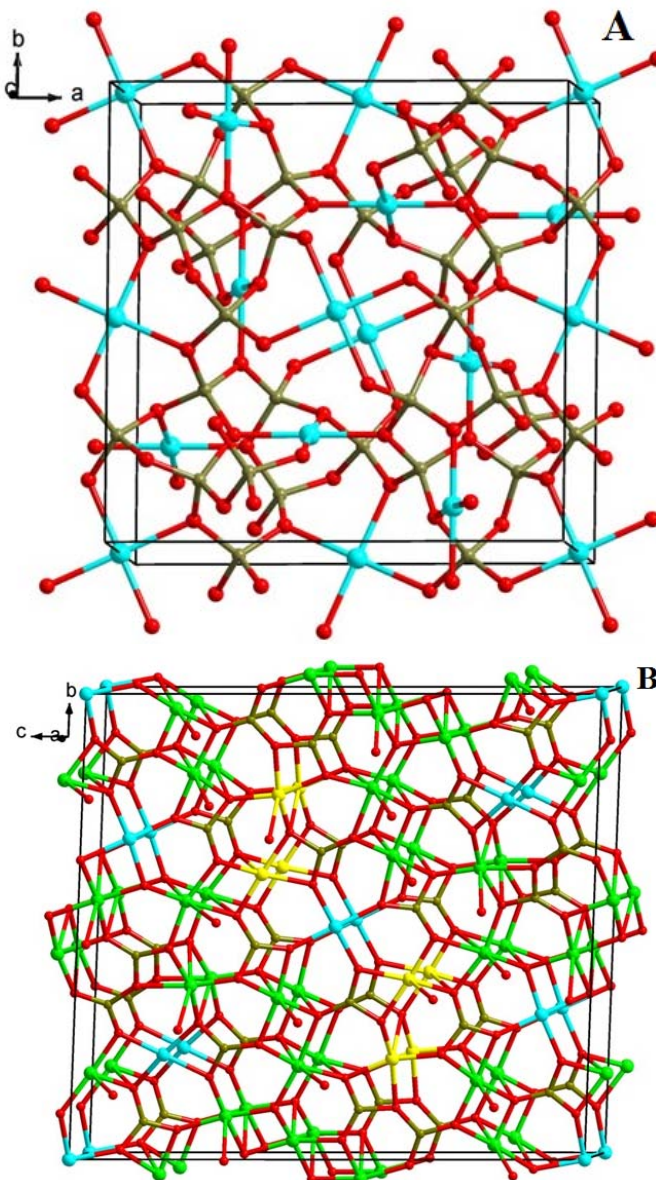


**Figure 3.1** Unit cell portions of the crystal structures of  $\text{CuB}_2\text{O}_4$  (A) and  $\text{Cu}_3\text{B}_2\text{O}_6$  (B). The color code is as follows: oxygen (red); boron (dark yellow); copper in square (cyan), pyramidal (yellow) and octahedral (green) geometry.

In Figure 3.2, prepared  $\text{Cu}_3\text{B}_2\text{O}_6$  contains small amount of unreacted  $\text{CuO}$  which is inactive for photocatalytic water reduction.<sup>13</sup> The dark green  $\text{Cu}_3\text{B}_2\text{O}_6$  crystals exhibit a triclinic layered structure. In each layer of  $\text{Cu}_3\text{B}_2\text{O}_6$ , different  $\text{Cu}^{2+}$  ions are coordinated

in octahedral, square, or pyramidal environments of oxygen ions.<sup>14</sup>

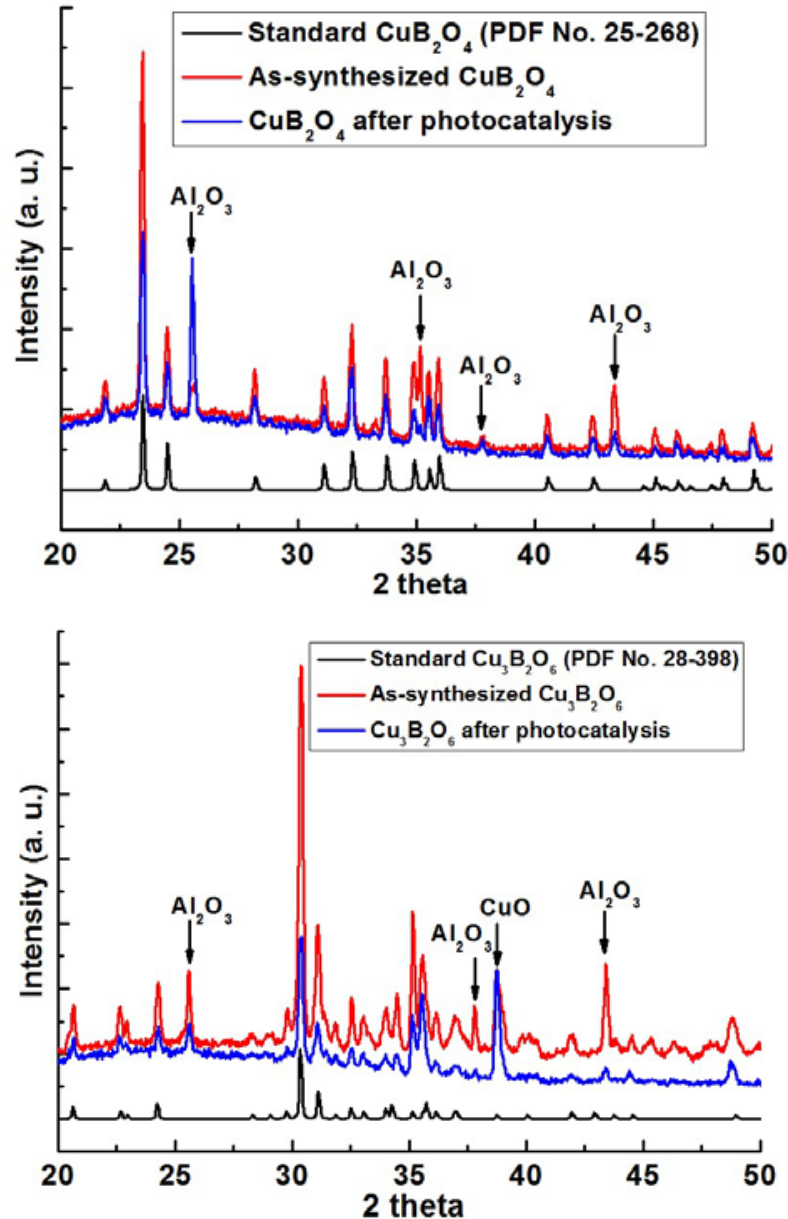


**Figure 3.2** XRD patterns of  $\text{CuB}_2\text{O}_4$  (top) and  $\text{Cu}_3\text{B}_2\text{O}_6$  (bottom).

Scanning electron microscope (SEM) images reveal that the  $\text{CuB}_2\text{O}_4$  particles are around 2  $\mu\text{m}$  in size and that the  $\text{Cu}_3\text{B}_2\text{O}_6$  particles exhibit the expected layered

morphology as shown in Figure 3.3. The specific surface areas of both copper borates are negligible based on BET measurements.

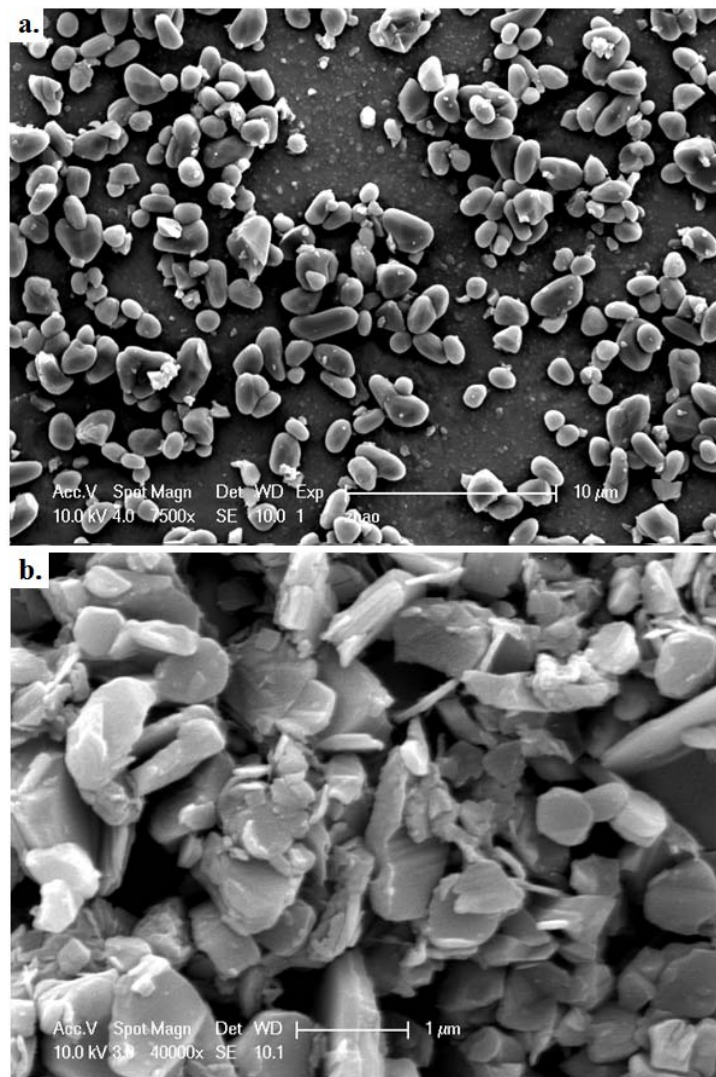


**Figure 3.3** SEM pictures of prepared (a) CuB<sub>2</sub>O<sub>4</sub> and (b) Cu<sub>3</sub>B<sub>2</sub>O<sub>6</sub>.

General survey X-ray photoelectron spectra (XPS) indicate the presence of Cu, B, O and C elements (C is from XPS instrument itself) in both samples (see Figure 3.4). As shown in the highly resolved Cu 2p spectra (see Figure 3.9), the peaks with binding

energies at  $\sim$ 935 eV and  $\sim$ 955 eV represent Cu 2p<sub>3/2</sub> and Cu 2p<sub>1/2</sub> respectively. The satellite peaks at  $\sim$ 944 eV and  $\sim$ 963 eV are characteristic of Cu<sup>2+</sup>.<sup>15</sup> The highly resolved B 1s spectra exhibits a peak with the binding energy  $\sim$ 192 eV, which is consistent with B<sup>3+</sup> in B<sub>x</sub>O<sub>y</sub> systems.<sup>16</sup>

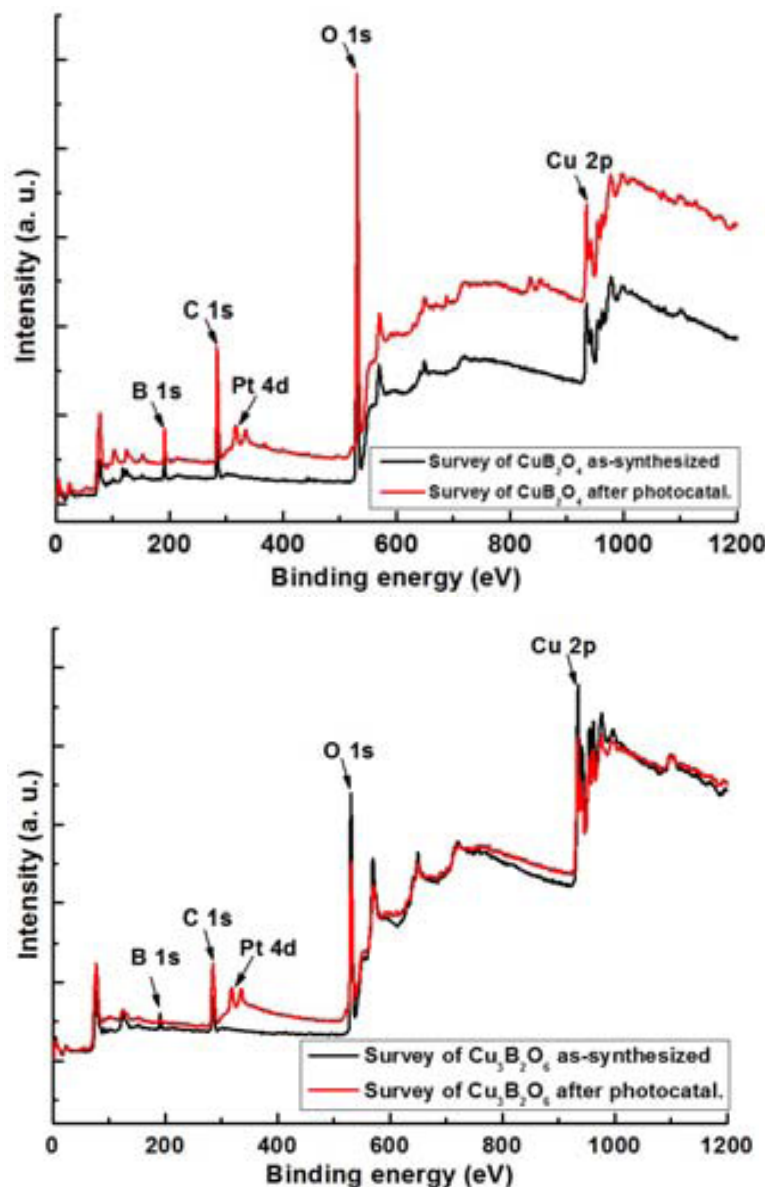


**Figure 3.4** General survey XPS spectra of copper borates before and after H<sub>2</sub> evolution.

The local chemical environments of  $\text{Cu}^{2+}$  in the two copper borates were characterized using electron spin resonance (ESR). At room temperature, no  $\text{Cu}^{2+}$  signal was detected for  $\text{Cu}_3\text{B}_2\text{O}_6$  while a strong  $\text{Cu}^{2+}$  signal appeared in  $\text{CuB}_2\text{O}_4$  (see Figure 3.5), indicating different local chemical environments of  $\text{Cu}^{2+}$  in the two copper borates. This agrees with previous research showing that the magnetic properties of the two copper borates are different.<sup>17</sup>

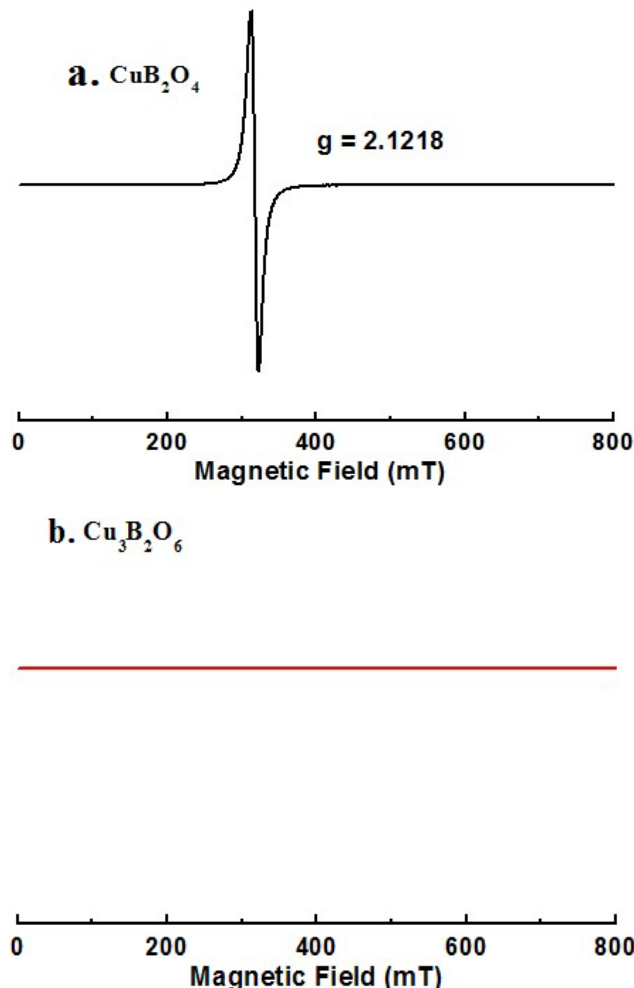


**Figure 3.5** The ESR spectra of (a)  $\text{CuB}_2\text{O}_4$  and (b)  $\text{Cu}_3\text{B}_2\text{O}_6$  at room temperature.

UV-visible absorption spectra of two samples are shown in Figure 3.6.  $\text{CuB}_2\text{O}_4$  exhibits a band absorption edge at 376 nm and an intense absorption peak near 635 nm. The latter peak is associated with the d-d transition absorptions of  $\text{Cu}^{2+}$ .<sup>18</sup> For  $\text{Cu}_3\text{B}_2\text{O}_6$ , the band absorption lies at 502 nm, while the broad d-d transition absorption peak occurs at 697 nm.

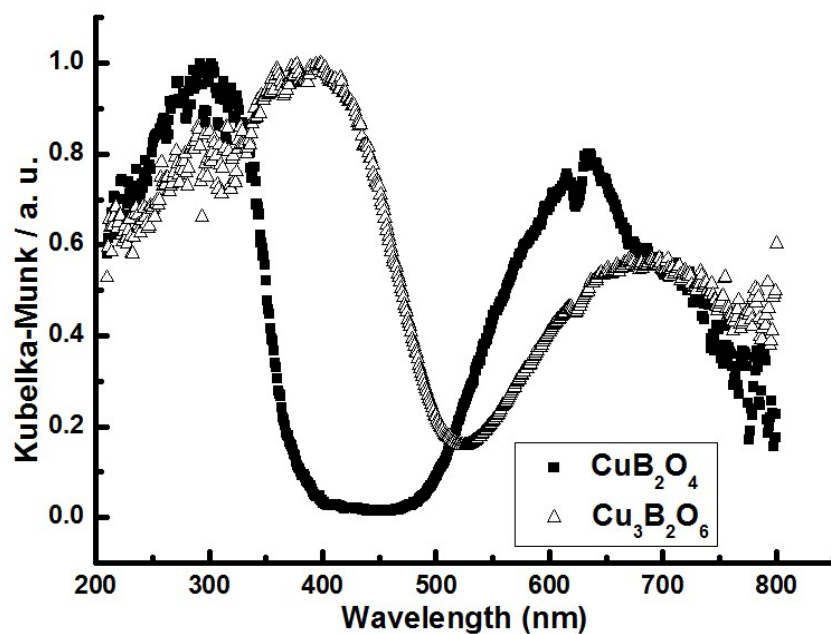


**Figure 3.6** Diffuse reflectance spectra for  $\text{CuB}_2\text{O}_4$  (■) and  $\text{Cu}_3\text{B}_2\text{O}_6$  ( $\Delta$ ).

### 3.4.2 Study of Photocatalytic Water Splitting

We studied the photocatalytic properties of the synthesized copper borates for the evolution of  $\text{H}_2$  and  $\text{O}_2$  from water in the presence of sacrificial agents. Under Xe lamp irradiation, the  $\text{O}_2$  and  $\text{H}_2$  evolution rates of  $\text{CuB}_2\text{O}_4$  are  $\sim 13.69 \mu\text{mol/h}/0.1\text{g}$  and  $\sim 6.95 \mu\text{mol/h}/0.1\text{g}$ , measured with  $\text{AgNO}_3$  and methanol aqueous solutions as sacrificial agents,

respectively. But for  $\text{Cu}_3\text{B}_2\text{O}_6$ , the  $\text{O}_2$  and  $\text{H}_2$  evolution rates are only  $\sim 7.2 \mu\text{mol}/\text{h}/0.1\text{g}$  and  $\sim 1.49 \mu\text{mol}/\text{h}/0.1\text{g}$ , respectively. Very interestingly, we also observed  $\text{O}_2$  and  $\text{H}_2$  evolution under visible light irradiation as shown in Figure 3.7.

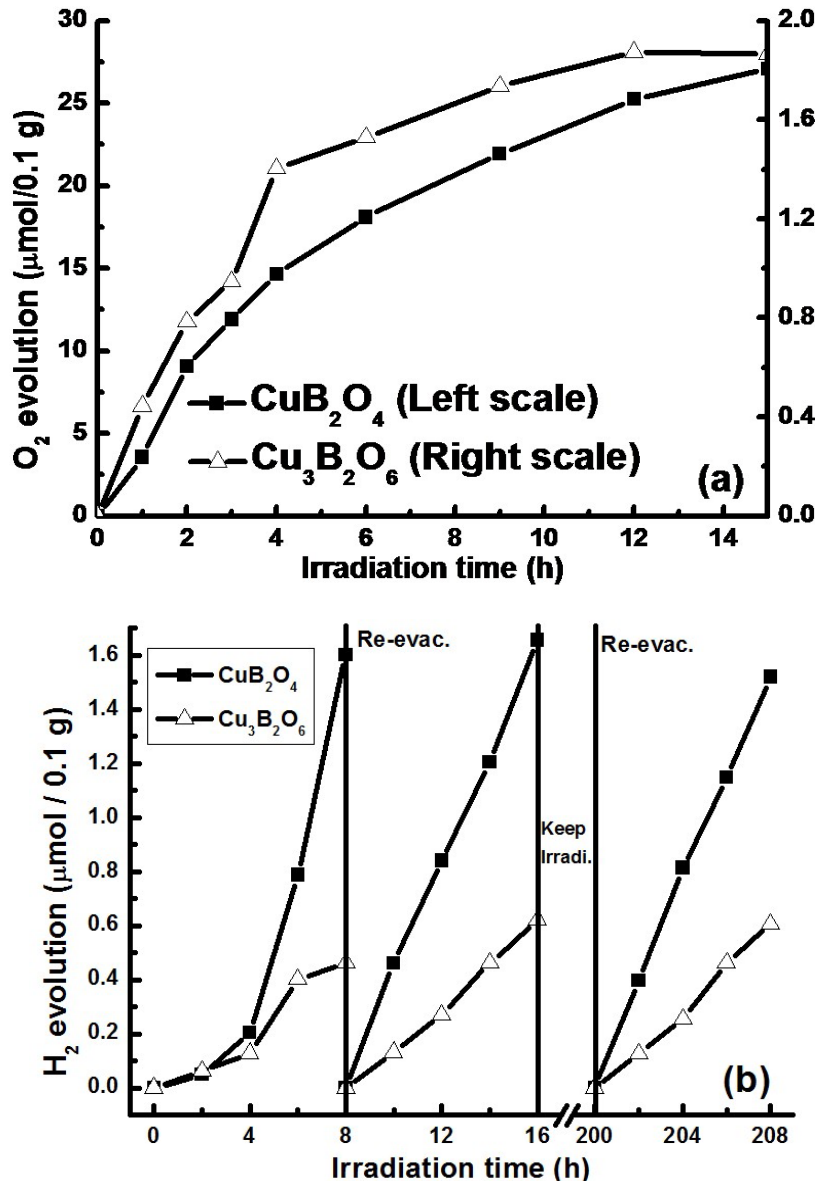


**Figure 3.7** (a)  $\text{O}_2$  evolution data as a function of time under visible light ( $>400 \text{ nm}$ ). (b) Time course of  $\text{H}_2$  evolution under visible light irradiation ( $>400 \text{ nm}$ ). Symbol:  $\text{CuB}_2\text{O}_4$  ( $\blacksquare$ ) and  $\text{Cu}_3\text{B}_2\text{O}_6$  ( $\triangle$ ).

In Figure 3.7(a), the photocatalytic O<sub>2</sub> evolution decreased over time because metallic silver (from sacrificial agent AgNO<sub>3</sub>) was deposited on the surface and shielded incident light as a result of Ag<sup>+</sup> reduction.<sup>19</sup> Therefore, the activity was determined from the fastest O<sub>2</sub> evolution rate (the first two hours),<sup>19</sup> which was ~4.53 μmol/h/0.1g for CuB<sub>2</sub>O<sub>4</sub> and ~0.39 μmol/h/0.1g for Cu<sub>3</sub>B<sub>2</sub>O<sub>6</sub>. Figure 3.7(b) shows the time course of H<sub>2</sub> evolution. The H<sub>2</sub> evolution rates of CuB<sub>2</sub>O<sub>4</sub> and Cu<sub>3</sub>B<sub>2</sub>O<sub>6</sub> are ~0.2 μmol/h/0.1g and ~0.08 μmol/h/0.1g, respectively. No noticeable decrease in photocatalytic activity was observed after 200 hours illumination, indicating the high photocatalytic stability of prepared copper borates.

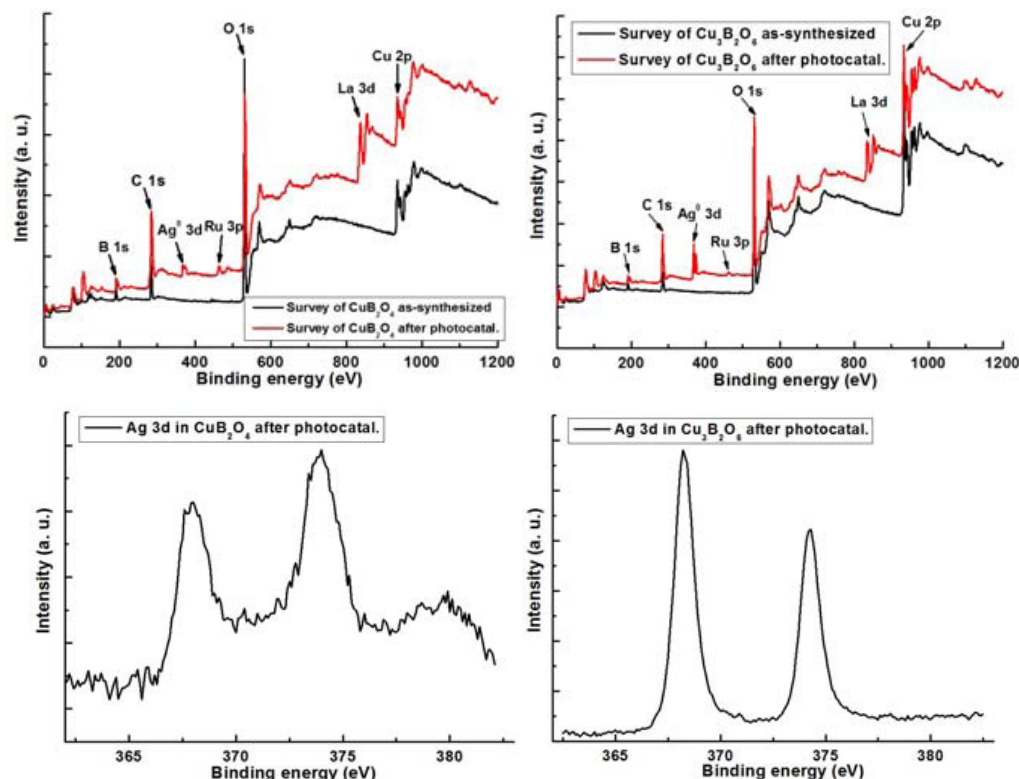


**Figure 3.8** XPS spectra of copper borates before and after O<sub>2</sub> evolution reaction (bottom: highly resolved XPS spectra of Ag 3d after O<sub>2</sub> evolution reaction).

To further confirm the photocatalytic process and the stability of the copper borates, the XPS spectra were taken after the photocatalytic reactions. As shown in Figure 3.8, the XPS spectra after O<sub>2</sub> evolution reactions show the appearance of Ag<sup>0</sup>, which further confirms that O<sub>2</sub> is generated by the title compounds.

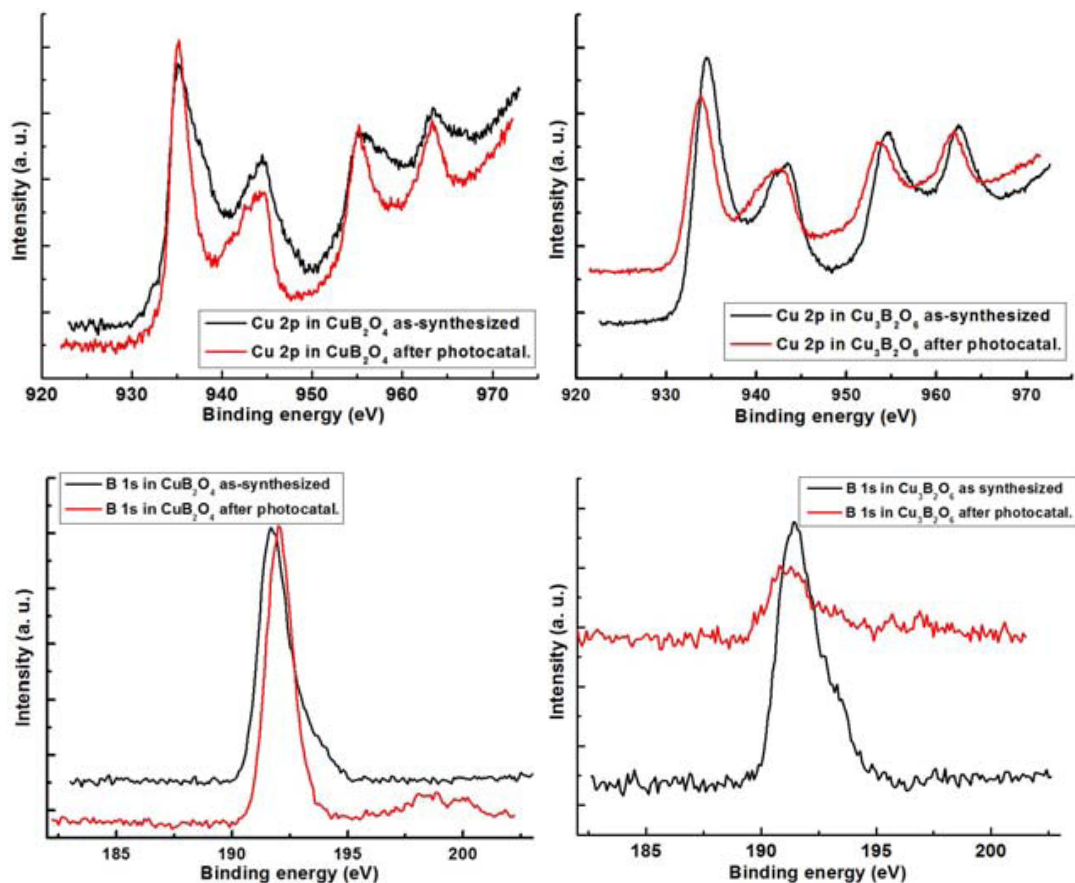


**Figure 3.9** XPS spectra of copper borates before and after H<sub>2</sub> evolution reaction.

After a long term H<sub>2</sub> evolution reaction, no noticeable phase changes were observed between powder XRD spectra taken before and after photocatalysis (see Figure 3.2). We also performed the XPS measurements after the H<sub>2</sub> evolution reactions as shown

in Figure 3.9. Although there are small shifts of the binding energies after photocatalytic reactions, which may be aroused by loading Pt, the oxidation states of Cu<sup>2+</sup> and B<sup>3+</sup> do not change based on XPS spectra, indicating the stability of the copper borates photocatalysts.

The water-splitting reactions proceeded catalytically, as indicated by calculated turnover numbers (generated H<sub>2</sub> to the amount of photocatalyst used) greater than 1 as shown in Experimental Section (Photocatalytic Experiments). Control experiments were conducted to exclude the possibility of mechano-catalytic water splitting (see Experimental Section: Photocatalytic Experiments).<sup>20</sup> The apparent quantum yield (AQY) of CuB<sub>2</sub>O<sub>4</sub> was determined with a band-pass filter at various wavelengths from 300 nm to 700 nm (see Table 3.1). At a typical visible light wavelength (420 nm), the AQY for O<sub>2</sub> evolution was 6.39% and for H<sub>2</sub> evolution it was 0.06%. No activity can be observed with the light at 700 nm since the d-d transition absorption of CuB<sub>2</sub>O<sub>4</sub> occurs at ~635 nm. The photocatalytic activities were also observed even at 500 nm and 600 nm, indicating that the d-d transition absorption of CuB<sub>2</sub>O<sub>4</sub> undoubtedly contributes to the visible light responses. As shown in Table 3.1, when applied with a 300 nm filter, the AQYs of CuB<sub>2</sub>O<sub>4</sub> for both H<sub>2</sub> and O<sub>2</sub> evolution were remarkably enhanced. At the wavelength of 300 nm, the band absorption of CuB<sub>2</sub>O<sub>4</sub> can be stimulated, which contributes to the enhanced AQYs. The detailed explanations on the mechanism are further studied by

theoretical calculations and presented as following.

**Table 3.1** Apparent Quantum Yield of CuB<sub>2</sub>O<sub>4</sub> at different wavelengths

Wavelength	300 nm	420 nm	500 nm	600 nm	700 nm
AQY of H <sub>2</sub>	0.67%	0.06%	0.045%	0.034%	0%
AQY of O <sub>2</sub>	10.6%	6.39%	3.74%	1.3%	0%

### 3.4.3 Study of DOS Calculations

To understand the origin of and differences in the photocatalytic activities of the two copper borates, the projected density of states (PDOS) for both compounds was computed with the LSDA+U method<sup>11</sup> using planewave DFT and the projector-augmented wave method,<sup>10</sup> as implemented in VASP.<sup>9</sup> For CuB<sub>2</sub>O<sub>4</sub>, empirical on-site Coulomb and exchange parameters U(Cu)=7.5 eV and J(Cu)=0.98 eV, which have previously been demonstrated to provide a good description of Cu 3d<sup>9</sup> systems,<sup>4</sup> were used. We expect these LSDA+U calculations to be a good approximation to the paramagnetic states found in both compounds at the experimental temperatures.<sup>17(a), 21</sup> We also performed the calculations of the antiferromagnetically ordered ground states of both compounds and the resulting PDOS are similar.

As shown in Figure 3.10, these calculations predict an intrinsic midgap state between the VB and CB with a population peak maximum at ~2.1 eV for CuB<sub>2</sub>O<sub>4</sub>, which corresponds fairly well to the experimental d-d absorption peak at 635 nm (1.95 eV). As indicated by the ESR spectra, the local Cu<sup>2+</sup> chemical environment in Cu<sub>3</sub>B<sub>2</sub>O<sub>6</sub> differs

from that in  $\text{CuB}_2\text{O}_4$ , suggesting that an alternate set of LSDA+U parameters is needed. The parameters  $U(\text{Cu})=6.0$  eV and  $J(\text{Cu})=0.98$  eV were chosen because they shift the midgap state population maximum to  $\sim 1.8$  eV, which corresponds to the experimental d-d absorpion peak maximum of 697 nm (1.78 eV). This parameter change moderately shifts the position of the midgap state peaks, but it does not significantly alter the qualitative peak shapes of the midgap states.

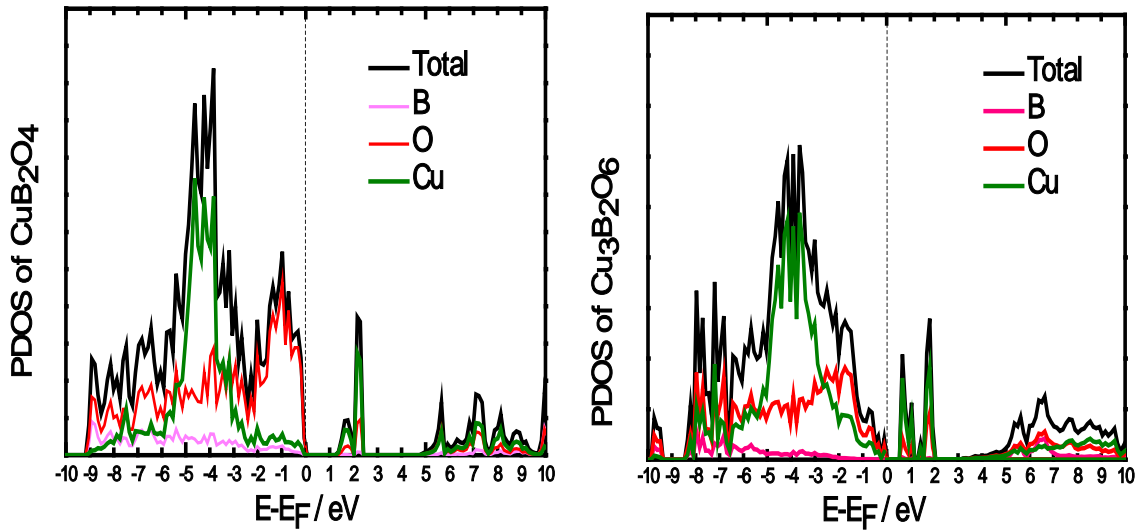


**Figure 3.10** The comparison of total and projected density of states (PDOS) using LSDA+U for (a)  $\text{CuB}_2\text{O}_4$  and (b)  $\text{Cu}_3\text{B}_2\text{O}_6$ .

Figure 3.11 presents the calculations of the antiferromagnetically ordered ground states of both compounds and the resulting PDOS are similar.

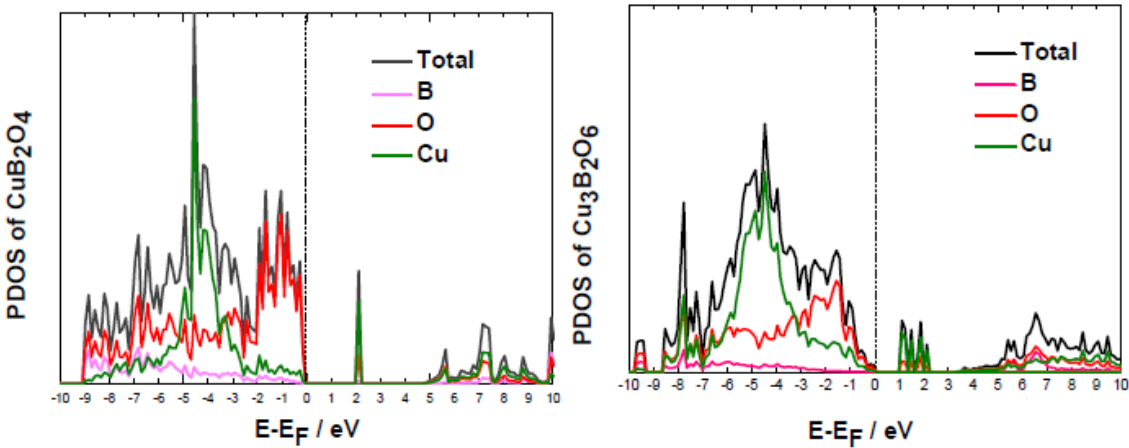


**Figure 3.11** LSDA+U PDOS in antiferromagnetically ordered ground state. U(Cu)=7.5 eV, J(Cu)=0.98 eV are used for both  $\text{CuB}_2\text{O}_4$  and  $\text{Cu}_3\text{B}_2\text{O}_6$ .

Since  $\text{O}_2$  evolution was observed, the VBs of the copper borates are both more positive than +1.23 V vs Standard Hydrogen Electrode (SHE). Therefore, the midgap states must lie at least 1.23 eV above the VB for photocatalytic  $\text{H}_2$  production to occur. As shown in Figure 3.10, the most intense midgap peak of  $\text{CuB}_2\text{O}_4$  at  $\sim 2.1$  eV easily satisfies this. In contrast, for  $\text{Cu}_3\text{B}_2\text{O}_6$ , most of the midgap state band lies below 1.23 eV, which is unsuitable for  $\text{H}_2$  production. This prediction holds true for a fairly broad range of possible LSDA+U parameters, including both parameter sets mentioned above.

Figure 3.12 schematically illustrates the relative positions of the midgap states in the copper borates. When irradiating  $\text{Cu}_3\text{B}_2\text{O}_6$  with visible light, electronic excitations to the midgap states are thermodynamically more preferable than to the CB. However, the excited electrons in the midgap states of  $\text{Cu}_3\text{B}_2\text{O}_6$  can not perform photocatalytic water reduction due to its unsuitable band position. The electrons excited from VB to CB are responsible for the observed  $\text{H}_2$  production. This accounts for the low photocatalytic

activities of the compound. In other words, rather than promoting water splitting, the midgap states in  $\text{Cu}_3\text{B}_2\text{O}_6$  actually serve as trap states that promote charge recombination.

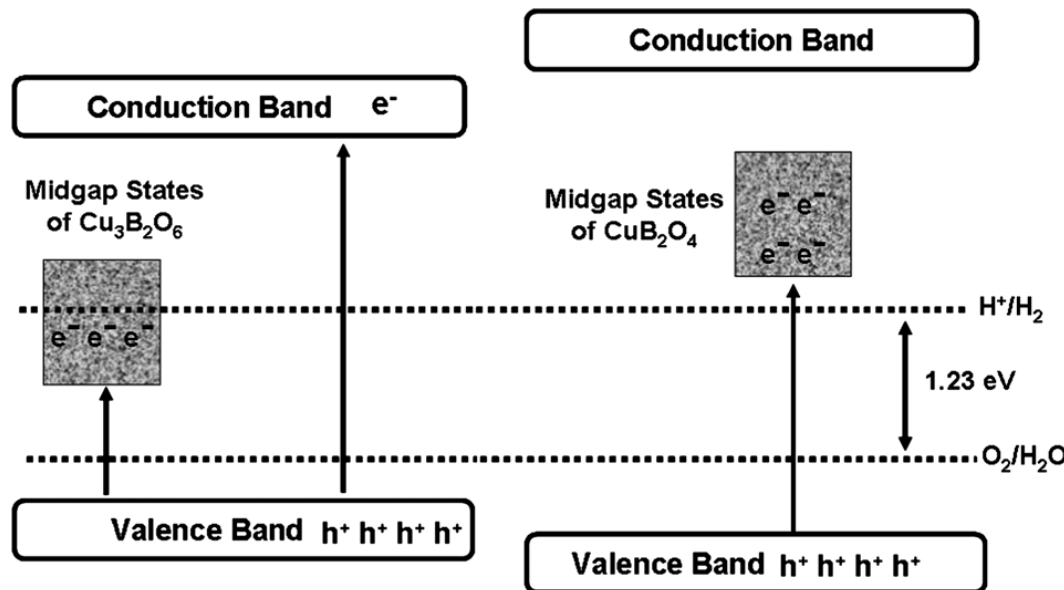


**Figure 3.12** Schematic of the band structures and midgap states of the two copper borates and possible electronic excitations under visible light irradiation.

The d-d transition effects of noble metals were recently explored for photocatalytic water splitting,<sup>22</sup> but in general, symmetry restrictions and selection rules limit d-d transition effects in materials. However, recent research suggests that  $\text{CuB}_2\text{O}_4$  has excellent d-d transition properties because both the electric-dipole and magnetic-dipole d-d transitions are allowed in the specific local coordination of  $\text{Cu}^{2+}$  sites,<sup>23</sup> which could be one possible reason for the relatively good photocatalytic performance of  $\text{CuB}_2\text{O}_4$ . Therefore, for  $\text{CuB}_2\text{O}_4$  which has band gap energy in UV region, the suitable midgap states position and unique d-d transition effects bestow the compound with visible light absorption and enhance its photocatalytic water splitting activity under visible light.

In contrast, the midgap states for  $\text{Cu}_3\text{B}_2\text{O}_6$  actually act as trap states as in  $\text{CaCu}_3\text{Ti}_4\text{O}_{12}$ <sup>4</sup> and other doped materials.<sup>24</sup>

### 3.5 Conclusion

In conclusion, two copper borates that photocatalytically evolve  $\text{H}_2$  and  $\text{O}_2$  from water under visible light were investigated. Both undoped materials exhibit intrinsic midgap states whose properties are determined by the crystal structures and coordination environments of the photocatalysts. However, these midgap states behave differently during photocatalysis. For the large-band-gap  $\text{CuB}_2\text{O}_4$ , the midgap states facilitate visible light absorption and photocatalytic water splitting, while for the smaller-band-gap  $\text{Cu}_3\text{B}_2\text{O}_6$ , the midgap states trap electrons leading to the reduction of the photocatalytic activity. This study illustrates that the midgap band position can be critical to the overall photocatalytic performance. Photocatalytic function based on the d-d transition effects of  $\text{Cu}^{2+}$  is exciting and may promote the exploration of other transition metals d-d transition effects for photocatalytic water splitting.

### 3.6 References

- (1) (a) Chen, X.; Shen, S.; Guo, L.; Mao, S. S. *Chem. Rev.* **2010**, *110*, 6503; (b) Kudo, A.; Miseki, Y. *Chem. Soc. Rev.* **2009**, *38*, 253; (c) Osterloh, F. E. *Chem. Mater.* **2008**, *20*, 35; (d) Kitano, M.; Hara, M. *J. J. Mater. Chem.* **2010**, *20*, 627; (e) Maeda, K.; Domen, K. *J. Phys. Chem. C* **2007**, *111*, 7851; (f) Chen, C.; Ma, W.; Zhao, J. *Chem. Soc. Rev.* **2010**, *39*, 4206.
- (2) Joshi, U. A.; Palasyuk, A.; Arney, D.; Maggard, P. A. *J. Phys. Chem. Lett.* **2010**, *1*, 2719.
- (3) (a) Chen, X.; Mao, S. S. *Chem. Rev.* **2007**, *107*, 2891; (b) Kato, H.; Kudo, A. *J. Phys. Chem. B* **2002**, *106*, 5029; (c) Cao, Y.; Yang, W.; Zhang, W.; Liu, G.; Yue, P. *New J. Chem.* **2004**, *28*, 218; (d) Asahi, R.; Morikawa, T.; Ohwaki, T.; Aoki, K.; Taga, Y. *Science* **2001**, *293*, 269; (e) Chen, X.; Burda, C. *J. Am. Chem. Soc.* **2008**, *130*, 5018.
- (4) Clark, J. H.; Dyer, M. S.; Palgrave, R. G.; Ireland, C. P.; Darwent, J. R.; Claridge, J. B.; Rosseinsky, M. J. *J. Am. Chem. Soc.* **2011**, *133*, 1016.
- (5) Anantharamulu, A.; Kumar, V. B.; Devi, R. V.; Sarojini, T.; Anjaneyulu, C.; Vithal, M. *Bull. Mater. Sci.* **2009**, *32*, 421.
- (6) Fukaya, A.; Watanabe, I.; Nagamine, K. *J. Phy. Soc. Jpn.* **2001**, *70*, 2868.
- (7) Inoue, Y.; Hayashi, O.; Sato, K. *J. Chem. Soc., Faraday Trans.* **1990**, *86*, 2277.
- (8) Wang, X.; Maeda, K.; Thomas, A.; Takanabe, K.; Xin, G.; Carlsson, J. M.; Domen, K.; Antonietti, M. *Nature Mater.* **2009**, *8*, 76.
- (9) Kresse, G.; Furthmuller, J. *Phys. Rev. B* **1996**, *54*, 11169.
- (10) Kresse, G.; Joubert, D. *Phys. Rev. B* **1999**, *59*, 1758.
- (11) (a) Anisimov, V. I.; Zaanen, J.; Andersen, O. K. *Phys. Rev. B* **1991**, *44*, 943. (b) Dudarev, S. L.; Botton, G. A.; Savrasov, S. Y.; Humphreys, C. J.; Sutton, A. P. *Phys. Rev. B* **1998**, *57*, 1505.
- (12) Martinez-Ripoll, M.; Martinez-carrera, S.; Garcia-blanco, S. *Acta Crystallogr., Sect.*

A: *Cryst. Phys., Diffr., Theor. Gen. Crystallogr.* **1971**, B27, 677.

- (13) Bandara, J.; Udwatta, C. P. K. *Photochem. Photobiol. Sci.* **2005**, 4, 857.
- (14) Behm, H. *Acta Crystallogr., Sect. A: Cryst. Phys., Diffr., Theor. Gen. Crystallogr.* **1982**, B38, 2781.
- (15) Briggs, D.; Riviere, J. C. in *Practical Surface Analysis*, ed. Briggs, D; Seah, M. P. *John Wiley & Sons*, New York, 2nd edn, **1990**, vol. 1, p. 131.
- (16) Zheng, B.; Kwok, R. W. M. *J. Appl. Phys.* **2004**, 95, 3527.
- (17) (a) Petrakovskii, G.; Velikanov, D.; Vorotinov, A.; Balaev, A.; Sablina, K.; Amato, A.; Roessli, B.; Schefer, J.; Staub, U. *J. Magn. Magn. Mater.* **1999**, 205, 105. (b) Petrakovski, G. A.; Sablina, K. A.; Vorotynov, A. M.; Bayukov, O. A.; Bovina, A. F.; Bondarenko, G. V. *Phys. Solid State* **1999**, 41, 610.
- (18) Bezmaternykh, L. N.; Potseluko, A. M.; Erlykova, E. A.; Edelman, I. S. *Phys. Solid State* **2001**, 43, 309.
- (19) Kudo, A.; Omori, K.; Kato, H. *J. Am. Chem. Soc.* **1999**, 121, 11459.
- (20) (a) Ikeda, S.; Takata, T.; Kondo, T.; Hitoki, G.; Hara, M.; Kondo, J. N.; Domen, K.; Hosono, H.; Kawazoe, H.; Tanaka, A. *Chem. Commun.* **1998**, 2185. (b) Hitoki, G.; Takata, T.; Ikeda, S.; Hara, M.; Kondo, J. N.; Kakihana, M.; Domen, K. *Catal. Today*, **2000**, 63, 175.
- (21) Fukaya, A.; Watanabe, I.; Nagamine, K. *J. Phys. Soc. Jpn.* **2001**, 70, 2868.
- (22) (a) Frame, F. A.; Townsend, T. K.; Chamousis, R. L.; Sabio, E. M.; Dittrich, T.; Browning, N. D.; Osterloh, F. E. *J. Am. Chem. Soc.* **2011**, 115, 5081. (b) Kumagai, N.; Ni, L.; Irie, H. *Chem. Commun.* **2011**, 47, 1884.
- (23) Pisarev, R. V.; Kalashnikova, A. M.; Schops, O.; Bezmaternykh, L. N. *Phys. Rev. B: Condens. Matter Mater. Phys.* **2011**, 84, 075160.
- (24) (a) Wang, D.; Ye, J.; Kako, T.; Kimura, T. *J. Phys. Chem. B* **2006**, 110, 15824. (b) Li, Y.; Ma, G.; Peng, S.; Lu, G.; Li, S. *Appl. Surf. Sci.* **2008**, 254, 6831.

# **Chapter 4**

## **Boron Carbides as Efficient, Metal-Free, Visible-light-responsive Photocatalysts**

### **4.1 Introduction**

Semiconductor-based photocatalysts can convert solar energy into hydrogen by splitting water or decompose harmful environmental pollutants under ultraviolet Solar-powered photocatalytic and photoelectrochemical (PEC) water splitting provide two promising strategies to produce hydrogen for future energy needs. Currently, most photocatalytic or PEC water-splitting materials are based on transition metal oxide, (oxy)nitride, or (oxy)sulfide semiconductors with suitable band gaps and band positions.<sup>1</sup> However, finding stable, efficient, and low-cost materials that are active under visible light has proved challenging.

Metal-free photocatalytic materials are a promising new class of photocatalytic materials that have not been fully explored. In 2009, a novel metal-free polymeric photocatalyst, graphitic C<sub>3</sub>N<sub>4</sub> (g-C<sub>3</sub>N<sub>4</sub>),<sup>2</sup> was found to perform photocatalytic water splitting in the visible light region. The appealing electronic structure of this material, its chemical and physical stability, and its low cost make it potentially useful in a variety of applications.<sup>3</sup> However, few such metal-free photocatalysts are currently known: poly(p-phenylenes),<sup>4</sup> g-C<sub>3</sub>N<sub>4</sub>, C<sub>3</sub>N<sub>3</sub>S<sub>3</sub>,<sup>5</sup> a-sulfur<sup>6</sup> and red phosphorus.<sup>7</sup> Unfortunately, all

of these metal-free materials achieve sufficient efficiency only when loaded with scarce and expensive noble metal cocatalysts, as is also the case for PEC water splitting with these materials.<sup>8</sup> Moreover, although various p-type semiconductors exhibit sufficient efficiency as photocathode materials,<sup>1(c)</sup> their high cost and poor corrosion stability pose severe limitations on the potential application of these materials as photocathodes.

Herein, we demonstrate that stable and inexpensive boron carbides ( $B_{4.3}C$  and  $B_{13}C_2$ ), which are already used in large quantities for many industrial applications,<sup>9</sup> can also function as efficient visible-light-responsive photocatalysts for  $H_2$  evolution. Critically, the  $H_2$  evolution rate of  $B_{4.3}C$  is about two orders of magnitude larger than that of  $g\text{-}C_3N_4$ , without the need for noble metal cocatalysts (*ca.*  $2.9 \mu\text{mol h}^{-1}/0.2 \text{ g}$  *vs.* *ca.*  $0.035 \mu\text{mol h}^{-1}/0.2 \text{ g}$  for  $g\text{-}C_3N_4$  in the presence of sacrificial methanol). The apparent quantum yield of  $B_{4.3}C$  is also higher: 0.54% of Pt/ $B_{4.3}C$  *vs.* 0.23% of Pt/ $g\text{-}C_3N_4$  at 420 nm. Furthermore, the p-type semiconducting nature of the boron carbides makes them one of only a handful of known stable and efficient photocathode materials for PEC water reduction under visible light irradiation that do not require noble metal cocatalysts.<sup>10</sup> Density functional theory (DFT) calculations indicate that the inherent defects and structural distortions in  $B_{4.3}C$  cause a continuum downshift of its conduction band (CB) edge that facilitates visible-light absorption and water splitting. In  $B_{13}C_2$ , however, the more complicated structural defects and distortions result in a large number of midgap

states between the CB and the valence band (VB), which reduce its overall photocatalytic and PEC water splitting efficiency by promoting charge recombination.

## 4.2 Experimental Section

### 4.2.1 Method of Synthesis

The  $B_{4.3}C$ , labeled as “ $B_4C$ ” on the bottle, was purchased from Alfa Aesar (CAS: 12069-32-8). The  $B_{13}C_2$  was synthesized by arc-melting method. Typically, 26.3 g of crystalline boron reacts with 3.7 g of graphitic carbon under vacuum at  $3100^0C$  by arc-melting for 2 min. The product was cast in a water-cooled hearth and cooled to room temperature. Materials shattered on cooling and were re-melted by vacuum arc-melting and allowed to cool more slowly to inhibit shattering. The sintered bulky product was mashed into a powder by hammer, ball milling, and mortar/pestle milling. To remove possible impurities, such as boron oxides and transition metals, the boron carbide products were washed repeatedly with a sequence of HCl (2M), distilled water, and ethanol. The materials were then dried in air at  $70^0C$  overnight before use.

### 4.2.2 Characterizations

Powder X-ray diffraction data were collected using a Bruker D8-Advance powder diffractometer operating at 40 kV, 40 mA for Cu K $\alpha$  radiation ( $\lambda=1.5406\text{ \AA}$ ). The Raman spectra were obtained with a Nicolet Almega XR instrument using 532 nm laser excitations, laser power of less than 1.7 mW, spot size of 2.1 mm, spectral resolution of 4

$\text{cm}^{-1}$ . The UV-visible absorption spectra were recorded on a Shimadzu UV-3101PC UV-Vis-NIR spectrophotometer operating in the diffuse mode with application of Kubelka-Munk equation. The photoluminescence (PL) spectra of the photocatalyst were obtained by a Varian Cary Eclipse spectrometer with an excitation wavelength of 325 nm. SEM pictures and EDX were recorded on a Philips XL30 scanning electron microscope. A copper substrate was used to load the samples. A thin layer of Pt/Pd was sprayed onto the sample before measurement. The specific surface area was calculated using the BET (Brunauer-Emmett-Teller) method from the nitrogen adsorption data by using a Micromeritics ASAP 2020 surface-area and pore-size analyzer. The TGA analysis was performed using TGA Q500 V20.10 Build 36.

#### 4.2.3 Photocatalytic Experiments

Photocatalytic  $\text{H}_2$  production experiments were conducted in a sealed circulation system. In the run with co-catalysts, 2 wt% Pt was loaded by UV irradiation of  $\text{PtCl}_4$  aqueous solution. Typically, 0.200 g of sample was suspended in 240 mL 25% methanol aqueous solution (containing 0.0068 g  $\text{PtCl}_4$ ) under magnetic stirring. Then a 300 W Xe lamp was applied to this mixture for 30 minutes, in that case, Pt nanoparticles would be loaded to the surface of boron carbides as co-catalysts. After degassing the system for about half an hour, this 300 W Xe lamp with a 420 nm cut-on filter (Newport Corp.) was applied to execute the photocatalytic reaction. The products of  $\text{H}_2$  were analyzed by gas

chromatography (Shimadzu GC-8A) equipped with a thermal conductivity detector (TCD). In the run without co-catalysts, except omitting loading Pt, all the other experimental conditions are the same.

To confirm the H<sub>2</sub> is coming from the photocatalytic reaction, the amount of H<sub>2</sub> we actually collected must exceed the amount of photocatalysts we used in the experiment (Turnover number > 1). To facilitate the measurements, H<sub>2</sub> was collected by illuminating the reaction using the 300W Xe lamp without any filter. For B<sub>4.3</sub>C, we collected 7003.3 μmol of H<sub>2</sub>, which exceeds the amount of B<sub>4.3</sub>C (0.2 g, 3419.8 μmol) used in the experiment. For B<sub>13</sub>C<sub>2</sub>, we collected 2653.5 μmol of H<sub>2</sub>, which exceeds the amount of B<sub>13</sub>C<sub>2</sub> (0.2 g, 1215.6 μmol) used in the experiment.

The apparent quantum yield (AQY) was calculated based on the following equation: AQY of H<sub>2</sub> evolution = 100% × [(number of evolved H<sub>2</sub> molecules) × 2] / (number of incident photons). A 420 nm bandpass filter (Newport Corp.) was applied. The number of incident photons was determined using a radiant power energy meter (Newport Corp., Model 70260 with a Thermopile Detector).

In order to further confirm the H<sub>2</sub> was generated from the photocatalytic reaction, the control experiments were performed as follows. Set up a H<sub>2</sub> evolution trial according to the above experimental conditions and wrap the reactor with aluminum foils thoroughly. Sample the system every 30 minutes for 2 hours. No H<sub>2</sub> was observed, which

excludes that the H<sub>2</sub> is from mechano-catalytic water splitting. To further verify that boron carbides do perform photocatalytic water splitting, we illuminated 25% aqueous methanol solution without adding any boron carbides. No H<sub>2</sub> was collected.

#### **4.2.4 Photoelectrochemical (PEC) Experiments**

The photoelectrodes of boron carbides were fabricated by an electrophoretic deposition (EPD) method. Typically, boron carbide powders were suspended in isopropyl alcohol with a concentration of 0.5 mg/mL. In order to achieve surface charges on the boron carbide powders, a small amount of Mg(NO<sub>3</sub>)<sub>2</sub>•6H<sub>2</sub>O (10<sup>-3</sup> M) was added into the suspension. The final suspension was sonicated at room temperature for 1 hour before EPD. The fluorine-doped tin-oxide (FTO) glass (~1 cm x 2 cm) was subsequently sonicated in distilled water, ethanol and acetone for 30 minutes and naturally dried before use.

For EPD, the FTO glass was used as working electrode and a Pt foil was used as counter electrode. The distance between the two electrodes was fixed at 2 cm. A direct-current voltage of -50 V was applied between the electrodes for 2 minutes. The boron carbides deposited FTO glass was washed with distilled water and dried naturally before use. Photocurrent densities were measured using a Solartron SI 1287 electrochemical interface analysis instrument operated in a standard three-electrode configuration with an FTO electrode deposited with boron carbides as photocathode (an

effective area of 1.5 cm<sup>2</sup>), a Pt foil as counter electrode, and a saturated calomel electrode (SCE) as reference electrode. 0.01 M Na<sub>2</sub>SO<sub>4</sub> (20 mL) was used as the electrolyte. A 300 W Xenon lamp (Oriel) with a filter to remove light of wavelengths below 420 nm was used as the visible light source to provide a light intensity of 64 mW•cm<sup>-2</sup>.

#### 4.3 Density of States (DOS) Calculations

The B<sub>4.3</sub>C and B<sub>13</sub>C<sub>2</sub> materials are modeled as a 5 x 1 x 1 supercell of hexagonal boron carbide. Defects were introduced in ratios that closely approximate previous experimental reports.<sup>9</sup>

In B<sub>4.3</sub>C, the concentration of B<sub>12</sub> icosahedral: B<sub>11</sub>C icosahedra: C-B-C: C-B-B: B-vacancy-B structural elements is 0 : 100 : 80 : 20 : 0. In other words, it contains 15 3-atom-chains and 15 12-atom-icosahedra. 12 3-atom-chains are C-B-C and 3 3-atom-chains are C-B-B. All icosahedra are (B<sub>11</sub>C). Because of the existence of nonequivalent atomic positions within the icosahedra, two variants of (B<sub>11</sub>C)CBC should be considered: the polar (B<sub>11</sub>C) configuration, where one of the boron atoms in the icosahedron is substituted by carbon in the polar site, and the equatorial (B<sub>11</sub>C) configuration, where the substitution occurs in the equatorial site. The polar configuration is found to be energetically preferred to the equatorial one in all studies where the two structures have been modeled within the same calculation framework.<sup>11</sup> The polar sites correspond to those atoms that link the icosahedra together. The equatorial sites on the

other hand are those to which the 3-atom chains are bonded. It was found that the placement of carbon atoms i.e., which boron atom was replaced by carbon in the icosahedral polar sites and alternative arrangements of substituted icosahedral in supercells do not significantly alter the electronic properties.<sup>12</sup>

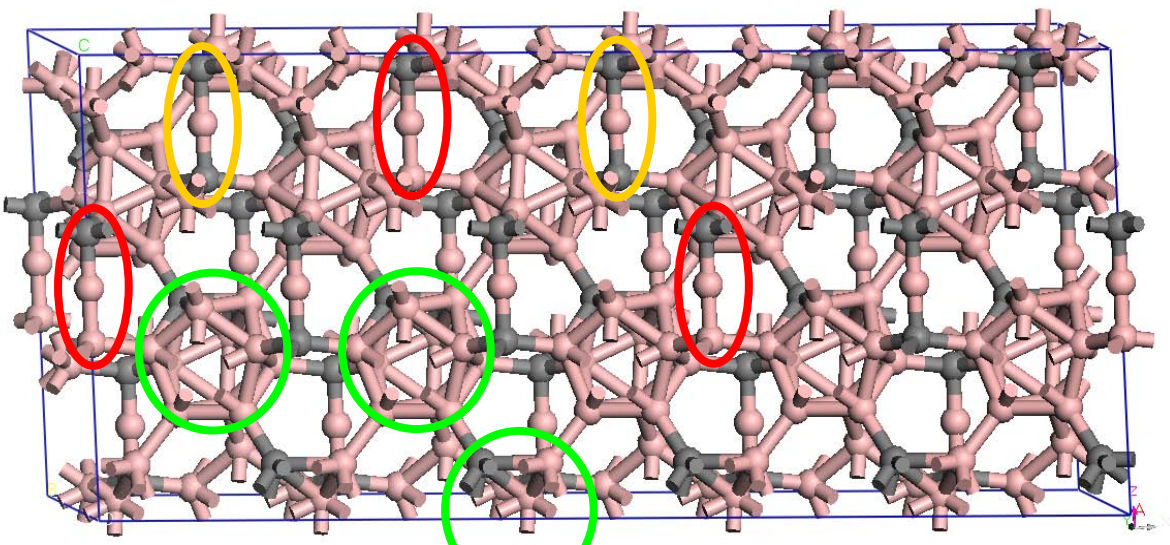


**Figure 4.1** Supercell model of  $B_{4.3}C$ . Red ellipses show C-B-B chains; Yellow ellipses show the C-B-C chains. Green circles show  $B_{11}C^{\text{polar-site}}$  icosahedra.

In  $B_{13}C_2$ , the  $B_{12}$  icosahedral:  $B_{11}C$  icosahedra: C-B-C: C-B-B: B-vacancy-B ratio is 40 : 60 : 60 : 20 : 20. In the  $5 \times 1 \times 1$  supercell, this amounts to 15 chains and 15 icosahedra with the following distribution: 9 chains are C-B-C, 3 chains are C-B-B, and 3 chains are B-vacancy-B. 9 icosahedra are ( $B_{11}C$ ), and 6 icosahedra are ( $B_{12}$ ).

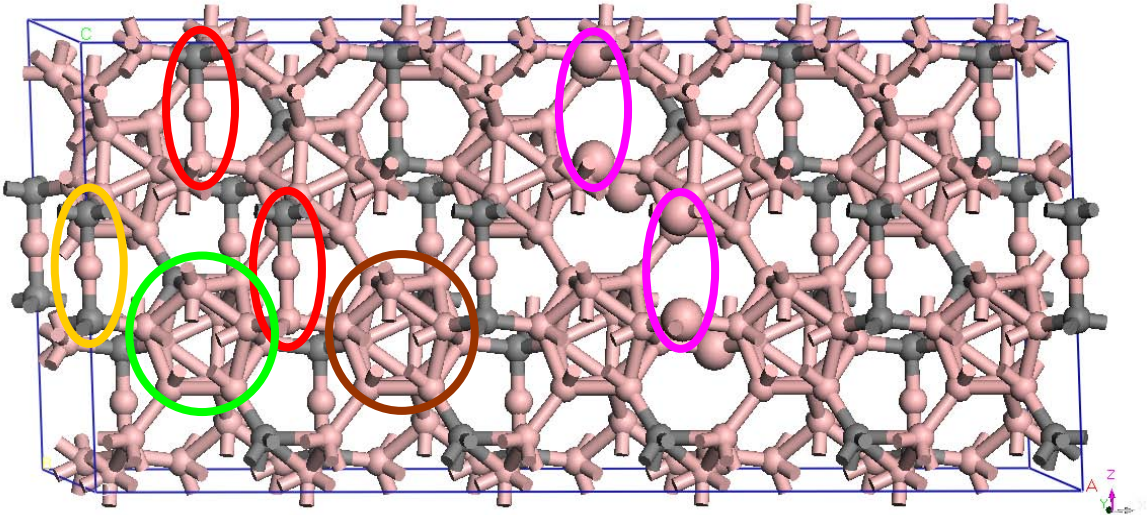


**Figure 4.2** Supercell model of  $B_{13}C_2$ . Red ellipses show C-B-B chains; Yellow ellipses show the C-B-C chains; Purple ellipses show the B-vacancy-B chains; Green circles show  $B_{11}C^{\text{polar-site}}$  icosahedra; Brown circles show the  $B_{12}$  icosahedra.

DFT Computational details: The DOS calculations were performed using the Perdew-Burke-Ernzerhof (PBE)<sup>13</sup> functional and projector-augmented wave (PAW) method to describe core electrons,<sup>14</sup> as implemented in VASP.<sup>15</sup> Reciprocal space integrations were performed using a 2 x 4 x 2 Monkhorst-Pack k-point mesh (gamma-point centered grid). As is recommended for the PAW approach with first-row elements like B and C, a large planewave cutoff energy of 700 eV was used. The tetrahedron method with Blöchl corrections (ISMEAR = -5) was used to obtain the DOS.

## 4.4 Results and Discussion

### 4.4.1 Instrumental Characterizations

Boron carbides have a rhombohedral structure with space group R-3m.<sup>16</sup> They are composed of  $B_{12}$  or  $B_{11}C$  icosahedra, which distort slightly at each vertex owing to

Jahn-Teller effects, and which are connected by mostly linear three-atom chains on the main cell diagonal (the crystallographic c direction).<sup>17</sup> Disordered combinations of the 12-atom icosahedra and three-atom chains (C-B-C, B-Vacancy-B, C-B-B) lead to elementary cells with different stoichiometric compositions which are statistically distributed over the whole structure.<sup>18</sup> The idealized boron carbide elementary cell is shown in Figure 4.3.

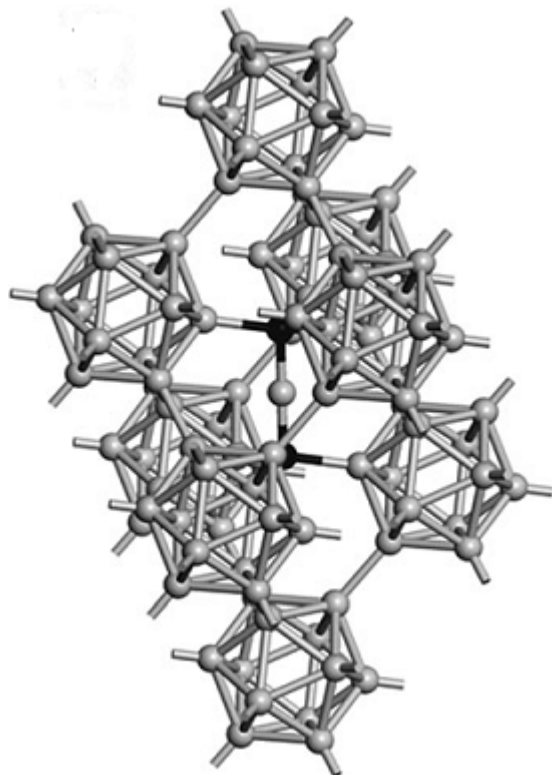


**Figure 4.3** Idealized elementary cell of boron carbides. B gray, C black.

The boron carbides were primarily evaluated by X-ray diffraction (XRD), FT-Raman spectroscopy, photoluminescence (PL) spectroscopy, scanning electron microscopy (SEM), thermogravimetric analysis (TGA), and energy-dispersive X-ray

spectroscopy (EDX).

The XRD patterns in Figure 4.4 match that of either  $B_{4.3}C$  or  $B_{13}C_2$ , although their identical crystal structures make it difficult to distinguish between them based on the XRD patterns. The small low-angle shift for  $B_{13}C_2$  compared to  $B_{4.3}C$  indicates that the former has larger unit cells, which is in agreement with previous results.<sup>19</sup> Both boron carbides contain a small amount of free graphitic carbon, which is rather common in both commercial boron carbides<sup>17</sup> and boron carbides synthesized by arc-melting.<sup>20</sup> However, the graphitic carbon is not active in either photocatalytic or PEC water splitting.

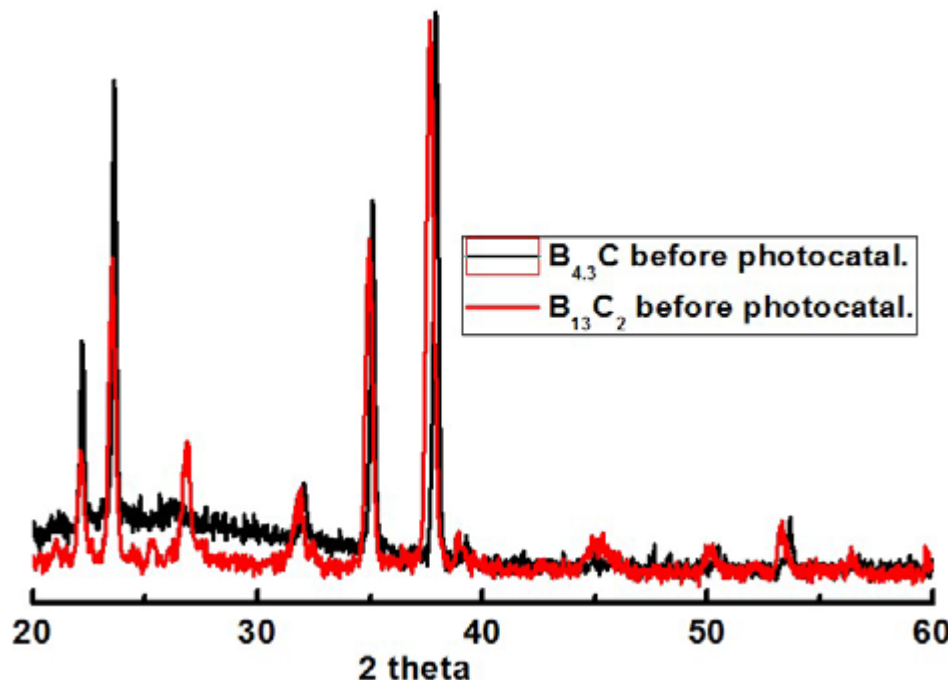


**Figure 4.4** XRD patterns: (a)  $B_{4.3}C$  and  $B_{13}C_2$

FT-Raman spectroscopy was used to further identify the two boron carbides. The FT-Raman spectra shown in Figure 4.5 are in good agreement with a previous FT-Raman

study on various boron carbides.<sup>21</sup> Compared to  $B_{4.3}C$ , the two narrow bands near  $500\text{ cm}^{-1}$  and the broad bands near  $300\text{ cm}^{-1}$  disappear in our synthesized boron carbide, and a broad band near  $370\text{ cm}^{-1}$  appears. These changes correspond to the replacement of C-B-C chains with C-B-B chains and indicate that the C content is 13% ( $B_{13}C_2$ ) or lower.<sup>21</sup> However,  $B_xC$  with lower C content than  $B_{13}C_2$  are unlikely here, because they would be metastable and would yield different crystal structures, such as  $B_8C$  (orthorhombic) or  $B_{25}C$  (tetragonal), which would be inconsistent with the observed XRD pattern of the synthesized boron carbide.<sup>22</sup> Theoretical calculations of the enthalpies of formation for the ideal boron carbide structures also indicate that materials with the stoichiometries of  $B_4C$  and  $B_{13}C_2$  have the lowest enthalpies of formation.<sup>23</sup> The combination of this evidence indicates that the synthesized boron carbide is  $B_{13}C_2$ .

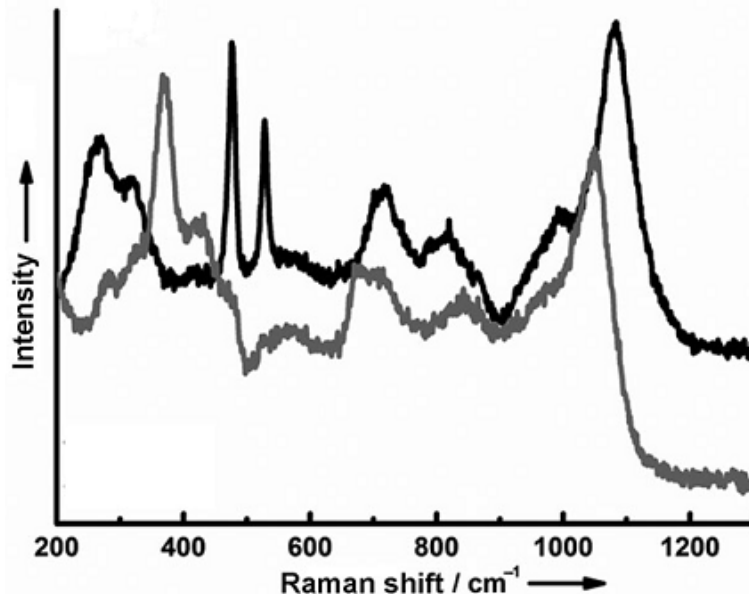


**Figure 4.5** FT-Raman spectra.  $B_{13}C_2$  (gray),  $B_{4.3}C$  (black).

Because of the dark coloration and high absorption coefficient of boron carbides, the powder samples show high absorption in the full region of 310-800 nm by UV/Vis diffuse reflectance spectroscopy in Figure 4.6(top). Instead, the PL spectroscopy was adopted to further elucidate the electronic structures of boron carbides. A peak centered at *ca.* 448 nm (2.78 eV) was observed with an excitation wavelength of 325 nm in Figure 4.6(bottom). This agrees well with a previous theoretical study, and indicates that an indirect energy gap of 2.78 eV exists in  $B_{12}C_3$ .<sup>24</sup>

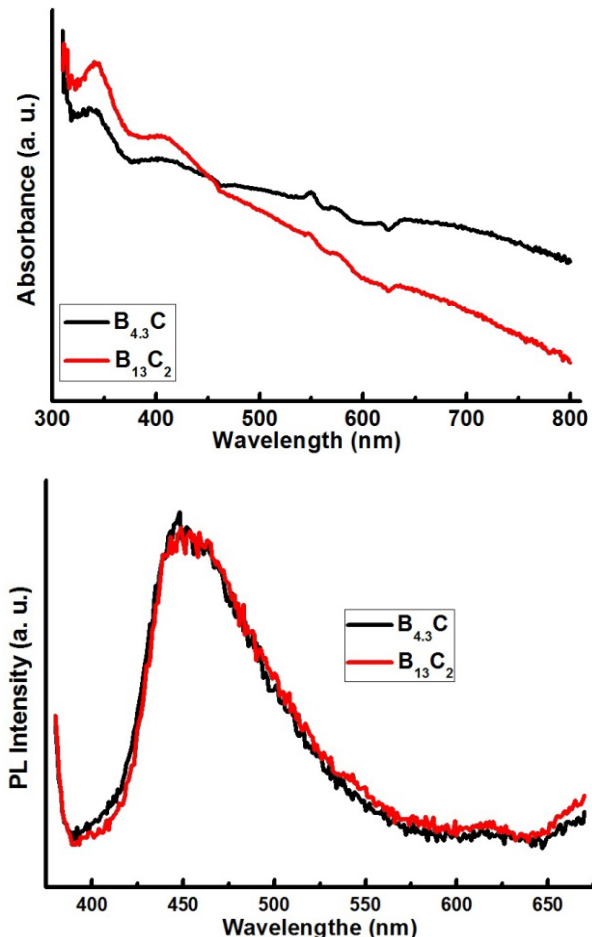


**Figure 4.6** Top: UV-visible diffuse reflectance spectra. Bottom: Photoluminescence spectra at room temperature with the excitation wavelength of 325 nm.

SEM images (Figure 4.7) show that both boron carbides consist of big particles and the size varies from several micrometers to *ca.* 10 µm. The specific surface areas of both boron carbides are negligible by the Brunauer-Emmett-Teller (BET) method.

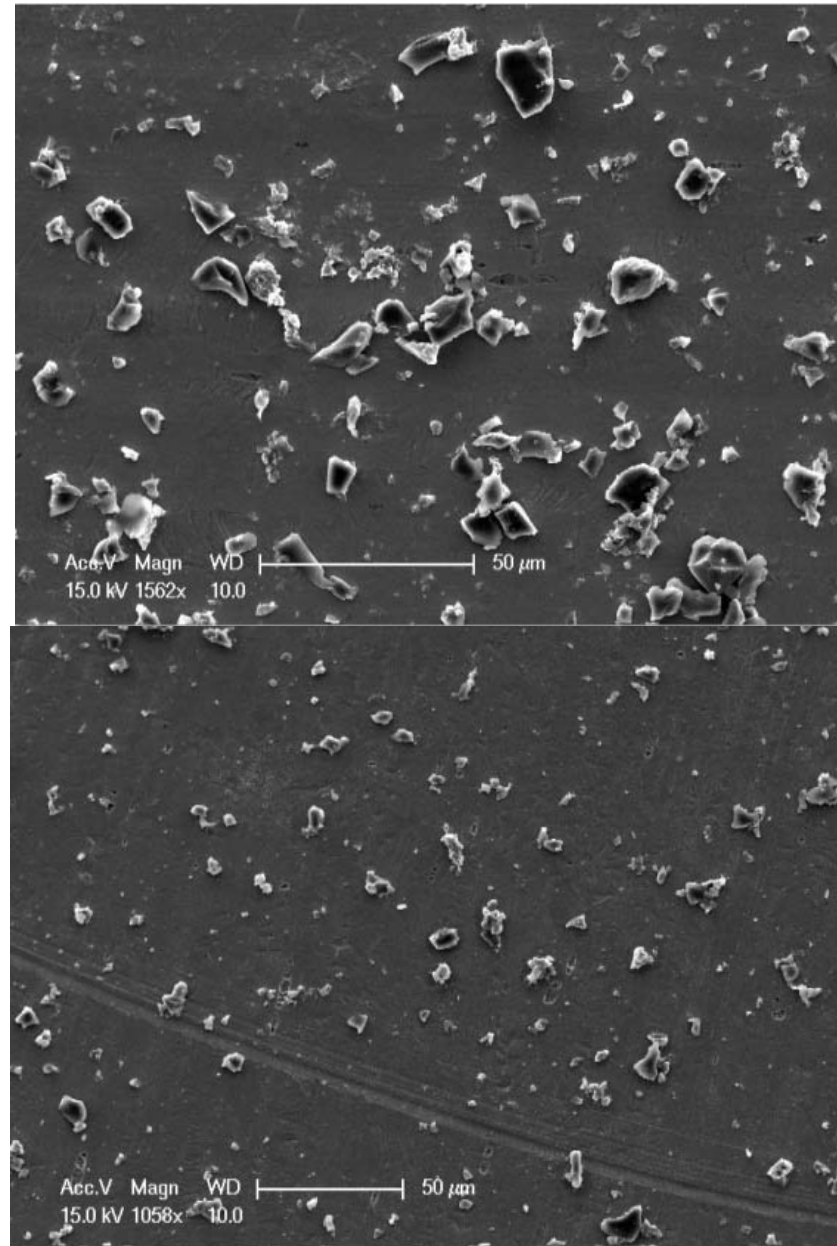


**Figure 4.7** SEM images of B<sub>4.3</sub>C (top) and B<sub>13</sub>C<sub>2</sub> (bottom).

EDX spectra (Figure 4.8) confirm that the photocatalysts only contain boron and carbon elements (the Cu and Pt elements are from the substrates and coating for EDX measurements). TGA analysis (Figure 4.9) shows that the boron carbides start being oxidized at *ca.* 450 °C in air.

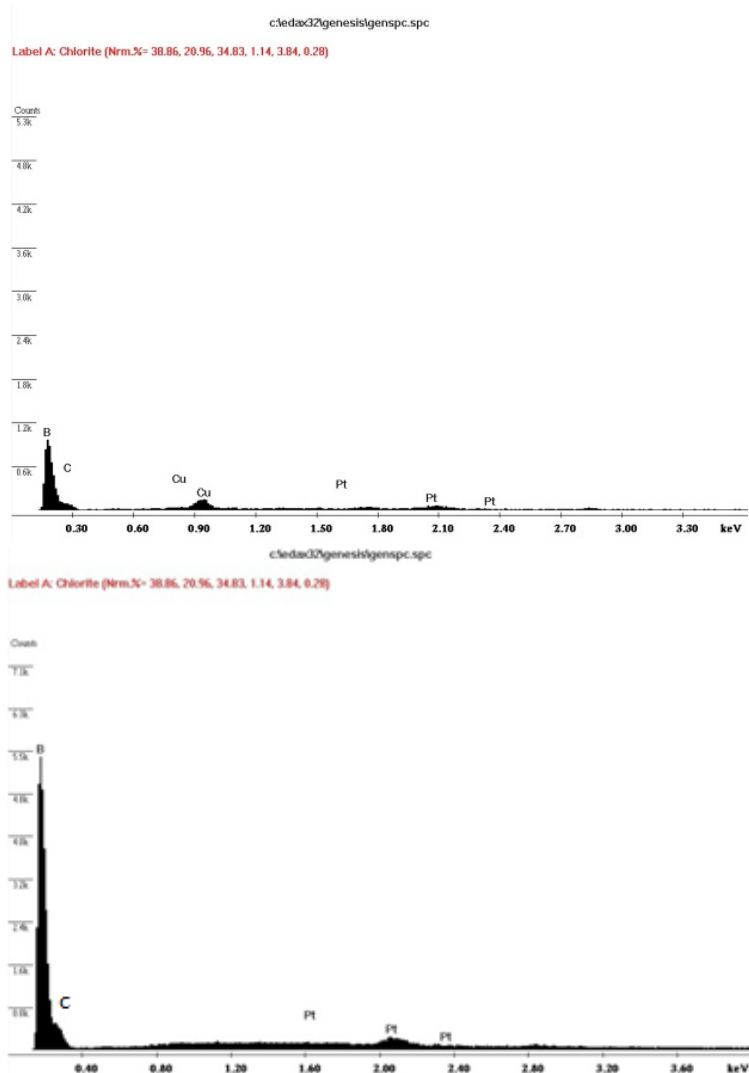


**Figure 4.8** EDX spectra of  $\text{B}_{4.3}\text{C}$  (top) and  $\text{B}_{13}\text{C}_2$  (bottom).

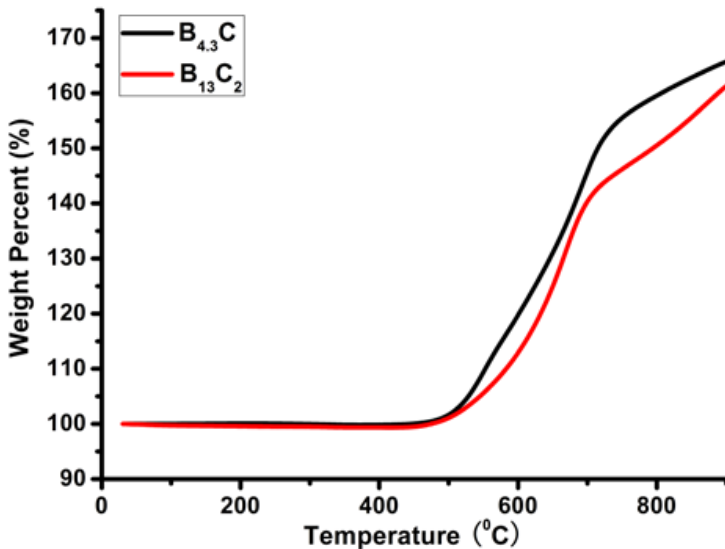
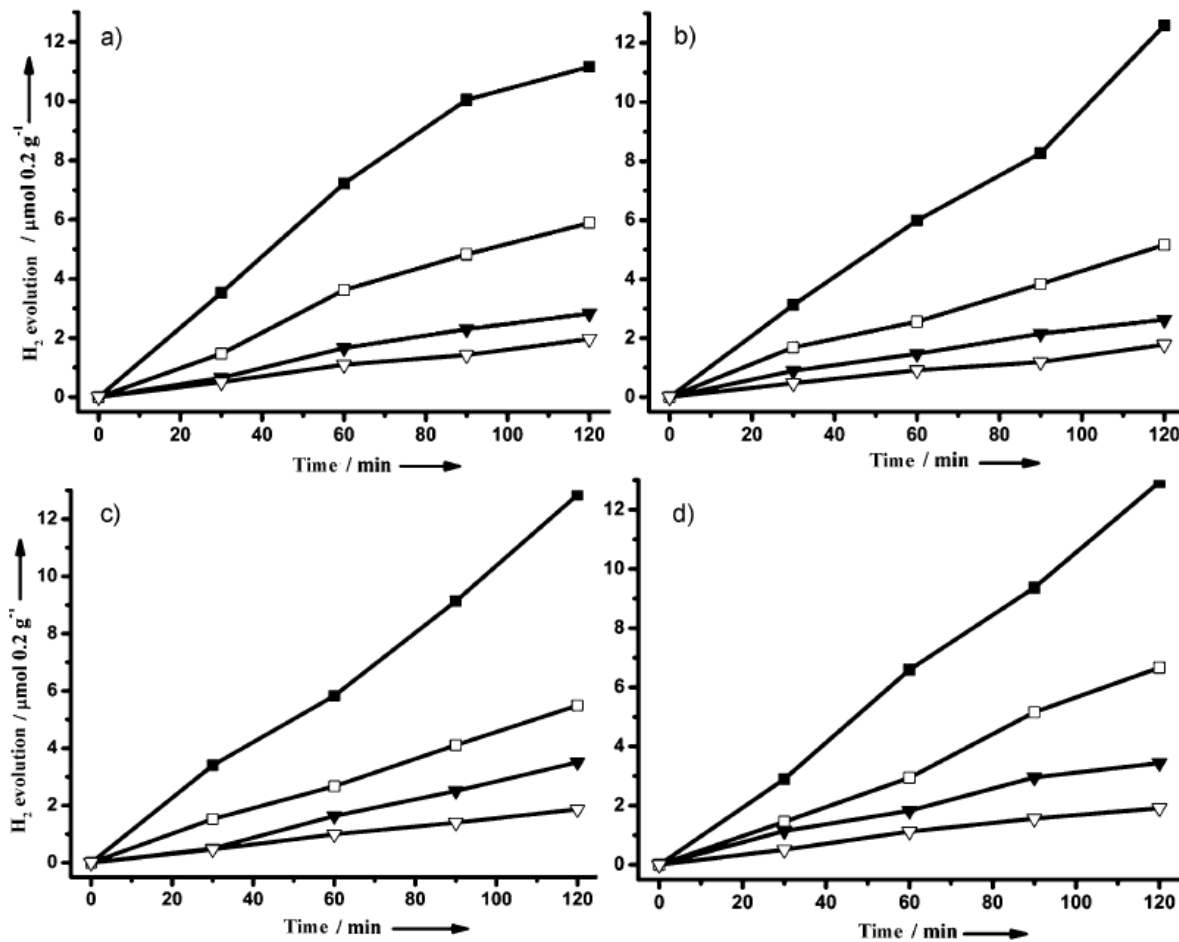


**Figure 4.9** The TGA curves of  $B_{4.3}C$  and  $B_{13}C_2$  in air.

#### 4.4.2 Study of Photocatalytic and PEC H<sub>2</sub> Evolution

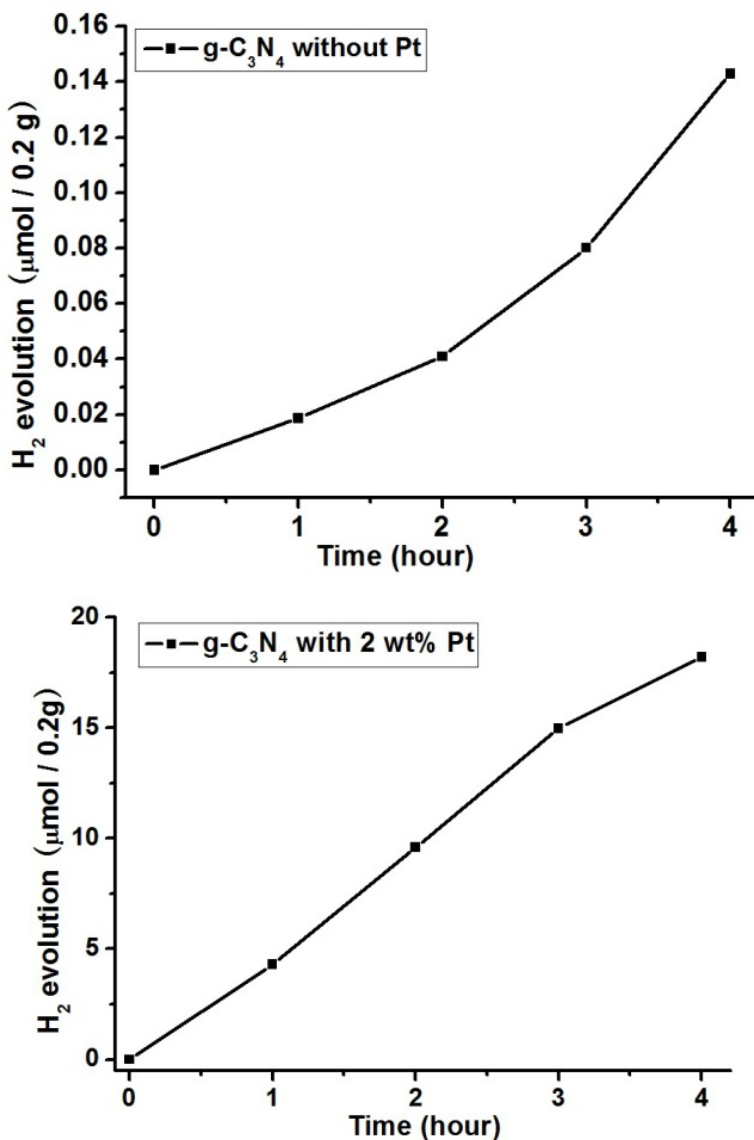
The photocatalytic properties of boron carbides for H<sub>2</sub> evolution from water were studied using a 25% methanol aqueous solution as the sacrificial agent under visible light irradiation (>420 nm).

Figure 4.10 shows the time courses of H<sub>2</sub> evolution from the two boron carbides. Without any co-catalysts, the H<sub>2</sub> evolution rates (average rate from four cycles) of  $B_{4.3}C$  and  $B_{13}C_2$  are *ca.* 2.9  $\mu\text{mol h}^{-1}/0.2 \text{ g}$  and *ca.* 0.9  $\mu\text{mol h}^{-1}/0.2 \text{ g}$ , respectively. After loading 2 wt% Pt, the H<sub>2</sub> evolution rates of  $B_{4.3}C$  and  $B_{13}C_2$  were increased to *ca.* 6.2  $\mu\text{mol h}^{-1}/0.2 \text{ g}$  and *ca.* 1.6  $\mu\text{mol h}^{-1}/0.2 \text{ g}$ , respectively. The H<sub>2</sub> evolution rates remain stable even after 100 h (see the fourth cycle), which is indicative of long-term photocatalyst stability.



**Figure 4.10** Time course of H<sub>2</sub> evolution under visible light irradiation. a) 1st cycle, b) 2nd cycle after reevacuation, c) 3rd cycle after re-evacuation, d) 4th cycle after re-evacuation and 100 h reaction time. B<sub>4.3</sub>C with Pt (—■—), B<sub>4.3</sub>C without Pt (—□—), B<sub>13</sub>C<sub>2</sub> with Pt (—▼—), B<sub>13</sub>C<sub>2</sub> without Pt (—▽—).

For comparison, we studied metal-free g-C<sub>3</sub>N<sub>4</sub> photocatalysts, which were synthesized according to a previous report.<sup>2</sup> The g-C<sub>3</sub>N<sub>4</sub> catalyst exhibits *ca.* 0.035 μmol h<sup>-1</sup>/0.2 g of H<sub>2</sub> evolution without Pt loading, and *ca.* 4.7 μmol h<sup>-1</sup>/0.2 g after loading 2 wt% Pt (Figure 4.11).



**Figure 4.11** Synthesized  $\text{g-C}_3\text{N}_4$  for H<sub>2</sub> evolution reaction under the same experimental conditions as what were used for boron carbides. (Since the activity of  $\text{g-C}_3\text{N}_4$  without Pt is too low, sampling interval was extended to 1 hour instead of 30 min in order to reduce experimental errors.)

Therefore,  $\text{B}_{4.3}\text{C}$  exhibits a rate of H<sub>2</sub> evolution *ca.* 83 times higher than that of  $\text{g-C}_3\text{N}_4$  without Pt loading and 1.3 times higher than with 2 wt% Pt loading. The apparent quantum yield (AQY) of  $\text{B}_{4.3}\text{C}$  and  $\text{g-C}_3\text{N}_4$  was determined with a 420 nm band-pass

filter. The observed AQY of Pt/B<sub>4.3</sub>C is *ca.* 0.54% compared to *ca.* 0.23% of Pt/g-C<sub>3</sub>N<sub>4</sub> at 420 nm (AQY of bare B<sub>4.3</sub>C is *ca.* 0.34%). The water splitting reactions proceeded catalytically, as indicated by calculated turnover numbers of greater than 2 (generated H<sub>2</sub> to amount of photocatalysts used; see Photocatalytic Experiments in the Experimental Section). To facilitate the measurements, H<sub>2</sub> was collected by illuminating the reaction using a 300W Xe lamp without any filter.<sup>2</sup> After the turnover experiments, the photocatalysts were centrifuged and recharacterized by XRD and FT-Raman spectroscopy to confirm the photostability of boron carbides. Aside from a slight decrease in the XRD peak intensities for B<sub>4.3</sub>C, there are no obvious changes in the peak positions of XRD or FT-Raman spectra, as shown in Figure 4.12 and Figure 4.13. This indicates that the crystalline structure of B<sub>4.3</sub>C is preserved after the turnover experiments and that B<sub>4.3</sub>C is stable during the reaction process. After the photocatalytic reactions, the B<sub>13</sub>C<sub>2</sub> XRD peak at *ca.* 31.88 disappeared and the Raman spectra shifted to slightly higher wavenumbers, which indicates that there were some structural changes of B<sub>13</sub>C<sub>2</sub>. However, the main crystal structure of B<sub>13</sub>C<sub>2</sub> is still maintained after the photocatalytic reactions. The overall peak intensity decrease may be due to the peak broadening associated with the reduced sample particle size resulting from the constant stirring during photocatalysis.

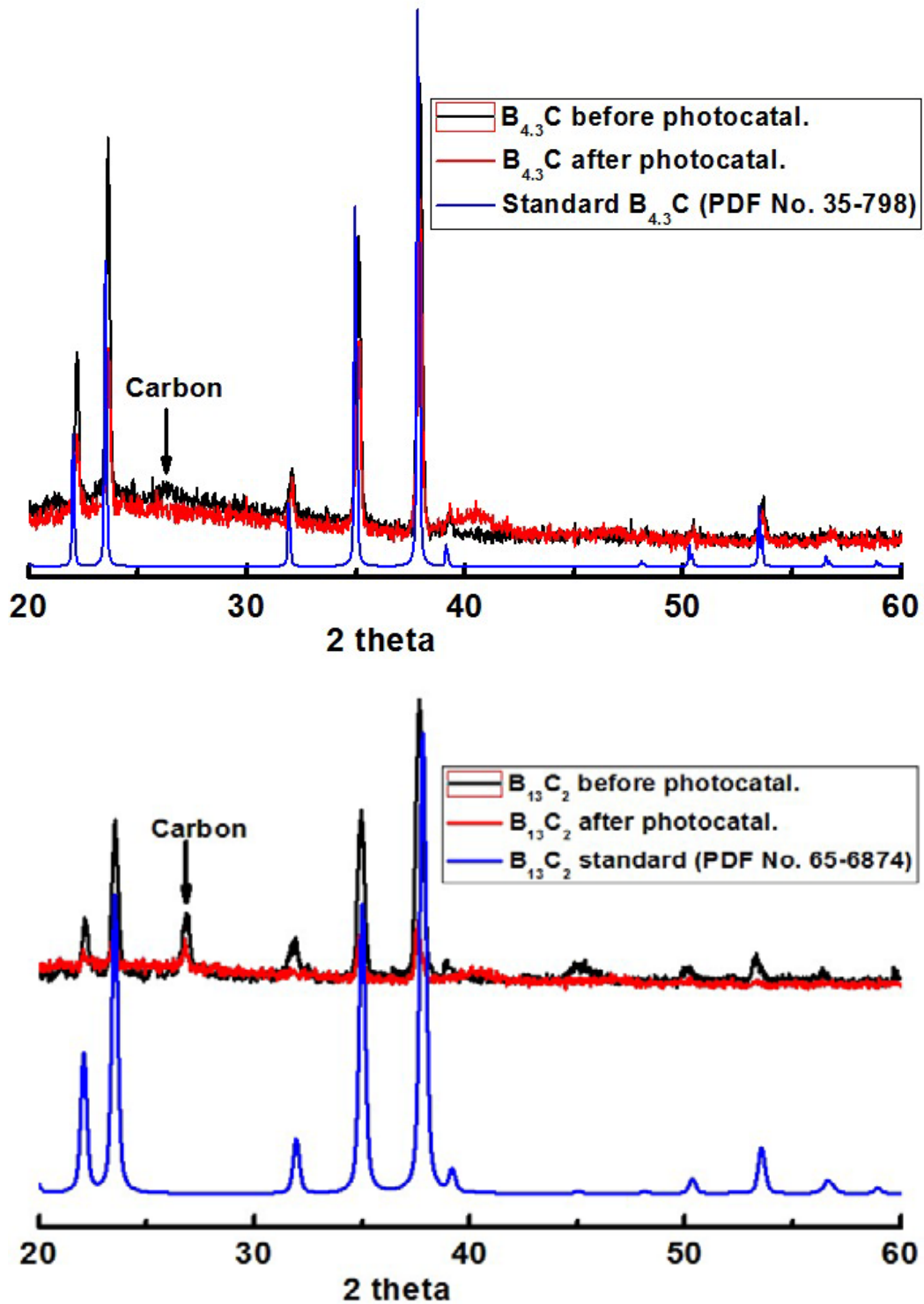


**Figure 4.12** XRD patterns of  $\text{B}_{4.3}\text{C}$  before and after photocatalysis reaction (top) and  $\text{B}_{13}\text{C}_2$  before and after photocatalysis reaction (bottom).

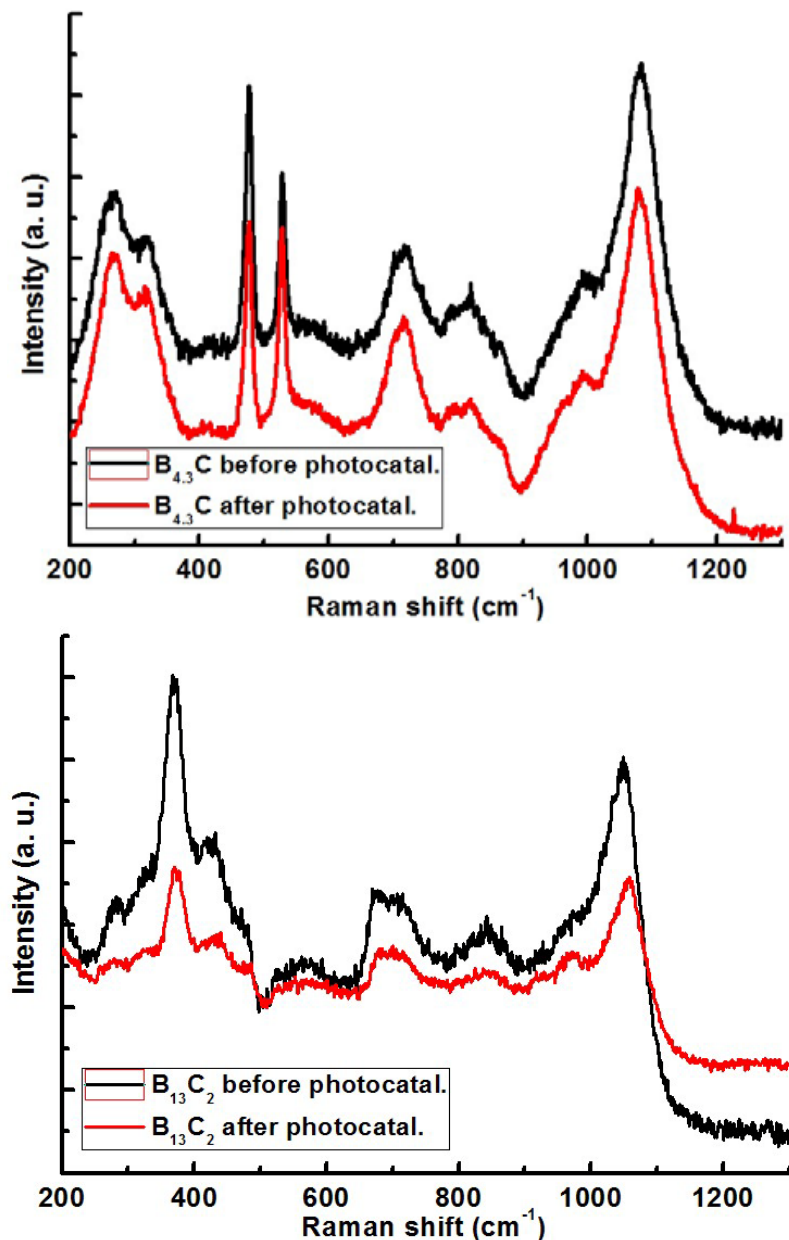


**Figure 4.13** FT-Raman spectra of  $B_{4.3}C$  before and after photocatalysis reaction (top) and  $B_{13}C_2$  before and after photocatalysis reaction (bottom).

The PEC experiments were conducted with boron carbide films on fluorine-doped tin-oxide glass slides (FTO) prepared by electrophoretic deposition (EPD) under optimized experimental conditions. This procedure is commonly employed in the

processing of ceramics, coatings, and composite materials.<sup>25</sup> For each photocathode, a significant cathodic photocurrent was observed that increased with increasing negative potential bias, thus indicating their p-type characteristics in the depletion condition.

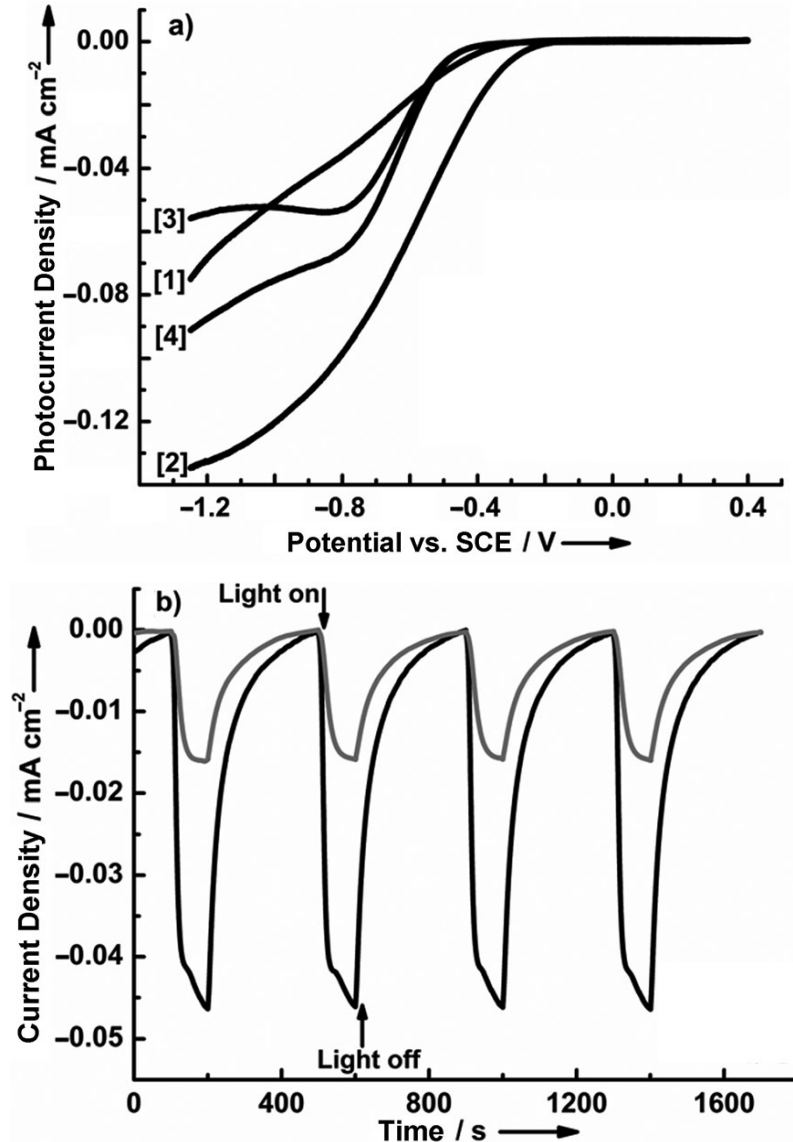


**Figure 4.14** a) Current-potential curves in  $\text{Na}_2\text{SO}_4$  aqueous solution (0.01m) under visible light. [1]  $\text{B}_{4.3}\text{C}$  dark, [2]  $\text{B}_{4.3}\text{C}$  visible light, [3]  $\text{B}_{13}\text{C}_2$  dark, [4]  $\text{B}_{13}\text{C}_2$  visible light. b) Transient photocurrent curves under visible light at -0.8 V vs. SCE.  $\text{B}_{13}\text{C}_2$  (gray),  $\text{B}_{4.3}\text{C}$  (black).

Figure 4.14 (top) shows the current-densitypotential (J-E) behavior of the boron carbide films in aqueous Na<sub>2</sub>SO<sub>4</sub> solution (0.01M) both in the dark and under visible light irradiation (>420 nm). The electrode achieves a cathodic current density of *ca.* 46 μAcm<sup>-2</sup> for B<sub>4.3</sub>C and *ca.* 16 μAcm<sup>-2</sup> for B<sub>13</sub>C<sub>2</sub> at -0.8 V applied bias vs. SCE (after subtracting dark current) as shown in Figure 4.14 (bottom).

#### 4.4.3 Study of DOS Calculations

DFT calculations were performed to understand the different observed photocatalytic behaviors of the two boron carbides. Because boron carbides exhibit an extremely high concentration of defects,<sup>26</sup> no single unit cell can adequately represent the whole structure. Fortunately, the concentrations of structural defects (B<sub>12</sub> and B<sub>11</sub>C icosahedra; C-B-C, C-B-B, B-vacancy-B chains) in boron carbides have been studied in detail.<sup>18</sup> To model these materials with periodic DFT calculations, we constructed 5 x 1 x 1 supercell models for B<sub>4.3</sub>C and B<sub>13</sub>C<sub>2</sub>, into which we can introduce defects in roughly the same proportions as in the experimental materials.

We then computed the density of states (DOS) of B<sub>4.3</sub>C and B<sub>13</sub>C<sub>2</sub> for 1) idealized, geometry-optimized boron carbides without defects, (such as (B<sub>11</sub>C)CBC), 2) boron carbides with defects inserted with no geometric relaxation, and 3) fully relaxed defect-containing boron carbides (Figure 4.15). First, our computed DOS on the idealized models agrees well with previous reports.<sup>26</sup> Second, the high concentration of structural

defects distorts the  $B_{12}$  or  $B_{11}C$  icosahedra in  $B_{4.3}C$  and  $B_{13}C_2$  upon DFT supercell optimization (Figure 4.1 and Figure 4.2).

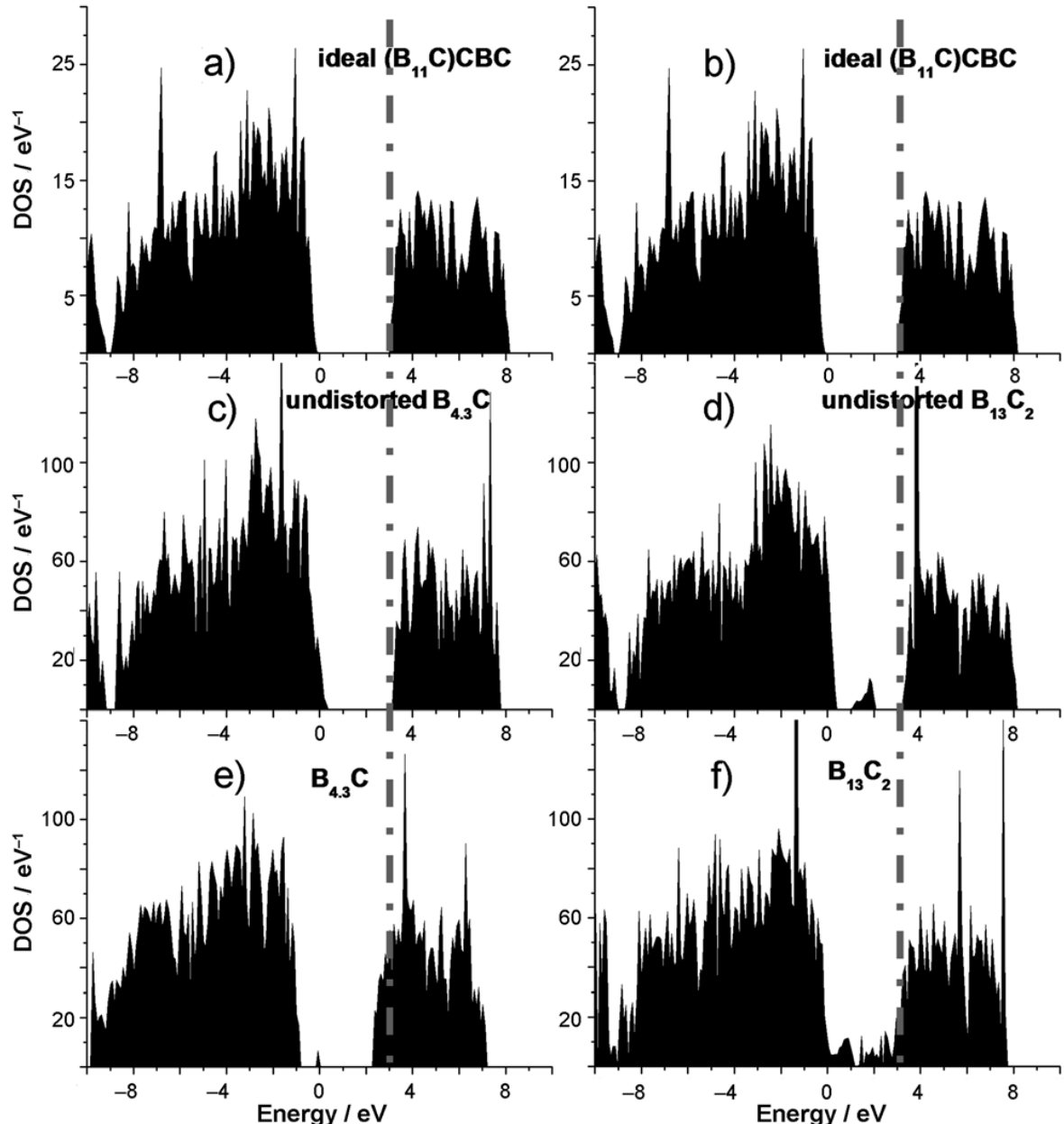


**Figure 4.15** a) and b) Total DOS of the optimized ideal structure of  $(B_{11}C)CBC$ . c) and d) The DOS of  $B_{4.3}C$  and  $B_{13}C_2$  with defects, but no structural relaxation. e) and f) The DOS of  $B_{4.3}C$  and  $B_{13}C_2$  with defects after structural relaxation. The dotted gray line highlights the downshift of the conduction band edge for  $B_{4.3}C$ .

As shown in Figure 4.15, significant changes in the DOS occur when the defects are introduced, and larger changes appear once the defect-containing structures are relaxed. In  $B_{4.3}C$ , the fully relaxed, defect-containing structure exhibits a significant continuum downshift of the CB and new midgap states at the Fermi level (see Figure 4.15e). As shown in Figures 4.15 and Figure 4.16, the CB edge downshift arises from distortions of the  $B_{11}C$  and  $B_{12}$  icosahedra upon structural relaxation, whereas the midgap state arises from the C-B-B chain defect. As a result, compared to the idealized structure, the intrinsic defects in  $B_{4.3}C$  narrow the band gap from *ca.* 3.0 eV to *ca.* 2.1 eV and facilitate its visible light absorption. Similarly, previous studies which demonstrated that introducing significant surface disorder by hydrogenating  $TiO_2$ <sup>27</sup> or growing a new phase on the surface of rutile  $TiO_2$  (011)<sup>28</sup> can result in significant continuum upshift of its VB edge, which improves the photocatalytic properties more effectively than traditional doping methods to create isolated midgap states. It appears, therefore, that the intrinsic defects in  $B_{4.3}C$  play an important role in its effective photocatalysis under visible light irradiation.

The situation for  $B_{13}C_2$  is slightly more complicated. Undistorted  $B_{13}C_2$  exhibits many midgap states between the VB and CB because of its more complicated structural defects. In this case, the distortions in  $B_{13}C_2$  introduce even more midgap states instead of downshifting the CB edge (Figure 4.15f). It is well known that the midgap states can

function as electron/hole traps and facilitate charge recombination,<sup>29</sup> and this may be one reason why  $B_{13}C_2$  exhibits lower photocatalytic efficiency than  $B_{4.3}C$ .

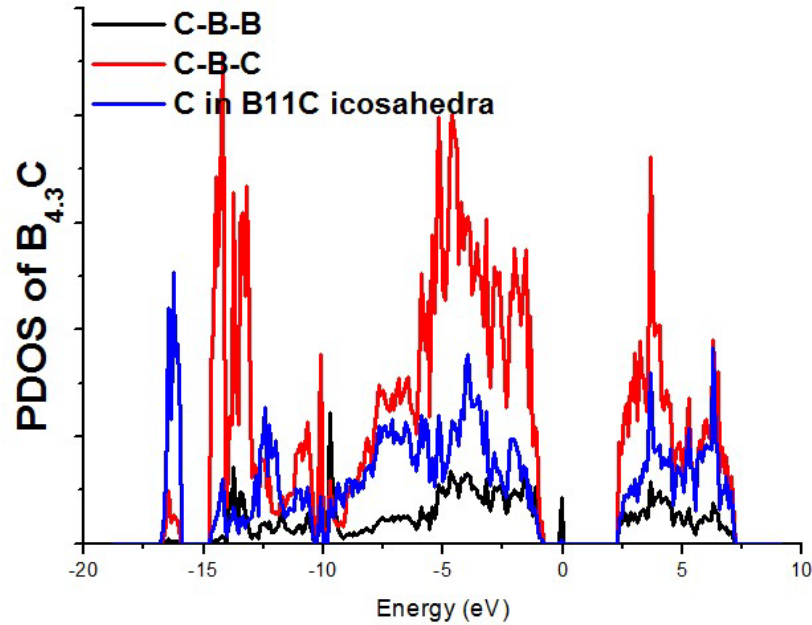


**Figure 4.16** The site projected density of states (PDOS) of  $B_{4.3}C$ .

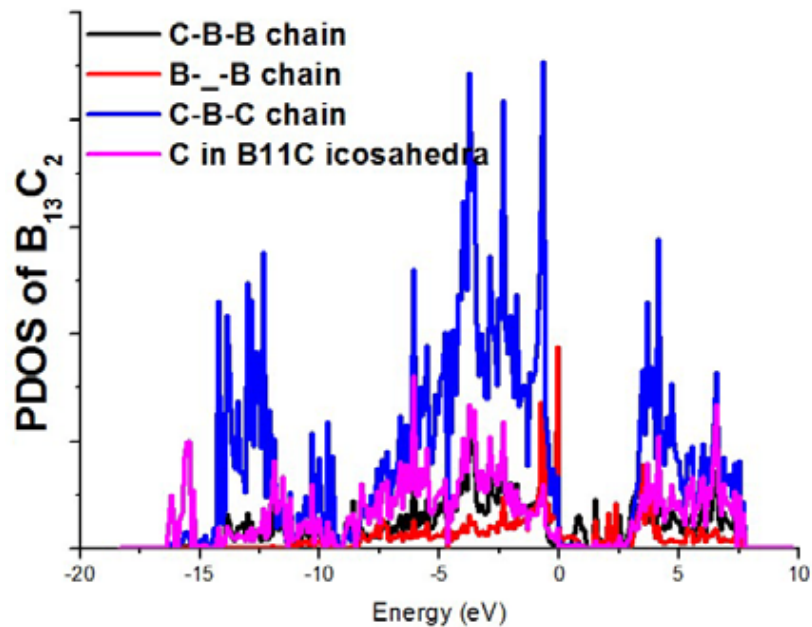


**Figure 4.17** The site PDOS of  $B_{13}C_2$ .

#### **4.5 Conclusion**

In conclusion, two boron carbides have been demonstrated to perform photocatalytic H<sub>2</sub> evolution and PEC water reduction under visible light. Importantly, these metal-free photocatalysts exhibit high efficiency even without any precious metal co-catalyst loading. We further show that B<sub>4.3</sub>C exhibits better efficiency and stability than B<sub>13</sub>C<sub>2</sub>. DFT calculations suggest that the defects and structural distortions in B<sub>4.3</sub>C cause a downshift of its CB edge that narrows its band gap and facilitates its visible light absorption. However, in B<sub>13</sub>C<sub>2</sub>, the more complicated structural defects and distortions introduce midgap states between the CB and VB that facilitate charge recombination and reduce its photocatalytic efficiency. We expect that these boron carbides will provide new opportunities for the future development of efficient and stable visible-light-responsive photocatalysts and solar cell materials.

## 4.6 References

- (1) (a) Chen, X.; Shen, S.; Guo, L.; Mao, S. S. *Chem. Rev.* **2010**, *110*, 6503; (b) Kudo, A.; Miseki, Y. *Chem. Soc. Rev.* **2009**, *38*, 253; (c) Walter, M. G.; Warren, E. L.; McKone, J. R.; Boetcher, S. W.; Mi, Q.; Santori, E. A.; Lewis, N. S. *Chem. Rev.* **2010**, *110*, 6446.
- (2) Wang, X.; Maeda, K.; Thomas, A.; Takanabe, K.; Xin, G.; Carlsson, J. M.; Domen, K.; Antonietti, M. *Nature Mater.* **2009**, *8*, 76.
- (3) Wang, Y.; Wang, X.; Antonietti, M. *Angew. Chem.* **2012**, *124*, 70; *Angew. Chem. Int. Ed.* **2012**, *51*, 68.
- (4) Yanagida, S.; Kabumoto, A.; Rheingold, A. L.; Heinekey, D. M. *J. Chem. Soc. Chem. Commun.* **1985**, 474.
- (5) Zhang, Z.; Long, J.; Yang, L.; Chen, W.; Dai, W. Fu, X.; Wang, X. *Chem. Sci.* **2011**, *2*, 1826.
- (6) Liu, G.; Niu, P.; Yin, L.; Cheng, H. *J. Am. Chem. Soc.* **2012**, *134*, 9070.
- (7) Wang, F.; Ng, W. K. H.; Yu, J. C.; Zhu, H.; Li, C.; Zhang, L.; Liu, Z.; Li, Q. *Appl. Catal. B* **2012**, *111-112*, 409.
- (8) Hou, Y.; Abrams, B. L.; Vesborg, P. C. K.; Bjorketun, M. E.; Herbst, K.; Bech, L.; Setti, A. M.; Damsgaard, C. D.; Pedersen, T.; Hansen, O.; Rossmeisl, J.; Dahl, S.; Norskov, J. K.; Chorkendorff, L. *Nature Mater.* **2011**, *10*, 434.
- (9) (a) Wood, C.; Emin, D. *Phys. Rev. B* **1984**, *29*, 4582; (b) Lazzari, R.; Vast, N.; Besson, J. M.; Baroni, S.; Dal Corso, A. *Phys. Rev. Lett.* **1999**, *83*, 3230.
- (10) Joshi, U. A.; Palasyuk, A.; Arney, D.; Maggard, P. A. *J. Phys. Chem. Lett.* **2010**, *1*, 2719.
- (11) (a) Fanchini, G.; McCauley, J. W.; Chhowall, M. *Phys. Rev. Lett.* **2006**, *97*, 035502; (b) Aydin, S.; Simsek, M. *Phys. Status Solidi B* **2009**, *246*, 62.
- (12) Saal, J. E.; Shang, S.; Liu, Z. *Appl. Phys. Lett.* **2007**, *91*, 231915.

- (13) Perdew, J. P.; Burke, K.; Ernzerhof, M. *Phys. Rev. Lett.* **1996**, *77*, 3865.
- (14) Kresse, G.; Joubert, D. *Phys. Rev. B* **1999**, *59*, 1758.
- (15) Kresse, G.; Furthmuller, J. *Phys. Rev. B* **1996**, *54*, 11169.
- (16) (a) Kuhlmann, U.; Werheit, H.; Schwetz, K. A. *J. Alloys Compd.* **1992**, *189*, 249; (b) Emin, D. *Phys. Rev. B* **1988**, *38*, 6041.
- (17) Werheit, H. *J. Phys. Condens. Matter* **2006**, *18*, 10655.
- (18) (a) Werheit, H.; Au, T.; Schmeichel, R.; Shalamberidze, S. O.; Kalandadze, G. I.; Eristavi, A. M. *J. Solid State Chem.* **2000**, *154*, 79; (b) Werheit, H.; Rotter, H. W.; Meyer, F. D.; Hillebrecht, H.; Shalmberidze, S. O.; Abzianidze, T. G.; Esadze, E. G. *J. Solid State Chem.* **2004**, *177*, 569.
- (19) Gosset, D.; Colin, M. *J. Nucl. Mater.* **1991**, *183*, 161.
- (20) Thevenot, F. *J. Eur. Ceram. Soc.* **1990**, *6*, 205.
- (21) Tallant, D. R.; Aselage, T. L.; Campbell, A. N.; Emin, D. *Phys. Rev. B* **1989**, *40*, 5649.
- (22) (a) Amberger, E.; Stumpf, W.; Buschbeck, K. C. *Gmelin Handbook of Inorganic Chemistry*, Springer-Verlag, Berlin 1981; (b) Beauvy, M. *J. Less-Common Met.* **1983**, *90*, 169.
- (23) Saal, J. E.; Shang, S.; Liu, Z. *Appl. Phys. Lett.* **2007**, *91*, 231915.
- (24) Bylander, D. M.; Kleinman, L.; Lee, S. *Phys. Rev. B* **1990**, *42*, 1394.
- (25) (a) Sarkar, P.; Nicholson, P. S. *J. Am. Ceram. Soc.* **1996**, *79*, 1987; (b) Boccaccini, A. R.; Zhitomirsky, I. *Curr. Opin. Solid State Mater. Sci.* **2002**, *6*, 251.
- (26) Domnich, V.; Reynaud, S.; Haber, R. A.; Chhowalla, M. *J. Am. Ceram. Soc.* **2011**, *94*, 3605.
- (27) Chen, X.; Liu, L.; Yu, P. Y.; Mao, S. S. *Science* **2011**, *331*, 746.

- (28) Tao, J.; Luttrell, T.; Batzill, M. *Nature Chem.* **2011**, *3*, 296.
- (29) Clark, J. H.; Dyer, M. S.; Palgrave, R. G.; Ireland, C. P.; Darwent, J. R.; Claridge, J. B.; Rosseinsky, M. J. *J. Am. Chem. Soc.* **2011**, *133*, 1016.